CRANFIELD UNIVERSITY

Kevin Lontin

Wear and airborne noise interdependency at asperitical level: analytical modelling and experimental validation

School of Aerospace, Transport and Manufacturing
PhD in Manufacturing

PhD
Academic Year: 2018 - 2021

Supervisor: Dr. Muhammad Khan
Associate Supervisor: Prof. Andrew Starr
September 2021

CRANFIELD UNIVERSITY

School of Aerospace, Transport and Manufacturing
PhD in Manufacturing

PhD

Academic Year 2018 - 2021

Kevin Lontin

Wear and airborne noise interdependency at asperitical level: analytical modelling and experimental validation

Supervisor: Dr. Muhammad Khan
Associate Supervisor: Prof. Andrew Starr
September 2021

This thesis is submitted in fulfilment of the requirements for the degree of Doctor of Philosophy

ABSTRACT

Generation of wear and airborne sound is inevitable during friction processes. Most correlation between the wear and the sound generated during a sliding process have been experimental. Analytical models do exist, but they remain scarce and do not fully account for the wear and the airborne sound generation especially at asperitical level. The model developed in this research attempts to fill the gap by providing a quantifiable relationship between the wear generated and the sound emitted in a simple pin-on-disc setup. It provides a relationship between the wear and the sound from an asperitical level. This is done by examining the conditions at which wear would occur on an asperity distribution. The asperity distribution is considered to be exponential, although a Gaussian distribution was also considered. Impact forces are calculated on a per-asperity basis and the wear and vibrational displacement is calculated as a result. This leads to the quantification of wear and acoustic noise. The model is validated using a pin-on disc setup for three varied materials (iron (4% carbon content), mild steel (0.18% carbon content) and aluminium T351) under two loads (10 N and 20 N) at 300 RPM. The loads and speeds were chosen so as to observe a range of wear behaviour while remaining within the constraints of the lab limitations and the safety of the force sensors on the tribometer. Temperatures are also examined, and a second set of validation experiment is performed at temperatures of 40 °C and 60 °C. The model computes the predicted wear and sound pressure, and it is compared with the experimental sound pressure measured by the microphone and the wear measured by the tribometer sensors. Sound pressure is chosen as a measure over frequency because it is easier to analyse and compare. The theoretical model agrees with the experimental results with a varying error of 10 to 15 % error in iron and aluminium. However, a larger error is observed in the case of mild steel. The model could be refined to improve the accuracy as it assumes point impacts on the asperities where a distributed impact would be more suitable. Furthermore, the pin is assumed a single asperity to simplify the model at the expense of accuracy. Overall, the experimental results are in fair correlation with the

theoretical results and this model provides the first step in quantifying wear using only the recorded sound pressure.

Keywords:

Friction, wear, acoustic noise, analytical modelling, pin-on-disc setup, single point contact

ACKNOWLEDGEMENTS

I would like to thank both of my supervisors, Dr. Muhammad Khan, and Prof. Andrew Starr. I would also like to thank Mr Alan Haume for his help on the interferometry tests, Mr Graham Hartwell for providing us with the samples, Mr Steve Pope for grinding the samples and Dr. Diane Johnson for providing the SEM images. I would further like to thank Mr Hamza Shams for his support and Mr Bander Alharbi for performing the high temperature validation experiments. Finally, I would like to thank my parents for their support throughout my studies.

TABLE OF CONTENTS

LIST OF FIGURES

LIST OF TABLES

LIST OF EQUATIONS

LIST OF PUBLICATIONS

1. Lontin, K., Khan, M. Interdependence of friction, wear, and noise: A review. *Friction* **9,** 1319–1345 (2021).
2. 164 Interdependence of friction, wear and noise: A review (BSSM 14th conference, Belfast)
3. Wear and Airborne noise interdependency at asperitical level: Analytical modelling and Experimental validation (FRICTION-2021-0190.R1, awaiting reviewer scores after submitting revision)
4. Multiple Point Contact Wear Prediction and Source Identification Scheme Using a Single Channel Blended Airborne Acoustic Signature (4th IFAC Workshop on Advanced Maintenance Engineering, Services and Technologies)

1 Identification and Significance of the Problem

1.1 Research Problem

Wear processes present a significant challenge in industry. This is because as wear occurs, this leads to the reduction of machine life and expensive component replacements [1]. In the worse cases, wear can lead to catastrophic machine failure if not noticed soon enough which can lead to the loss of life. It is important to track the progress of wear in order to minimise the risk of machine failure. The friction of the worn-out surfaces will influence the rate at which wear occurs as well as the type of wear that will occur along with the methods of identification.

There are different methods that can be used to identify the types of wear that occur. Those will differ based on the classification of the wear. Some of the wear mechanisms occur due to adhesive wear (when the wear debris attach from one surface to another), abrasive wear (when a hard surface slides across a softer surface), fatigue wear (caused by cyclic loading), fretting wear (caused by surfaces rubbing), erosive wear (caused by particle impacts) and corrosion and oxidational wear (caused by chemical reactions) [2]. There are different methods that can be used to monitor wear in machine components. These can be classified in two main categories: Direct monitoring and indirect monitoring [3]. Direct monitoring involves direct measurements of the wear by using optical, radioactive sensors, electrical resistance sensors or vision systems. They offer accurate readings, but a significant drawback of such methods is that the machine component of interest is not always easily accessible and would often require shutdown of the whole machine. Indirect monitoring systems involve measuring parameters that can be correlated with the wear state such as by measuring the vibrations or the emitted airborne noise. This is because the changes in the wear state would lead to a change in the airborne noise emission and acoustic emissions [4].

One of the most common types of wear in industrial machinery is sliding wear. This is caused by two surfaces sliding in relative motion across each other. The

harder surface wearing out the softer surface via abrasive wear. Direct measurements of such wear would require the removal of one of the two surfaces for visual inspection thus requiring significant downtime. Indirect measurements would therefore be more suitable. As the asperities on one of the surfaces interact with the asperities on the bottom surface, the surface topography would change, and this would lead to a change in the airborne noise emission. Indirect measurements of the wear would involve measuring the noise emitted by the machine and linking it to the change in the surface topography due to the progression of wear.

Understanding how the wear and the friction processes are linked with the sound generation is essential for various reasons. Not only does it lead to an ability to determine the wear of machine components via indirect means, but it is also important because it leads to efforts to reduce the noise. For example, noise reduction is very important in the automotive industry as it leads to higher customer satisfaction [5]. This is especially true for brake squeal noise which is an area of undergoing research.

There have been a lot of experimental observations of the change of the sound spectrum emitted by materials undergoing friction and wear. This was also linked to the surface roughness. As the surface roughness increases, so does the sound pressure. Along with experimental observations, several numerical models were developed to examine the interdependencies between the sound pressure and the friction processes. The impacts between the antagonist asperities on the two surfaces cause the kinetic energy to be converted to vibrational energy which is then responsible for the radiation of sound. However, most of the numerical models do not take the wear into account, so the asperitical distribution due to the wear is not factored in. Theoretical models asperitical based friction models do exist but they do not take the wear into account either.

1.2 Research Background

There are many models that deal with friction, wear, and noise. However, most of those models are empirical or experimental and do not involve the physical

interactions at a microscopic level. More advanced models that deal with the relationship between the wear, the friction and the noise are scarce. Those models are not often used and most of them do not include the wear either. Unifying the wear and the noise from an analytical perspective into one general model would be a significant advancement. It could potentially also be simple enough to be used in industrial applications.

1.3 Research Aim and Objectives

The aim of this research project was to create an analytical model that would be able to quantify the amount of wear that occurs during a sliding friction process by analysing the sound pressure emitted during friction. It was accomplished by completing the following individual objectives:

1. Identify the current research gap by performing a thorough literature review on the current work pertaining to the research topic.
2. Create an analytical model that encompasses the wear and the noise emitted during a sliding friction process at asperitical level.
3. Devise an experimental scheme and acquire the required samples. The samples need to be prepared according to the chosen experimental scheme by grinding them to an appropriate surface roughness and manufacturing them to the required thickness.
4. Validate the theoretical approach using the chosen experimental scheme

1.4 Structure of the Thesis

The thesis is structured as follows:

In chapter 2, a thorough literature review is presented. It provides an overview of the most significant research in friction and wear along with the acoustics of friction. It also presents the state-of-the-art in this domain along with the research gap. Considering the identified research gap, chapter 3 proposes the methodology that was employed to address the research gap. Chapter 4 details the mathematical model along with the theory and assumptions that were made

as the model was developed. It is split into three parts. The first part includes the topographical changes of the asperities on the surface due to wear. The second part details how the sound is generated due to the elastic vibrations of the asperities while the third part deals with the sound generated due to the asperities breaking. All three parts are then combined to form the final solution. Chapter 4 also includes a small sample of the computer code that highlights the important parts of the code. The computer program is also where the initial distribution function is chosen. Finally, chapter 4 concludes with the analytical results that were given by the MATLAB program. Chapter 5 details the experimental scheme that was devised to validate the model. This includes the experimental setup as well as the different materials tested and the different operating conditions. There are two stages to the experimental scheme. The first stage includes performing the validation experiments at room-temperature, whereas the second stage involves performing the validation experiments at higher than room temperatures. Chapter 6 describes the experimental results and compares them to the analytical results. It also provides a detailed discussion on the different mechanism that could explain the results as well as areas of further improvements. Finally, chapter 7 concludes the thesis with a summary of the work along with its significance. It also provides suggestions for further work that could improve the accuracy of the model

2 Literature Review

2.1 Introduction

Wear processes present a severe challenge in industry. This is because wear reduces the useful life of machine components and thus, replacing machine components prove costly [6]. The friction of worn-out surfaces of these components does have an influence on the wear processes. The mechanism of these processes mainly depends on mechanical properties and physical geometries of the surfaces in contact and the type of load applied [7]. However, changes in these processes have been rigorously observed in the past with the help of the emitted noise generated at the point of contact [3, 4]. For example, the calculation of the sound pressure can be performed by the Boundary Element Method at a high computational cost [8]. This is due to the high number of harmonic components associated with the friction-induced vibrations. Efforts have been made to reduce the computational cost associated with the Boundary Element Method by performing partial computations using only the dominant harmonic components as opposed to full harmonic components though they remain more costly than Finite Element Methods [9]. The studies of acoustic emissions are mostly done on disc brake systems as this is an area of industry where noise reduction is especially important for the consumers. However, most of these past efforts are based on empirical relationships [10].

More often, these relationships are accurate in lab-based experiments and generate wear measurements under real operating conditions [11]. For instance, wear occurring under unlubricated conditions can be readily measured and extended in practical applications outside of the lab. Furthermore, many wear processes can also be reasonably explained and then applied in industrial applications. However, their accuracy remains in question when machines with several worn-out components are under investigation or when more complex situations arise (such as the use of lubrication) with differences possibly within several orders. This is because integrating all the different mechanisms by which wear occurs into a unified wear model is problematic. Various mathematical models have been developed to account for friction and its

relationship with wear [12]. Combining friction models with wear models is important because, along with heat generation, the way frictional work dissipates is linked to roughness changes, wear particle generation, tribomaterial evolution, and microstructural alterations [13]. Having an identical friction coefficient does not necessarily indicate that the friction processes will be similar [14]. This is because the difference in the generation of wear can drastically alter the friction processes too. This might not be the case when the sliding distance is low, or the applied load is low or if the materials have been effectively lubricated. However, in most other cases, the mechanisms of wear generation will influence the frictional processes and those should be examined by embedding wear models into friction models. However, in these models, the acoustic emissions and the airborne noise are not included, which means that two fundamental components generated during the friction processes are still missing. Hence, they do not describe the true physics and interdependencies of friction, noise, and wear altogether.

Different reviews have been published on friction and friction-induced noise. Akay [15] published a review on various noise generation mechanisms that occur due to different friction processes. The review does not consider how the noise mechanisms will differ as wear starts to develop. Similarly, Pennestrì et al. [16] published a review on the most widespread friction models. They found most of these models are empirical by nature and they do not take wear into account. In industrial applications, Archard's wear model remains the most widely used model. Most of those are based on experimental evidence [17] and hence analytical work on friction and wear remains scarce.

So far, the published reviews treated friction, wear mechanics, and acoustic noise separately and an in-depth review that provides a critical analysis on their interdependencies is still missing. This chapter aims to provide a critical analysis on the existing friction, wear, and acoustic models and highlight the existing interdependencies between them. To get a fundamental understanding of the generation of wear and friction noise, this review first examines the mechanisms of contact at asperitical level. Then, a critical review of how the

frictional noise is altered due to the contact's mechanical properties under different wear conditions is provided. Finally, a survey of the existing friction and wear models is provided in the last section. This review will help to uncover the existing research gap. As of now, despite the interdependencies of friction, wear and noise being established, a comprehensive analytical model that incorporates all three of those components still has not been developed. A unified mathematical model that incorporates friction, wear, and noise could be a significant contribution to scientific knowledge as well as of significant practical use in industry, most notably in wear monitoring.

2.2 Concept of asperities and area of physical contact

The idea of the multi-asperitical contacts was first published by Bowden et al. [18]. They introduced the fact that friction between two rough surfaces is caused by the contact between the peak asperities i.e., Antagonist asperities. This shows that the real area of contact, which is the area of contact between the asperities of both the surfaces, is vastly different from the apparent area of contact as shown in Fig. 1

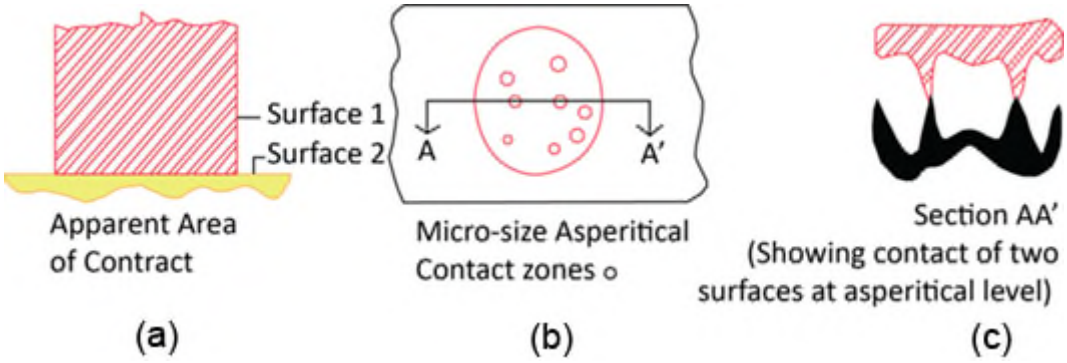

Figure 1: Apparent area of contact and real area of contact. (a) represents the area of contact as seen from a macroscopic point of view, (b) and (c) represent the contact area from a microscopic point of view, where the contact depends on the asperities located on both surfaces. (b) shows a top-down view, while (c) shows a cross-sectional view. Reproduced with permission from Ref. [19], © CRC 2004

Coulomb's first law of friction agrees as it states that the friction force is independent of the apparent area of contact but dependant on the real area of

contact [20]. In Bowden and Tabor's model, however, the number of asperities was assumed to be constant. Archard [21] refined the model by introducing a load-dependant number of asperities instead of a constant number. Greenwood and Williamson [22] further refined the model by introducing a Gaussian and an exponential distribution of asperities.

The molecular attraction between these asperities is one of the fundamental principles of friction and adhesive wear both for metals and polymers [20, 21]. Different models have been developed to determine the contact adhesion. The Johnson-Kendall-Roberts (JKR) model uses a modified Hertz model to account for the surface energy that causes attraction between the two surfaces in elastic solids. This is shown in Fig. 2. However, the solids must be perfectly smooth. The deformation caused by the attractive forces are so small that the surface roughness interferes a lot with the measurements. This model agreed with experimental results for soft surfaces such as rubber and gelatine, which, if pressed together, deform to such an extent that the surface roughness becomes negligible by comparison. Such is not the case with metals [23]. Another model (the DMT model) was developed to determine the influence of the contact deformation and the molecular attraction between a ball and a plane [24]. As the ball enters contact with the plane, the molecular van der Waals forces increase the contact area as the forces are attractive. The adhesion force was found to be proportional to the work done per unit area required in breaking the contact between the two surfaces. However, even though the contact area increases due to the van der Waal's forces, the force required in breaking up the contact does not increase. It can thus be calculated from the non-deformed contact as shown in Fig. 2. R_1 and R_2 are the radius of the spheres, δ is the elastic displacement due to the surface forces and P_0 is the applied load. Another comparative analysis was done by Johnson and Greenwood [25]. It was shown that the JKR adhesion theory was valid for large spheres more suited to polymers whereas the DMT theory was more suited for small, micrometre-sized metals spheres, which are elastic. An improved model to account for the transition was also developed [26]. It uses the Lennard- Jones potential to show that the magnitude of the force required to separate the two

surfaces varied continuously between the surfaces described by the JKR model and those described by the DMT model. The Lennard-Jones potential is shown in Fig. 3.

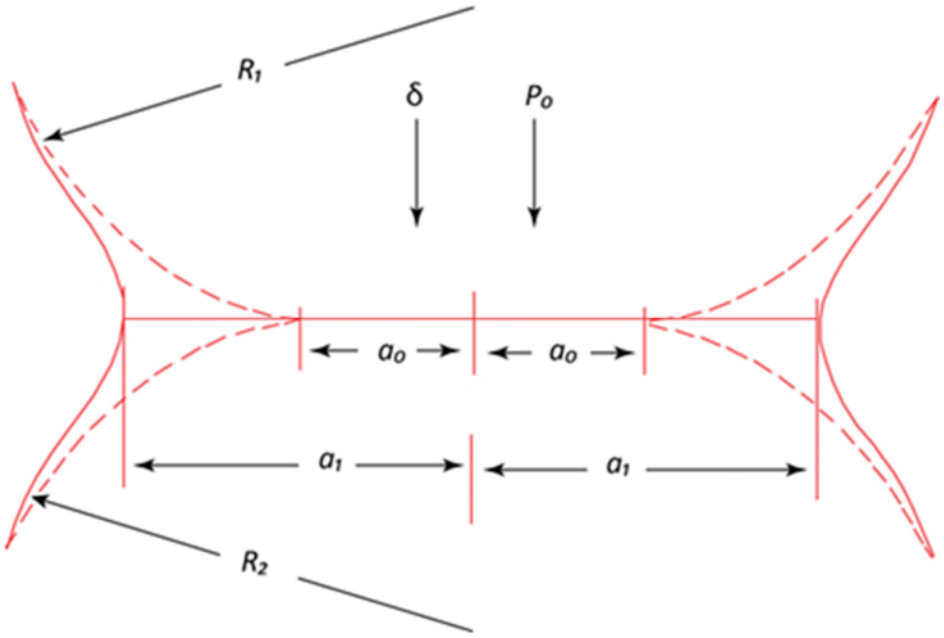

Figure 2: Contact between two elastic solids both in the presence (contact radius a_1) and absence (contact radius a_0) of surface forces. Reproduced with permission from Ref.[22], © Royal Society Publishing 1971

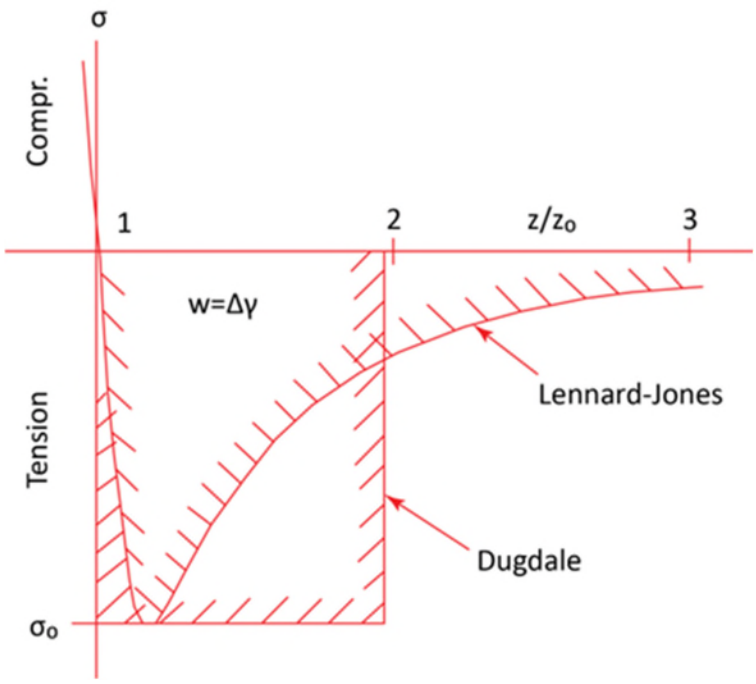

Figure 3: Lennard-Jones potential and the Dugdale approximation. Reproduced with permission from Ref.[25], © Elsevier 1994

Where σ = force, σ_0 = maximum tensile force, w = work of adhesion, γ = surface energy, and z = separation between the two planes and z_0 = equilibrium separation. There are no hysteresis forces that would cause permanent deformation. In the case of hysteresis, the work required to break apart the two surfaces is greater than the energy restored when the two surfaces come together.

The area of contact influences the surface roughness and thus, the generation of friction noise [27]. Simulations were also performed to correlate the real contact area with the surface roughness parameters [27, 28]. The effect of wear particles during the friction processes would influence the real area of contact [28] as shown in Fig. 4:

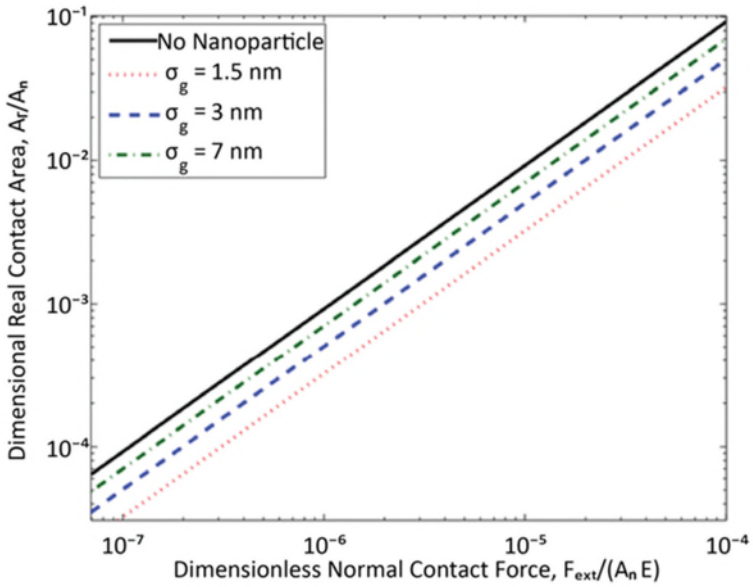

Figure 4: Effect of average particle size on real contact area. Reproduced with permission from Ref.[29], © ASME 2013

As the average size of the particles increase, the real contact area decreases. A decrease in the real area of contact introduces a decrease in friction. This is because the wear particles help in keeping the surfaces out of contact. However, there is a point of saturation. If the number of intermediate particles reaches the saturation point, then this leads to an increase in friction. The results were found to hold for abrasive wear particles only and it is not certain it would hold for other types of wear. The frictional heat generated by two surfaces under friction can provide an estimate for the real area of contact [29]. Assuming that the frictional heat power is constant, the measured temperature can be used as a constraint in a finite element model to determine the contact area as shown in figure 5.

The contact area increases due to an increase in the load and/or the sliding speed. However, the model used to calculate the contact area has some limitations. For example, it is only suitable for dry friction. In case of mixed/lubricated friction, the contact area effectively becomes zero. This is because the thermocouple requires conductance between the two surfaces. If the surfaces are not conductive or if there is a lubricant interference with the thermocouple, then this method fails.

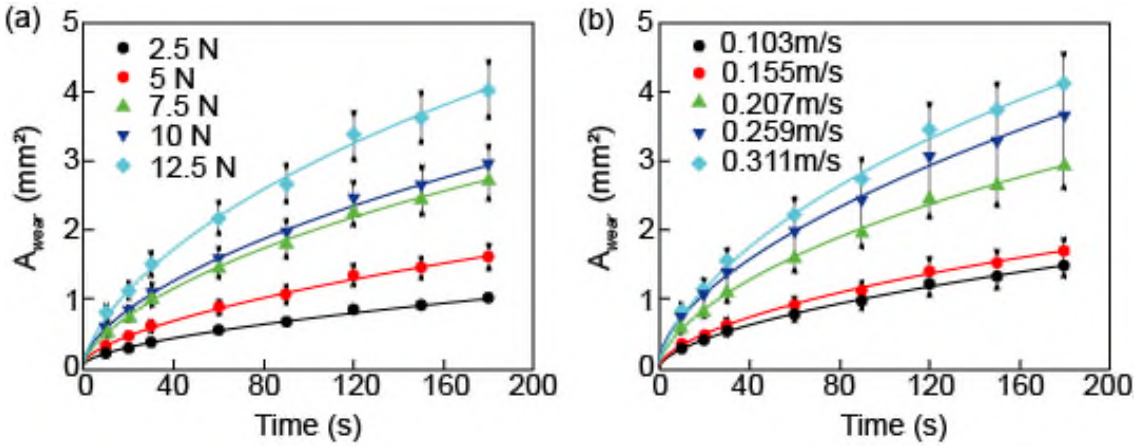

Figure 5: Wear area curve-fit result. (a) Load effect on wear area at a constant sliding speed of 0.207 m/s; (b) sliding speed effect on wear area at a constant load of 10 N. Reproduced with permission from Ref.[30], © AIP Publishing LLC 2016

Song and Yan [30] investigated the relationship between the real area of contact and the contact force during the pre-sliding regime. A tangential load was applied to the contact interface in quasi-static state, and the magnitude of the static friction was obtained and correlated with the real contact area. The increasing quantity of the interconnecting asperities was proven to be the dominant factor that expands the real contact area. It also expands linearly with the increase in static friction under a constant normal pressure in the pre-sliding regime. As the normal pressure increases and the static friction decreases, the real contact also changes.

The research shows that the real contact area is highly dependent on the number of asperities that are contacting on both surfaces. However, so far, there is no conclusive research as to how the number of contacting asperities will change with the change of friction or wear processes. To understand how the asperities and the change in asperitical contacts will influence the wear and the friction processes, it is necessary to investigate the friction processes at the microscopic level.

2.3 Relationship between friction and wear at the microscopic level

Although wear can be measured from a macroscopic point of view, the physical area of contact is particularly important to quantify the relationship between the wear and the friction. As such, it is necessary to go down to asperitical levels. At those levels, there are two main wear mechanisms that take place: adhesive wear and abrasive wear. Adhesive wear is caused when the contact between the two antagonist asperities has enough intermolecular attraction so that the asperities resist the sliding or demonstrate friction. The contact region of the asperities dislocates under compression and shearing [31]. A crack is initiated and propagated, and a wear particle is formed when the crack reaches the contact interface. The wear particle may then adhere to one of the surfaces as shown in Fig. 6.

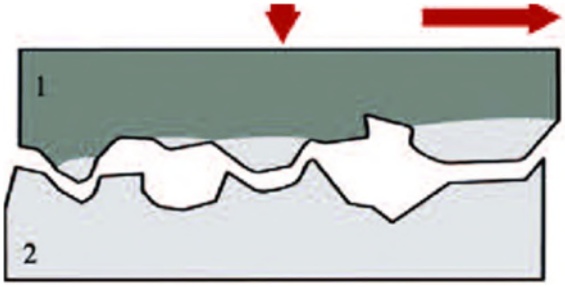

Figure 6: Adhesive wear mechanism

Abrasive wear occurs when the hardness of one asperitical surface is higher than the other as shown in Fig. 7. This causes one surface to plough through the other. This mechanism resists the possible sliding, and this shows the impact that friction has in abrasive wear. There are three different abrasive wear modes: microcutting, wedge-forming and ploughing as shown in Fig. 8. Under low friction, microcutting is more common. Higher friction will cause wedge-forming [32].

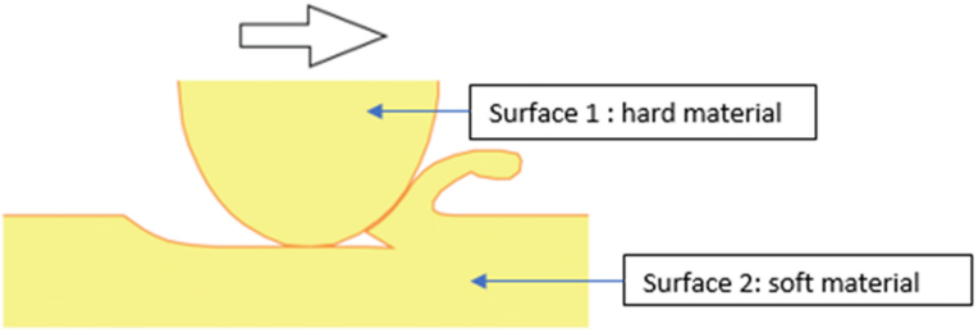

Figure 7: Abrasive Wear mechanism

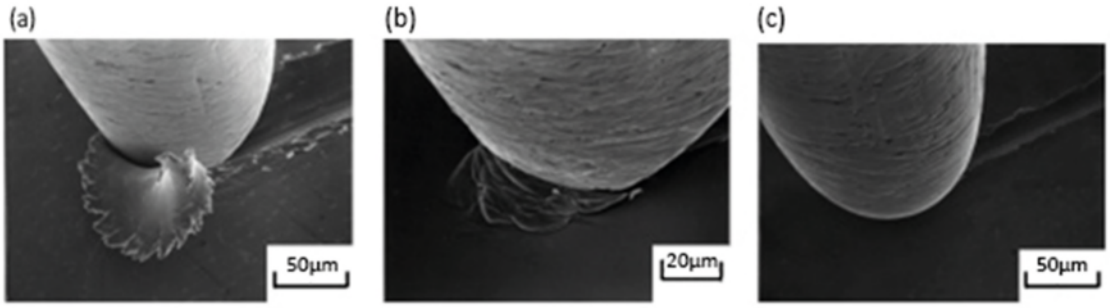

Figure 8: SEM images of the abrasive wear modes: (a) microcutting, (b) wedge-forming, and (c) ploughing. Reproduced with permission from Ref.[33], © CRC Press 2001

Several experimental and numerical studies have been performed to describe the details of the relationship between friction and wear. Aghababaei et al. [33] studied the correlation between the microscopic wear debris generated between two asperities on contacting surfaces. They performed simulations consisting of millions of atoms under friction-based contact with different sizes, and boundary conditions as shown in Fig. 9. The volume of wear debris generated was found to be proportional to the tangential work done on the surfaces (that is, the product of the tangential force applied and the sliding distance). However, there were no correlations found between the volume of the wear debris generated and the normal force applied at the debris level.

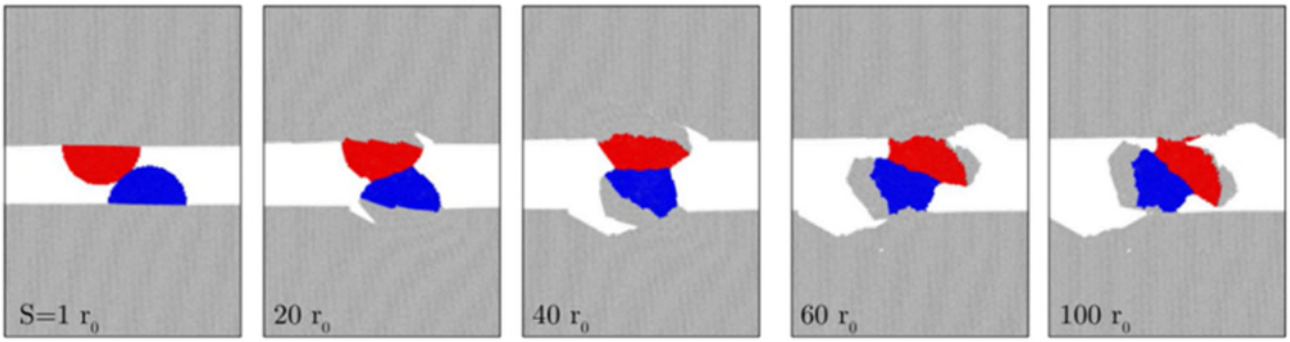

Figure 9: Debris Formation at the asperity level. Reproduced with permission from Ref.[34], © PNAS 2017

Myshkin and Kovalev [34] developed a precision tribometer with a normal load range from 1 mN to 1 N and velocity range from 0.1 to 10 mm/s. They conducted an experiment using a steel 52100 ball against a silicon substrate. The friction coefficient was then plotted against the number of cycles as shown in Fig. 10:

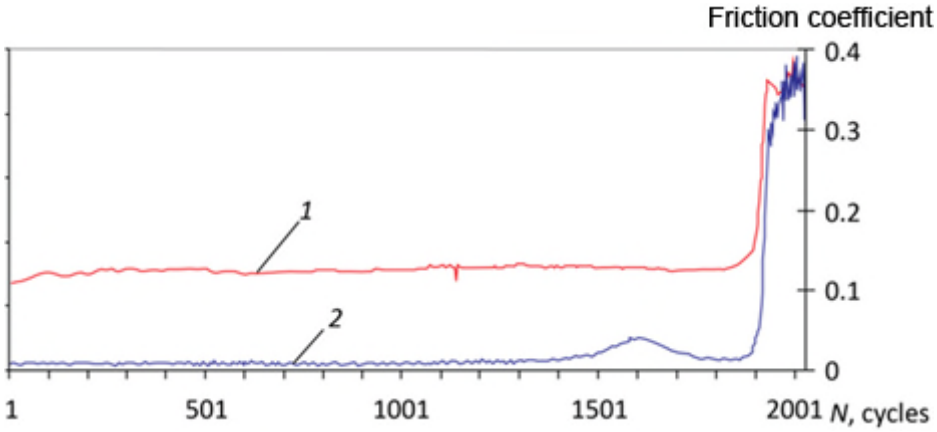

Figure 10: Friction coefficient vs number of test cycles. Reproduced with permission from Ref.[21], © Imperial College Press 2009

Where “2” in Fig. 10 shows the results with the material coated in the SEBS (Styrene Ethyl butylene Styrene) coating, and “1” in Fig. 10 shows the material with no coating. There is a large increase in the friction coefficient. This implies that wear develops as the number of cycles increases.

However, to comprehend how the friction processes and the wear that ensue lead to the generation of friction noise, it is necessary to go down to asperitical

level. At such levels, the contact parameters become a lot more important. These include the properties of the contacts as well as their geometries. How those influence the asperity distributions will lead to changes in the vibrations and the sound generation.

2.4 Origin of friction noise and its dependencies on contacts mechanical properties and geometries

Friction noise is generated during any friction process. Friction transmits energy from one surface to another as well as dissipating energy of relative motion. On the microscale, friction converts kinetic energy to thermal energy and thus acts as a dissipation mechanism. This process involves the oscillations of atoms. As we go to asperitical levels, If the system supplies more energy that can be dissipated, an instability is observed, which results in the generation of friction sound [35]. Friction sounds are unsteady and transient and depend on many different factors. Friction sound can emanate from one or both components of the friction pair or from some other parts of the system.

Fundamentally, during the sliding processes, the influence of the contact force reaches beyond the contact interface. The friction pair becomes a coupled system and the friction-induced vibrations caused by system instabilities resonate at their fundamental frequencies and harmonics. For example, in the typical wine glass example, the glass will resonate at its fundamental frequency when a wetted finger passes on the rim. Spurr [36] performed an experiment that showed that the wine glass had a dominant vibrational frequency that corresponded to its natural frequency. This is shown in Fig. 11:

The ring had a strong peak at about 1150 cps. The other peaks were at integral multiples of this frequency. This corresponds to the different modes of the natural frequency.

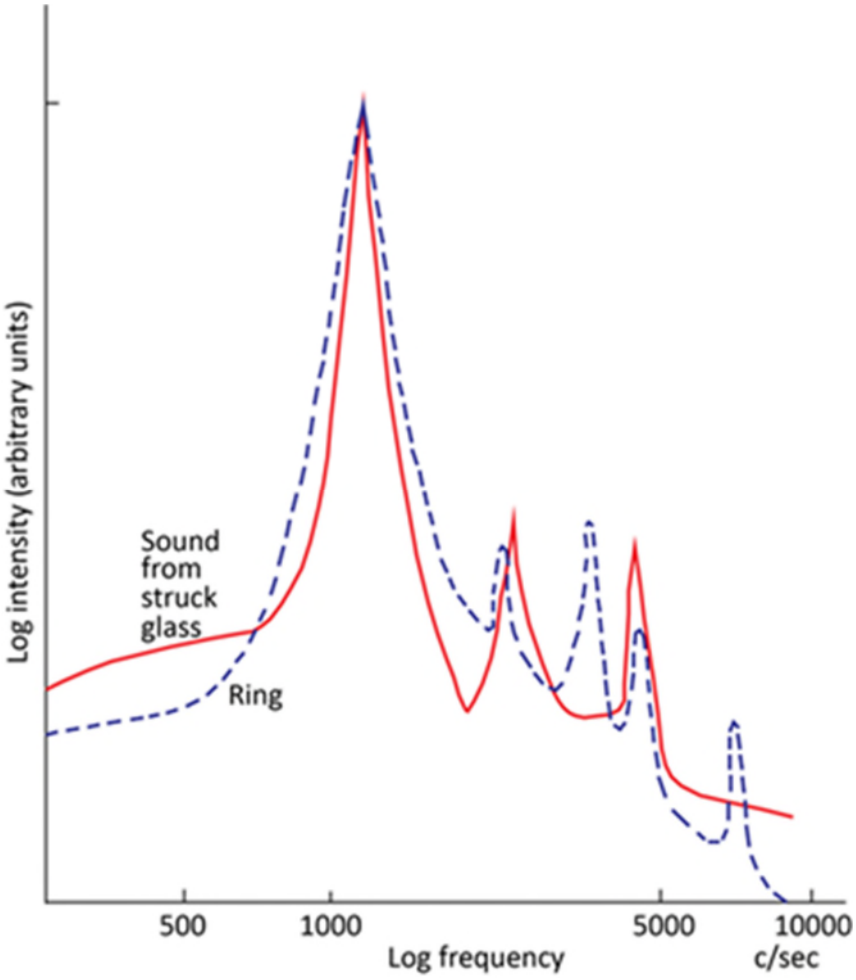

Figure 11: Frequency spectra of ring and of sound emitted by struck glass. Reproduced with permission from Ref.[36], © Elsevier 1961

The instabilities that result in the generation of friction sound can be caused by several different mechanisms. They can be related to geometric instabilities, to the material non-linearities, to instabilities caused by decreasing friction, which occurs in increasing velocities, or they can be caused by thermoelastic instabilities [37]. Those instabilities are created because of a variation in contact forces that occurs in a system. One notable example would be disc-brake systems. The contact forces will change as the disc is worn out or as the disc expands as heat is generated. Both those factors will contribute to the reduced effectiveness of the brake system; thus, mitigation of the heat generation and the wear generation is important.

The generation of friction noise mostly depend on the variation of the contact forces at the interface, which will influence the contact area. Those are dependent on the properties of the contact interface. For instance, an elastic material such as rubber can result in large deformation when a contact force is applied. This will result in a large contact area and that will lead to a certain sound spectrum. Conversely, a hard material like steel will not deform like rubber when the contact force is applied. The contact area would therefore be different and thus, the sound generation will also be different [38]. For example, one major area of study is in the disc brake systems and the squeal noise generated. Kinkaid et al. [39] provided a comprehensive review of the different models that could explain squeal generation in brake systems. Müller and Ostermeyer [40] extended the two-dimensional cellular automaton model to create a three-dimensional cellular automaton model to describe the interdependencies of friction and wear in brake systems. The topography of the brake pads changes based on the temperatures and pressure along with the external load applied. Based on those measurements and the Cellular Automata simulations, the interdependencies between the friction and the wear of the brake pads can be established. An increase in the load causes a higher surface roughness profile and higher contact areas up until a certain point. Further increases in the load no longer alters the topography much. Ostermeyer [41] also further investigated the lateral dynamics of brake systems under wear. Due to the increasing local normal and tangential stresses occurring around the areas where the wear particles are formed, the temperature also increases. This may lead to an alloying process between the hard particle and the wear particle, causing the formation of contact patches and different contact zones (the polymeric matrix for the brake material and the generated hard patches). The relationship between the friction and the wear will therefore depend on several factors which include the number and size of the contact patches as well as the temperature generated during the friction processes. Nishiwaki et al. [42] examined the possibilities of brake squeal reduction by refining not only the brake structures but also the materials of the brake pads. Two prototypes' materials were used as test prototypes, phenol formaldehyde resin and

polyamideimide (PAI). 500 tests were performed, and it was found that brake squeal occurred in 84% of the tests when the phenol formaldehyde resin binder was used. Conversely, brake squeal occurred in only 40% of the tests when the PAI binder was used. This is because one mechanism responsible for squeal is the variation of the friction coefficient. Replacement of the brake pad material leading to a smaller variation of the friction coefficient will result in less squeal noise. Chen and Bogy [43] created a numerical model for the interaction and friction forces on a hard drive system (the read-heard sliding on the magnetic disk). A pin-on-disk experiment was conducted by Earles and Lee [44] to validate their theoretical analysis. The frictional noise generated by a pin-on-disk system is caused by the dominant vibrational mode of the pin-disk subsystem. The pin-disk system was modelled as a three-degree of freedom model (parallel, normal, and rotational). Using this model, they could predict the regions of instabilities responsible for the squeal noise and it was validated experimentally.

This region of instability is called the kinematic constraint instability. Earles and Chambers [45] also studied how damping could be used to reduce the instability region. However, it was shown that damping could not reduce the magnitude of the instability.

Crolla and Lang [46] studied the effect of vibration induced noise on brake systems. They implemented an empirical approach on the modelling and design of brake systems as it was found that analytical solutions were not satisfactory and unfortunately did not meet industry requirements when it comes to squeal noise mitigation on the brake systems. They also focused on the commercial importance of reducing brake squeal noise due to growing customer complaints.

An analytical model was devised by Hervé et al. [47]. The model created was a two-degree-of-freedom model which was linearized. The equations of motion for the linearized model near the equilibrium region can be written as follows.

$$\boldsymbol{M\ddot{X} + D\ddot{X} + K\ddot{X} = 0} \qquad \textbf{(2-1)}$$

where ***M*** is the mass matrix, ***D*** is the damping matrix, and ***K*** is the stiffness matrix.

Ibrahim [48] provided a comprehensive review and discussed the different mechanisms that would lead to the generation of friction-induced noise. These include stick–slip, variable dynamic friction coefficient, sprag-slip, and different coupling mechanisms. The sprag-slip model assumes that the coefficient of friction is unrelated to the sliding velocity. It emphasises the fact that the source of the instability is due to the geometry [49]. Other models that use a constant coefficient of friction were devised by Ouyang and Mottershead [50]. The chaotic behaviour of friction was also discussed in the stick–slip phenomenon. The behaviour in such a phenomenon is not smooth and thus non-smooth systems can lead to chaotic behaviour. Chatter and squeal in friction processes [51] were also investigated in sliding systems such as water-lubricated bearings in ships or submarines, wheel/rail systems, disc brake systems and machine tools. Chaos is a special form of squeal caused by non-linear forces and it is still not completely understood. Oberst and Lou [52] studied the chaotic behaviour of a nonlinear brake system. Godfrey [53] also studied the friction force on pin-on-disc setups and their oscillations. Different materials were tested along with different lubricating conditions. Results showed that the coefficient of friction varies with continued sliding as shown in Fig. 12.

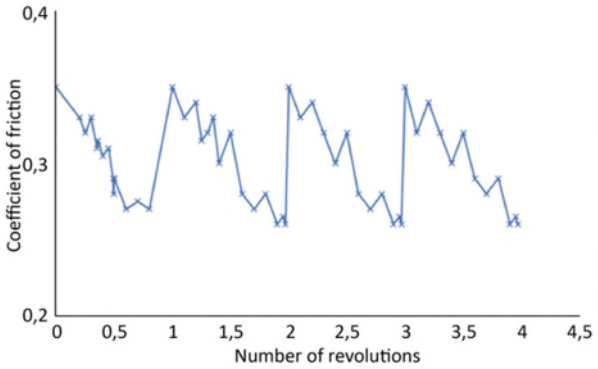

Figure 12: Coefficient of friction measured during the sliding wear experiment. Reproduced with permission from Ref.[53], © Elsevier 1995

Thus, it is more suitable to report the coefficient of friction as a range of values rather than a single nominal value. The friction oscillations varied because of

the lubricating conditions. They were small for good lubricants and large for poor quality lubricants [54]. Large material losses on the pin were associated with large friction oscillations while small material losses on the pin were associated with small friction oscillations. Further research including the surface roughness was performed by Yoon et al. [55].

Emira et al. [56] focused on the detection of stick–slip vibrations on a pin-on-disc experiment by using friction noise. The test rig was built so that the noise produced would be solely due to friction.

The stick–slip vibrations were predominant at high loads or high speeds. The characteristics of the noise produced can help to identify stick–slip vibrations as the spectrum of the noise includes high consecutive peaks. It can be easily seen as no noise is produced as stick occurs. This is shown in Fig. 13:

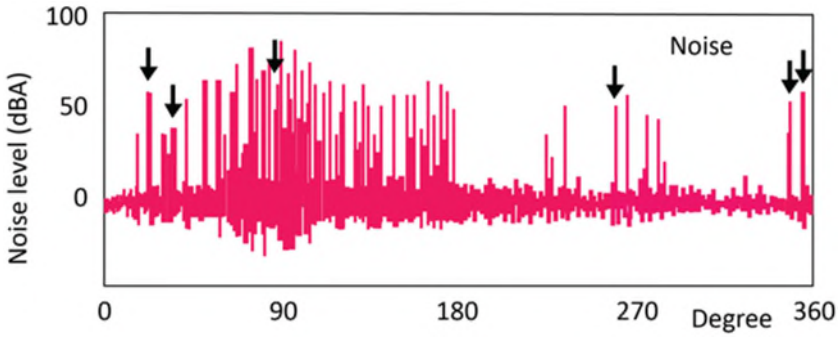

Figure 13: Measured induced noise (steel pin, normal load 40 N, Vpin = 5.2 m/s). Reproduced with permission from Ref.[56], © Academic Journals 2003

Stick–slip vibrations and chaos were also studied by Popp and Stelter [57] in which they studied self-excitations due to dry friction and the transition from a regular to a chaotic motion. The parameter dependencies were also investigated. Both numerical and experimental methods were used, and two types of models were considered. Simpler discrete models were investigated numerically whereas more complex, continuous models were investigated experimentally. The experimental models could then be compared to the numerical models. Those would allow to get better evidence of chaotic behaviour and to develop enhanced analysis techniques for noise generation. Abdo et al. [58] and Chowdhury et al. [59] included the effect of humidity and

the frequency of vibration on the amplitude of the stick–slip vibration. It was found that as the frequency increases, the amplitude of the vibrations decreases. Furthermore, humidity does have an impact at lower frequencies of vibrations, but they cease to have an impact after the frequency of vibrations reaches a higher value as shown in Fig. 14:

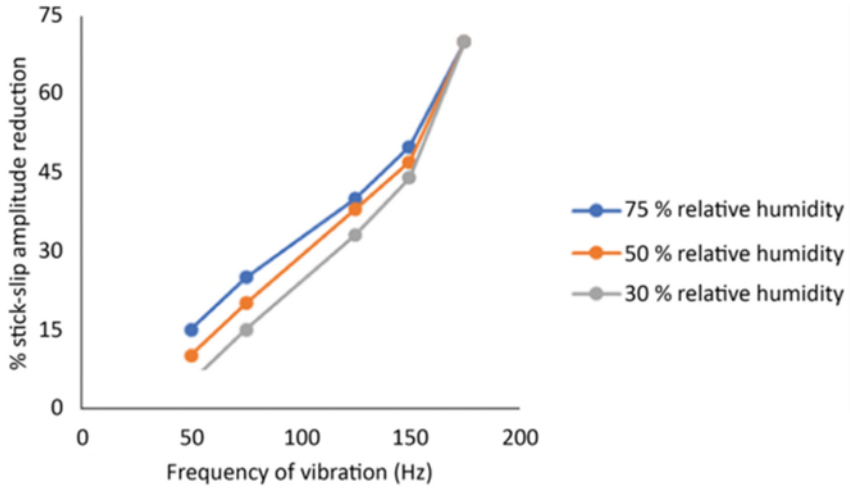

Figure 14: Percentage reduction of stick–slip amplitude as a function of frequency of vibration with relative humidity. Reproduced with permission from Ref.[59], © Bentham Open 2008

2.4.1 Friction Noise and Contact Geometries

Even if the materials are similar, the geometry will also have an impact on the generation of sound. There have been numerical and experimental studies to determine how the geometry would affect the frictional noise. It is important to note that adhesive wear is a major component of sound. This is due to the wear debris accumulating between the two surfaces. However, changing the geometry of the surfaces will change the distribution of the wear debris. For example, groove textured surfaces reduce the impact of the wear debris because of the increased space between the two surfaces [60]. The geometry can otherwise increase the noise generation because it can lead to a larger contact area between the two surfaces.

In most numerical studies, the surfaces are assumed to be perfect. Hence, Bonnay et al. [61] created a methodology to introduce geometric imperfections into the contacts. For example, it was assumed that the thickness of the disc was not uniform. They introduced a variation of the thickness as a function of the disc. The second geometric imperfection was the plateau as a function of the friction pad. The two geometric imperfections cause a variation in the noise generated due to the disc bumping as seen in Fig. 15.

A similar analysis regarding pad-on-discs systems was performed by Wang et al. [7]. Dynamic Transient Analysis using ABAQUS was performed as shown in Fig. 16.

The effect of groove-textured surfaces on the disc pad was investigated as shown in Fig. 17.

It was concluded that the geometry on the surface affected the noise generation. The sound pressure from the 90 degrees groove-textured surface was significantly lower than for the other surfaces. The 45 degrees and 135 degrees groove-textured surfaces had lower sound pressure than for the smooth surface and the 0 degrees groove-textured surface as seen in Fig. 18.

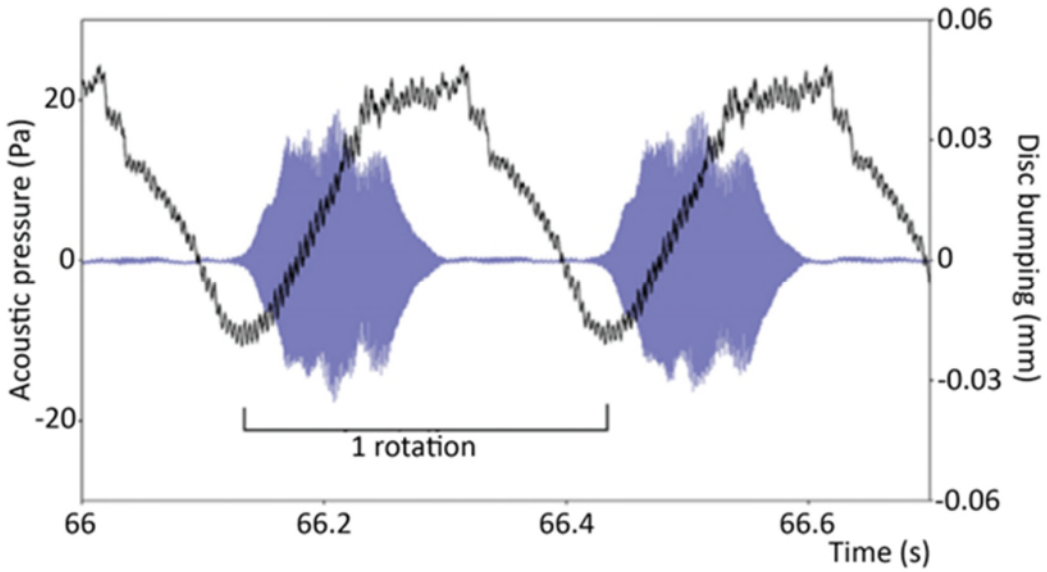

Figure 15: Correlation between disc bumping and squeal. Reproduced with permission from Ref.[61], © Elsevier 2015

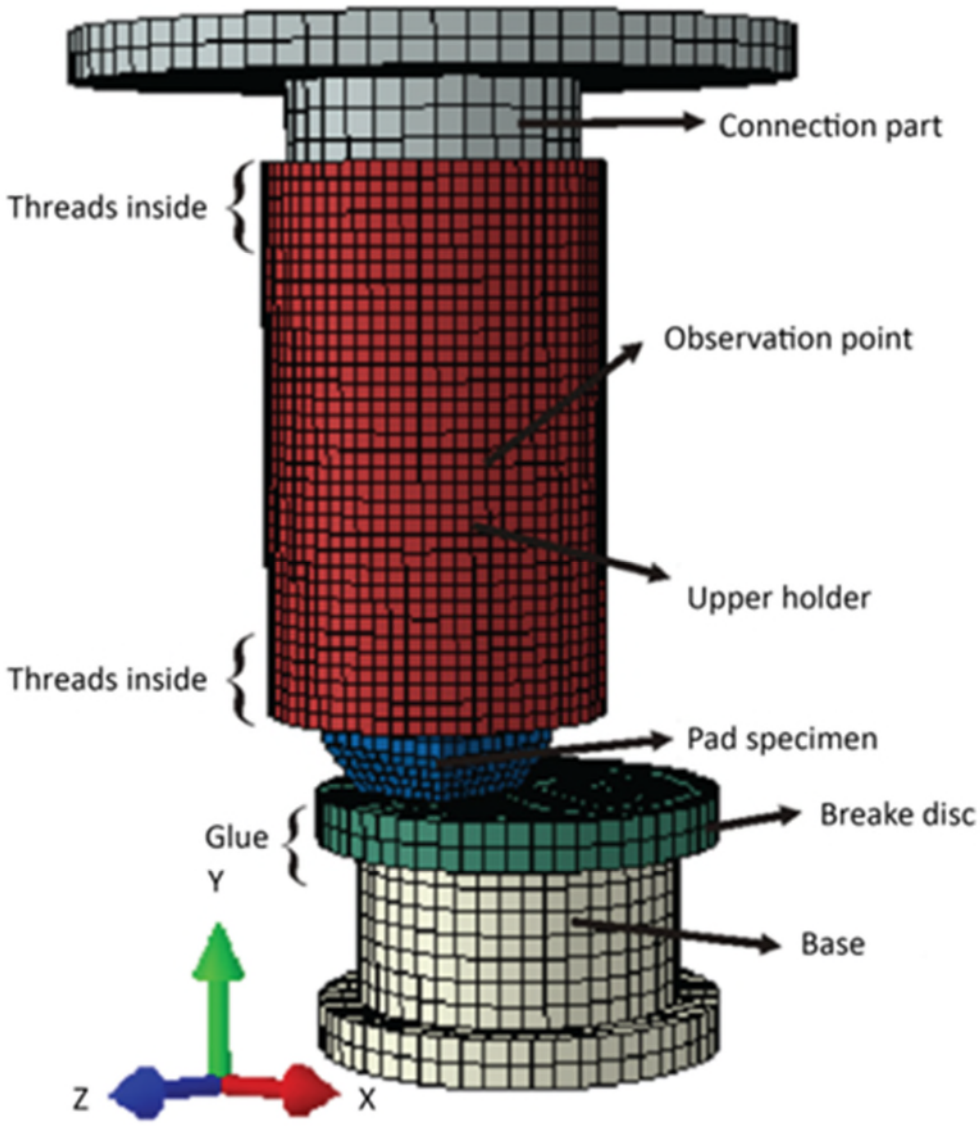

Figure 16: FE model of the experimental system. The FE analysis was performed using ABAQUS. The model represents a pad-on-disc system mostly used in the automobile industry. Using structural modifications allows for the reduction of friction induced noise. Reproduced with permission from Ref.[2], © ASME 2016

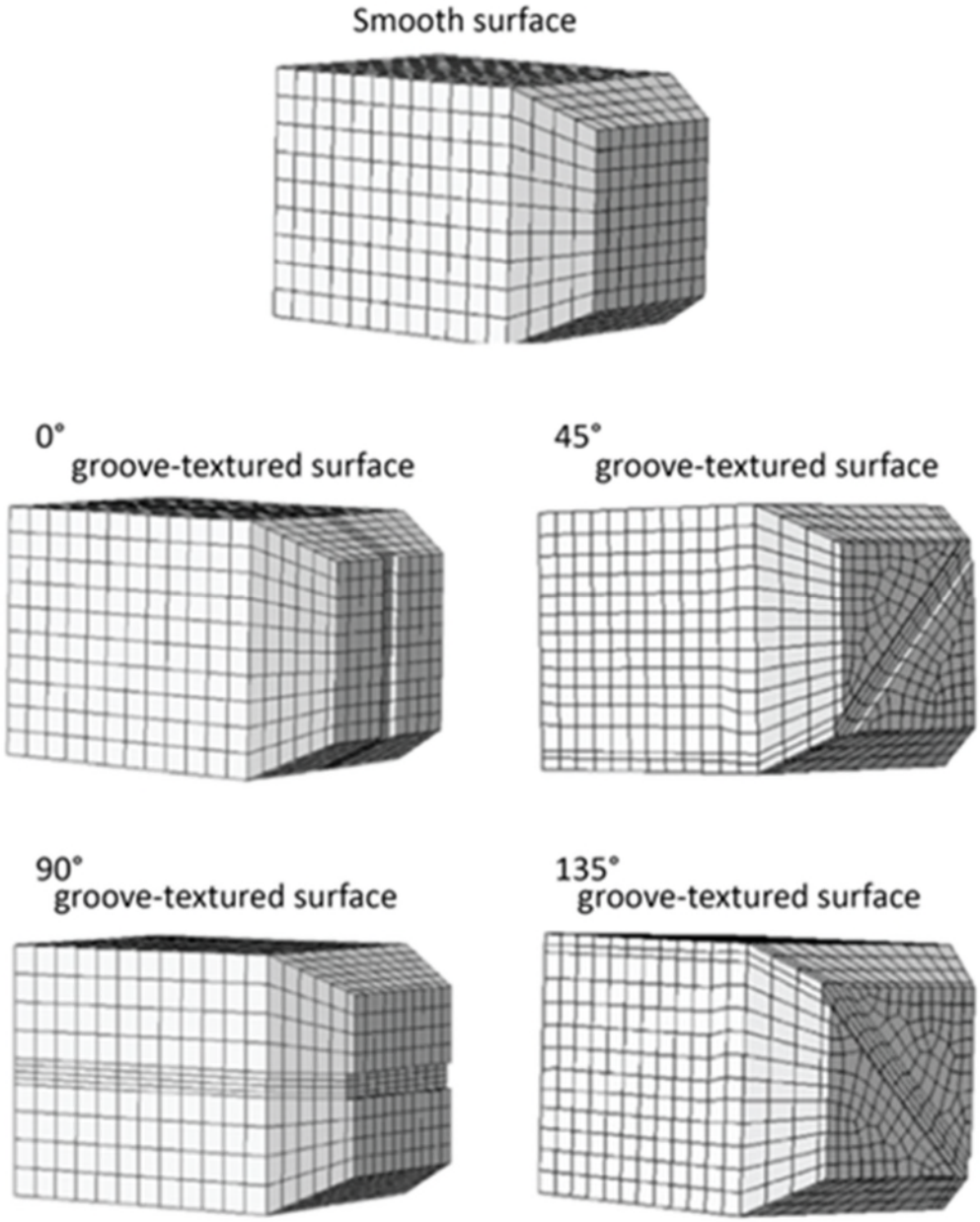

Figure 17: Five kinds of the pad surfaces. Reproduced with permission from Ref.[2]. © ASME 2016

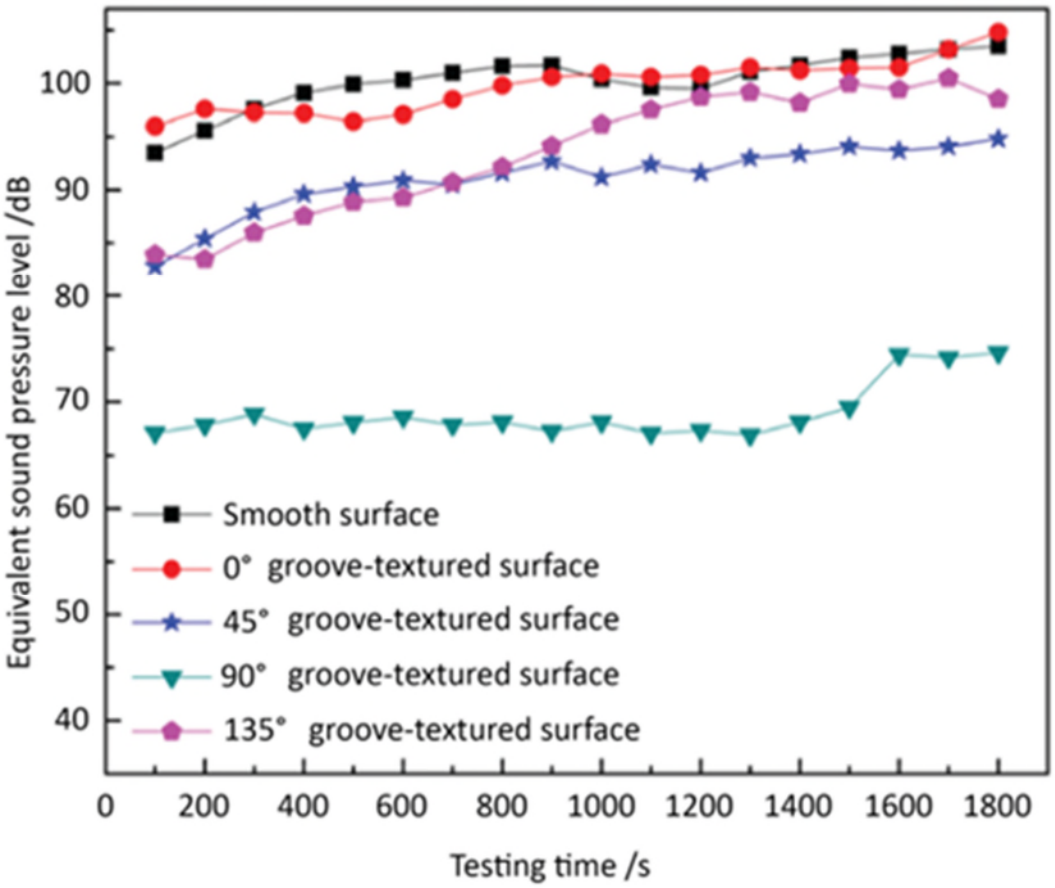

Figure 18: Equivalent Sound pressure level for five surfaces. Reproduced with permission from Ref.[2], ©ASME 2016

Jolivet et al. [62] studied the contribution of the differences in micro-geometry in gear tooth to the friction noise. To create those micro-geometries, two different finishing processes were applied to gear tooth while one was left unfinished. The surface of one gear tooth was powerhoned and the third one was grinded. The average amplitude of the noise spectrum for the unfinished gear tooth was higher than for the other two finishing processes (which are close). This is shown in Fig. 19. Those results demonstrate that finishing processes are very important for the reduction of friction noise. However, the difference between the friction noise of the two finishing processes used were minimal.

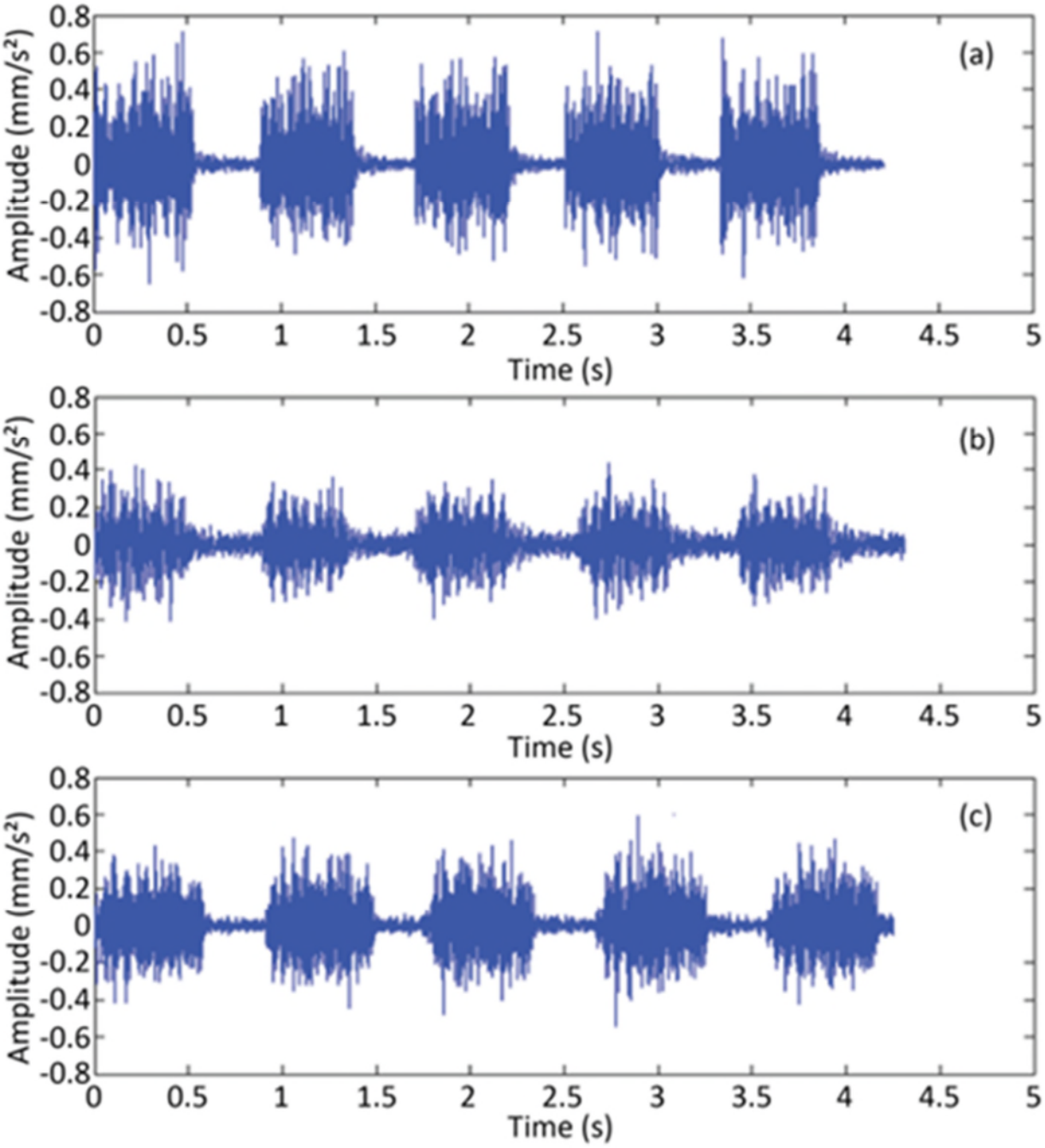

Figure 19: Measured raw vibratory signal at 10 mm/s for (a) not finished, (b) grinded, and (c) powerhoned tooth surfaces. Reproduced with permission from Ref.[62], © Elsevier 2017

2.4.2 Surface Roughness and friction noise

The accumulating wear debris leads to a change in the surface roughness of the sample. To study the relationships between the surface roughness and the

friction noise, the most common experimental setups consist of pin-on-discs experiments as they are the simplest to use and give an accurate description of real-world mechanisms.

2.4.2.1 Pin-on-disc based empirical research

Yokoi and Nakai [63] studied experimentally the frictional noise generated by a clamped rod rotating on a steel disk. It was concluded that the noise was generated because the coefficient of friction between the rod and the disk was small, and the sliding surface is rough. However, they found that as the sliding distance was increased, the surface of the disk became smoother which greatly increased the coefficient of friction which altered the sound pressure levels (as shown in Fig. 20). The sound pressure levels would increase as the friction increased.

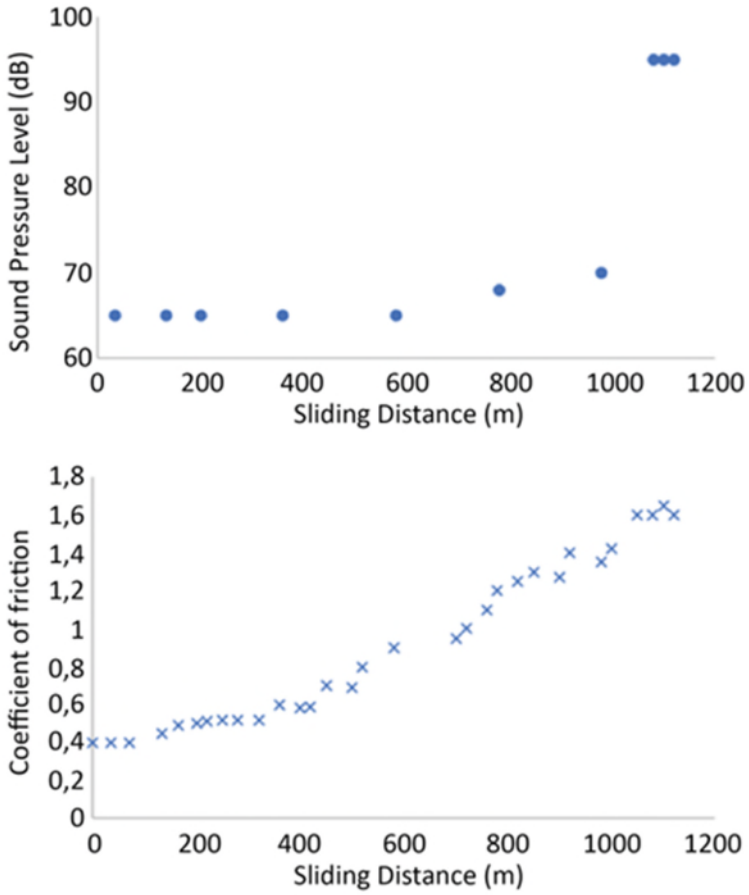

Figure 20: Coefficient of friction and sound pressure level versus sliding distance. Reproduced with permission from Ref.[63], © JSME 1979

There have been other attempts to experimentally determine the relationship between the rubbing noise and the surface roughness. Othman and Elkholy [64] devised a device to measure the roughness of a surface based on the frictional noise generated. It consists of a steel blade which has a tungsten carbide tip. The blade is inclined at an angle from the surface to be measured. The blade oscillates due to an electromagnetic exciter at a constant frequency inside a small anechoic chamber. The sound is detected by the microphone and the sound level is recorded by a sound meter.

The surface roughness could then be measured using the following equation:

$$R = A(SPL)^b \quad \textbf{(2-2)}$$

where R = surface roughness, SPL = sound pressure level, and A and b are experimental parameters.

The assumption made that if the frictional force is small enough to excite just the rod, then the generated frictional noise is proportional to the surface roughness. However, there are limitations to this assumption. If the frictional force increases and becomes too large, the whole system would be excited and the relationship between the frictional noise and the surface roughness would no longer be directly proportional.

Othman and Elkholy [65] also determined that regardless of surface roughness and contact load, the sound spectrum would always have a sharp peak (the dominant frequency) as shown in Fig. 21. The dominant frequency is dependent on the materials used in the pin-on-disc experiment. They also found that the magnitude of the dominant frequency is linearly proportional to the speed of sound in that material as shown in figure 21.

Yokoi and Nakai [66] also determined the influence of the surface roughness on the generation of noise on a pin-on-disc experiment. It was found that as the surface roughness increased, the sound pressure level also increased as shown in Fig. 22.

By considering the two different vibration modes of the pin, the acceleration of the pin was calculated, and they converted the acceleration of the pin to the sound pressure level. It was found that the largest peaks in the sound pressure level corresponded to the natural bending frequency of the pin.

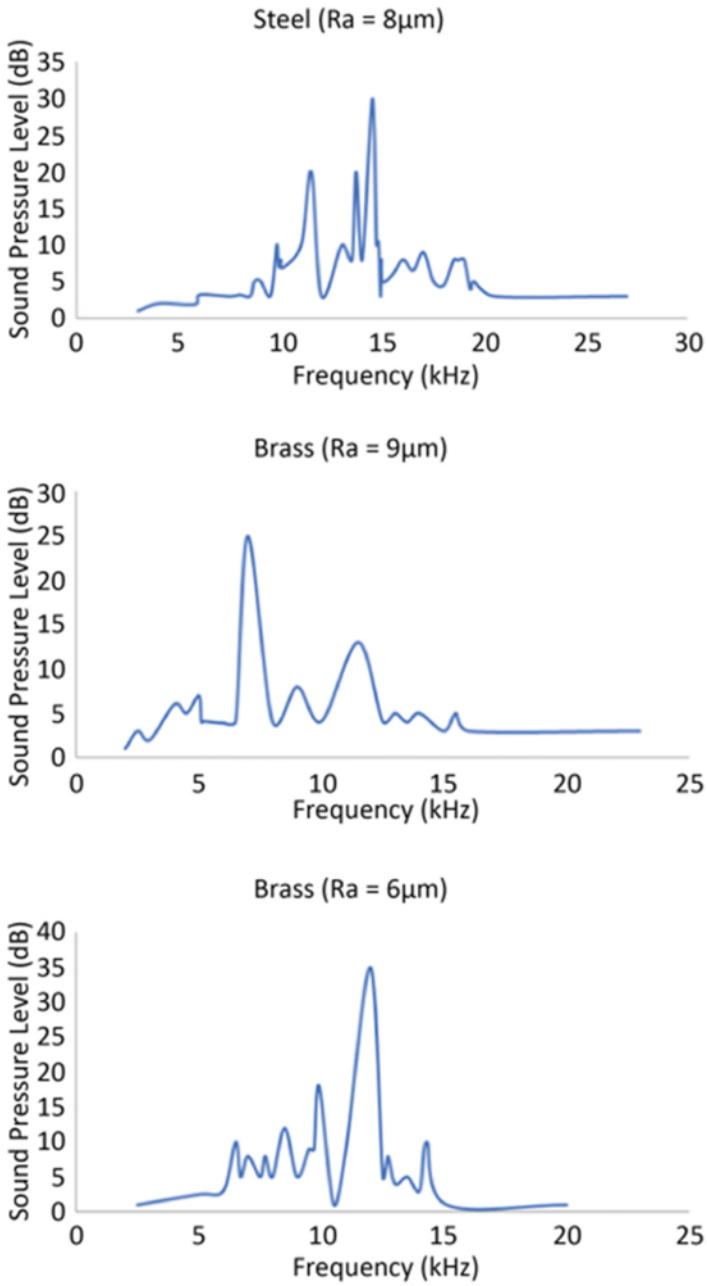

Figure 21: SPL spectrum in frequency domain for different materials (contact load = 0.50 N, all cases). Reproduced with permission from Ref.[65], © Springer 1990

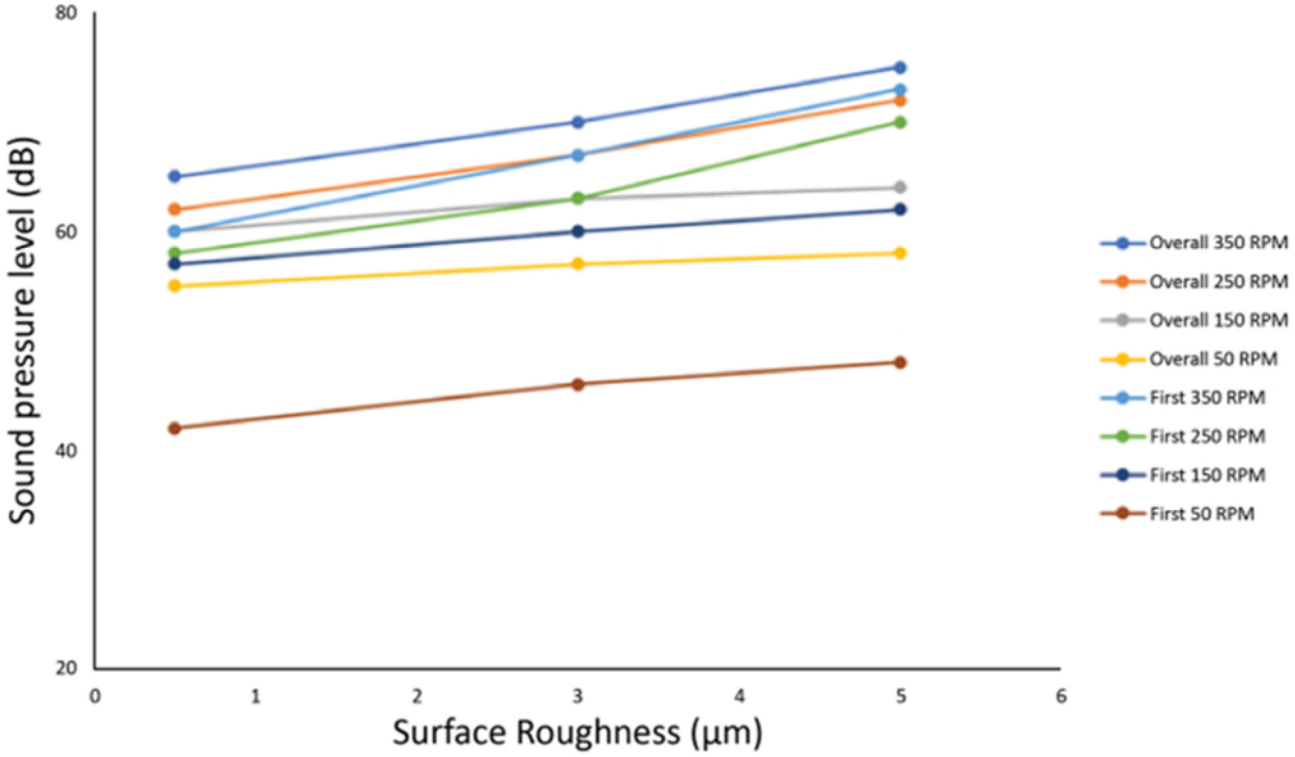

Figure 22: Relation between sound pressure level and surface roughness for various revolutions of the disk (Rod 3 cm in length. Reproduced with permission from Ref.[66], ©JSME 1982

By considering the two different vibration modes of the pin, the acceleration of the pin was calculated, and they converted the acceleration of the pin to the sound pressure level. It was found that the largest peaks in the sound pressure level corresponded to the natural bending frequency of the pin.

Stoimenov et al. [67] studied the frictional noise produced during the dry sliding of two flat-flat surfaces. The largest change of the sound spectrum peak due to the surface roughness was close to the fundamental natural bending frequency of the sample. This research therefore agrees with the previous pin-on-disk research which arrived at a similar conclusion. However, the experiment was not performed under constant load or sliding speed which could lead to a decrease in accuracy of the results as the sensitivity of the constant load or the sliding speed on the frequency of the frictional noise was not determined.

2.4.2.2 Simulation and Modelling

Rubbing noise was also studied numerically by Bem Abdelounis et al. [68].They used ABAQUS 2D to simulate the roughness noise. The noise was generated by the impacts between the antagonist asperities across the surface which then converted the kinetic energy of the impact to a vibrational energy which was responsible for the radiation of sound. It was shown that the sound pressure level was a function dependant on the logarithm of the surface roughness and the sliding speed as shown in the following equation.

$$\Delta Lv(dB) = 20\,log\left[\left(\frac{R_{a2}}{R_{a1}}\right)^{n}.\left(\frac{V_2}{V_1}\right)^{m}\right] \quad \textbf{(2-3)}$$

As the sliding speed and the surface roughness increases, the number of impacts per second decreases, but their intensity increases which leads to a higher intensity in the sound generated.

Earles and Lee [44] used modal analysis to analyse the behaviour of disc brake systems, most notably the generation of squeal noise. It was Jarvis and Mills [69] who first attempted to determine experimentally the generation of squeal noise. However, there were limitations with their model. For example, only one mode of vibration was considered. The system consisted of a pin supported in a way that it had two modes of oscillation. Those were one translational mode and one rotational mode. The model therefore had two degrees of freedom. However, it is possible to go even further. North created a ten-degrees-of-freedom model to represent the vibration of disc brakes [70]. Through these models, it becomes possible to predict the mechanisms that cause brakes to squeal and thus actions can be taken to minimise the squeal in disc brakes through changes in design.

Simo and Laursen [71] created numerical models involving contacts using the Augmented Lagrangian formulation. This is a penalty-based formulation in which the contact force is a function of contact stiffness. The higher the contact stiffness, the lower the penetration is. The Augmented Lagrangian formulation was also used by Hirmand et al. [72]. It is also a non-linear model in which the

Coulomb friction rule was implemented to simulate the stick–slip behaviour on the contact interface.

One of the major drawbacks of the numerical implementation of the Coulomb friction is the fact that the law is non-associative. This results in a non-symmetric mapping. However, most solvers are symmetric solvers such as Gaussian eliminations. Non-symmetric solvers do exist, but they are very computationally expensive. Laursen and Simo [73] worked on an adapted algorithm that would create a symmetrical Coulomb frictional problem that could then be applied to the Augmented Lagrangian formulation.

Oden and Martins [74] created numerical models for the stick–slip phenomena. Their models could be used to predict stick–slip, sliding resistance, and frictional damping. They divided the mechanisms of friction into 2 different categories. Type 1 friction was classified as quasi-static dry friction which has been investigated by other researchers prior. Type 2 friction was classified as dynamic sliding friction which includes stick–slip friction. However, their models had a few limitations as they did not account for the change in the coefficient of friction with velocity, nor did they consider the difference between the static and the dynamic coefficients of friction. However, it has been known for a long time that the coefficient of friction decreases as the sliding velocity increases [75].

Slavič et al. [76] devised a numerical model using Poisson impacts and the Coulomb laws of friction between random rough surfaces to investigate their effects on the roughness-induced vibrations. They also included the wear model and investigated the effects the wear would have on the frequency and amplitudes of the vibrations. The inclusion of wear would affect the dynamics of the system as the contact points would change and it would force other contacts to support the load. To devise their model, they started with a model consisting of one degree of freedom and one contact point. They later expanded their model to include 2 contact points and extended it again to include multiple contact points and thus simulate the whole system.

Another model was developed by Kang [77]. The model was focused on the stick–slip oscillation of disc brake systems and a time-transient analysis was

performed. The main difference between this model and the model developed by Jarvis and Mills is that this model uses non-linearized equations of motions whereas the one by Jarvis and Mills [69] used the linear equations of motions. This model is therefore more comprehensive than other models because linear models fail to account for the squeal generation far from the steady-state equilibrium.

As can be seen, the sound generated due to the friction processes change are highly dependent on the response of the system that the friction force interacts with. This interaction sets up a feedback between the friction force and the sound waves generated. Those dynamic effects have short time scales. However, there are other components with much longer time scales that will alter the friction and the sound generated. The wear of surfaces will have a major impact on the response of the system. Therefore, a simple linear system can still produce complicated responses as the time scale increases due to the deformation and the wear of the surfaces [15].

The models presented in this section shows a clear dependence between the wear and the friction noise as well as the friction coefficients. As wear starts to develop on the surfaces during sliding friction, the coefficient of friction greatly increases as the surface roughness of the surface is altered. This leads to an increase in the sound generated. There is also a dominant frequency in the sound spectrum irrespective of the sliding speed or the surface roughness. This dominant frequency is dependent on the material used. However, there are still gaps that need to be addressed. Most models presented are empirical. The numerical models use Coulomb's laws of friction as a basis. The analytical models presented in this section which establish the interdependence of friction coefficients and friction induced vibrations do not include an analytical expression for the wear calculations. As such, an analytical model that combines all three principal components of the friction processes has not yet been established.

2.5 Acoustic performance and noise due to wear

There are two distinct categories of noise generated during friction and wear processes. The acoustic noise and the airborne noise. This section details the process behind the airborne and the acoustic noise generated during the friction process. This section then describes the relationship between the acoustic/airborne noise and the wear that occurs during the friction process.

2.5.1 Airborne noise and wear

During the friction processes, energy is transferred due to the work done on the asperities. There are two types of deformation that can occur as a result. The asperities can either undergo plastic or elastic deformation. During elastic deformation, the energy is converted to noise. During plastic deformation, there is no noise component. However, the wear will contribute to the noise as the wear debris accumulate between the two surfaces as they create additional bodies that will impact the asperities and the impact energy will be converted to noise. This was also determined experimentally. Stoimenov and Kato [78] determined that wear had an impact on the generation of sound. In their experimental setup, adhesive wear occurred which caused a build-up of material on the surface of the disc. Those lumps of material (which were therefore higher than the original surface asperities) caused spikes in the sound spectrum that were correlated with the frequency at which the materials were attaching to the surface asperities during the sliding process. This research showed that friction generated a noise spectrum which was subsequently altered as wear occurred during the sliding process. The distance between subsequent spikes in the power spectrum were correlated with the distance between each lump of material. This is shown in Fig. 23.

Wang et al. [79] investigated the effect of surface roughness on the generation of squeal on a ball-on-flat surface. The ball was made of ceramic while the flat surface was made of graphite iron. All samples were polished and sandblasted to obtain a random surface roughness distribution. The smooth surface led to a higher sound pressure than the sandblasted surfaces. Squeal occurred due to the accumulating wear particles, ploughing, adhesion, and detachment which is

consistent with the previous research mentioned. However, the surface roughness had a major impact on the generation of squeal. The sandblasting of the surfaces caused a larger spread between asperities. Due to the larger distance between asperities in the sandblasted surfaces, the major mechanism of wear in those surfaces was due to ploughing. This possesses weak energy and thus leads to a lower sound spectrum. This confirms that wear debris and adhesion is a larger contributor to the high-frequency sound generation, which is what ultimately leads to squeal noise.

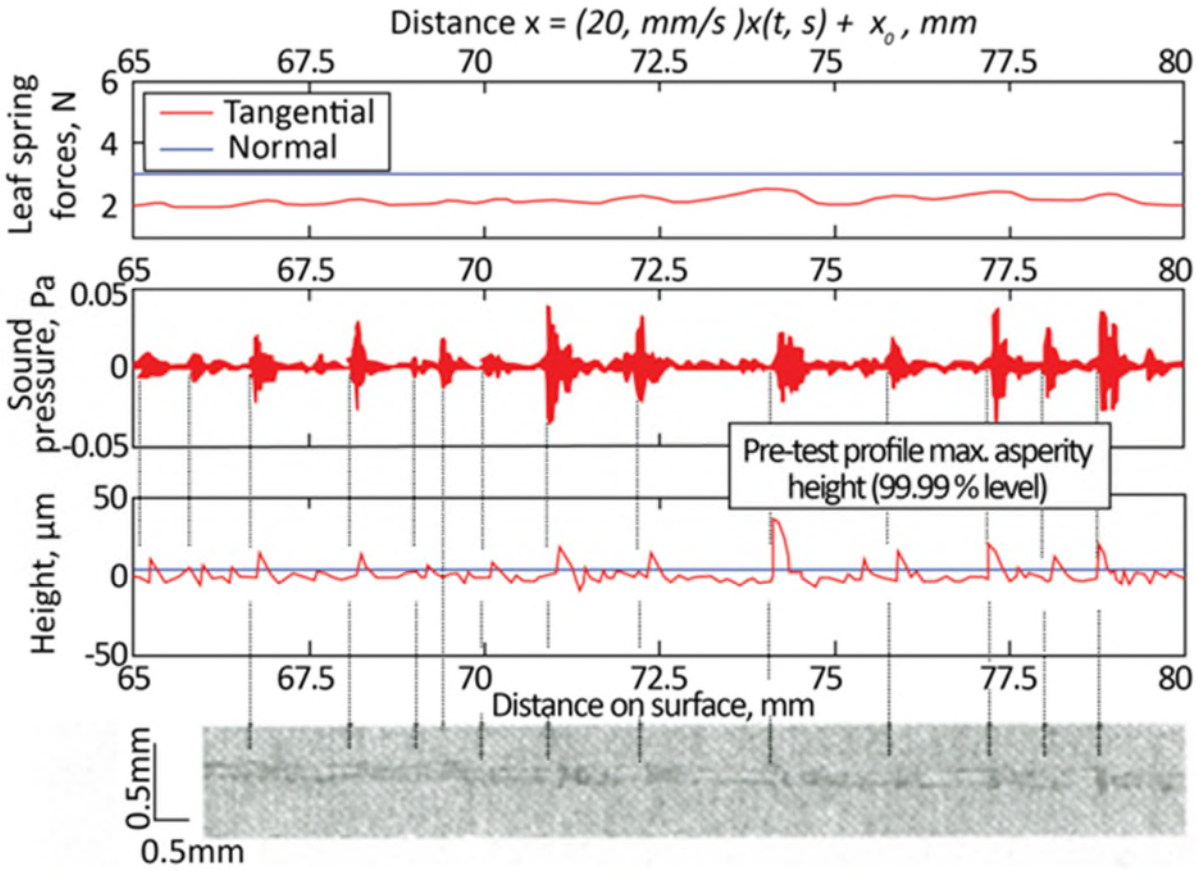

Figure 23: Zoomed-up portion of sound pressure signal at 3.0 N together with wear scar profile, scar photograph, and strain-gauge measured elastic forces. Reproduced with permission from Ref.[78], © Elsevier 2003

Since friction noise is closely related to wear, reducing wear would also reduce the friction noise. As such, Chen et al. [80] investigated how adding Titanium Silicocarbide to matrix composites would reduce the wear and by extension, the friction noise. Different proportions of Titanium silicocarbide were added to the

matrix composite. The samples tested included MT0 (no titanium silicocarbide added), MT5 (5 % added), MT10 (10 % added), and MT15 (15 % added). The results are shown in Fig. 24:

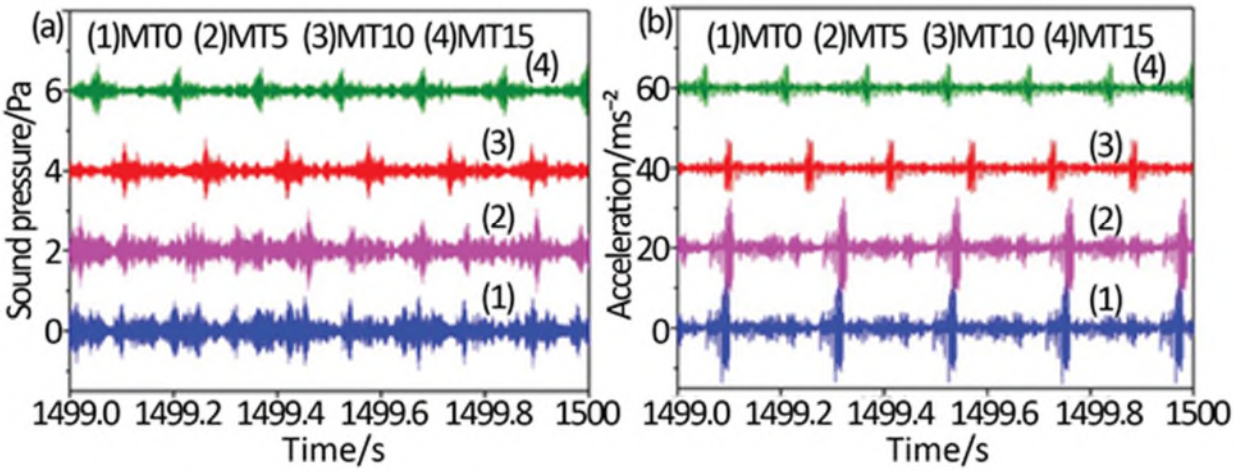

Figure 24: (a) Sound pressure and (b) vibration acceleration of MT0, MT5, MT10, and MT15 at 1,500 s. Reproduced with permission from Ref.[80], © IOP Publishing Ltd 2019

The sound pressure of MT0 was the highest. The main mechanism of wear in that sample was adhesive wear (electron microscopy shows the presence of wear debris on the surface). This therefore agrees with the previous research that adhesive wear was the largest contributor to friction noise. In MT5, the main mechanism of wear was abrasive wear. The surfaces still produced wear debris, but unlike in the first case, they did not immediately detach from the surface, but were instead compacted due to the role of cyclic stress. Because of this, they gradually repair the worn surfaces and as such, reduce the wear and the friction noise. MT10 was found by EDS analysis that there were many oxygen molecules present on the surface of the sample. This led to the conclusion that in this sample, the main wear mechanism was oxidation wear which does not contribute to the friction noise. Hence MT10 shows the least amount of noise. However, in MT15, adhesive wear becomes a factor again and so the noise level of MT15 is higher than for MT10.

The change in surface roughness also changes the sound pressure levels. This was shown by previous researchers [81]. However, an in-depth study of wear debris and contamination of the surfaces was also necessary. This would correlate the friction noise to the wear volume generated. Most of the research correlating wear with the coefficient of friction and friction noise has been experimental [82]. Nam et al. [83] studied experimentally the effect of lubricated contacts on friction noise. They compared two scenarios: One in which the lubricant was applied on the clean surface, and the second one where lubricant was applied on a surface contaminated by wear debris. Lubrication is used to mitigate friction and friction noise. However, as time progresses, the amount of lubricant between the two surfaces decreases. This leads to an increase in the friction coefficient and thus leads to an increase in friction noise as shown in Fig. 25.

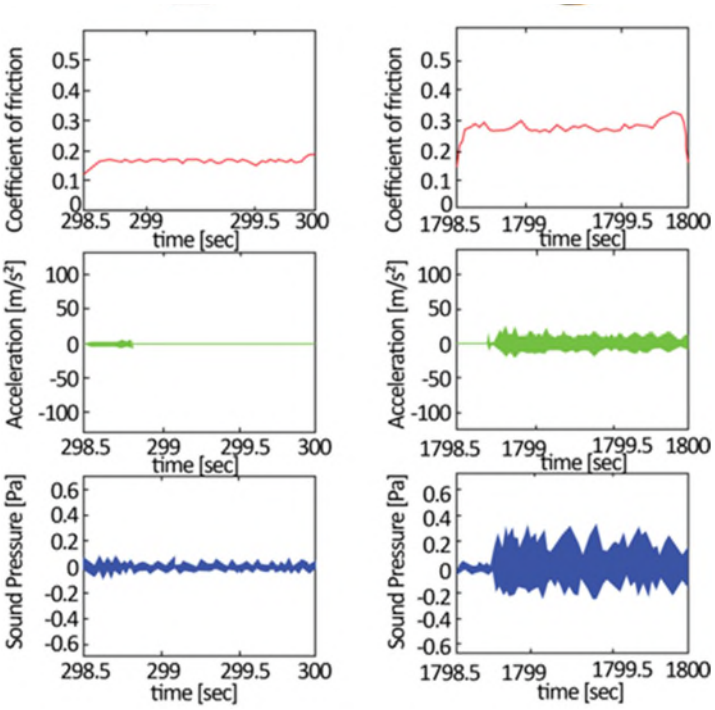

Figure 25: Surface Topology and time history of friction coefficient (top), vibration (middle) and sound pressure (bottom) for lubrication on the clean surface in the reciprocating test after (a) 298.5 s and (b) 1798.5 s. Reproduced with permission from Ref.[83], © Springer 2017

However, for the contaminated surface, there was no increase in friction coefficient despite an increase in noise (Fig. 26). This shows that wear does have an impact on friction noise.

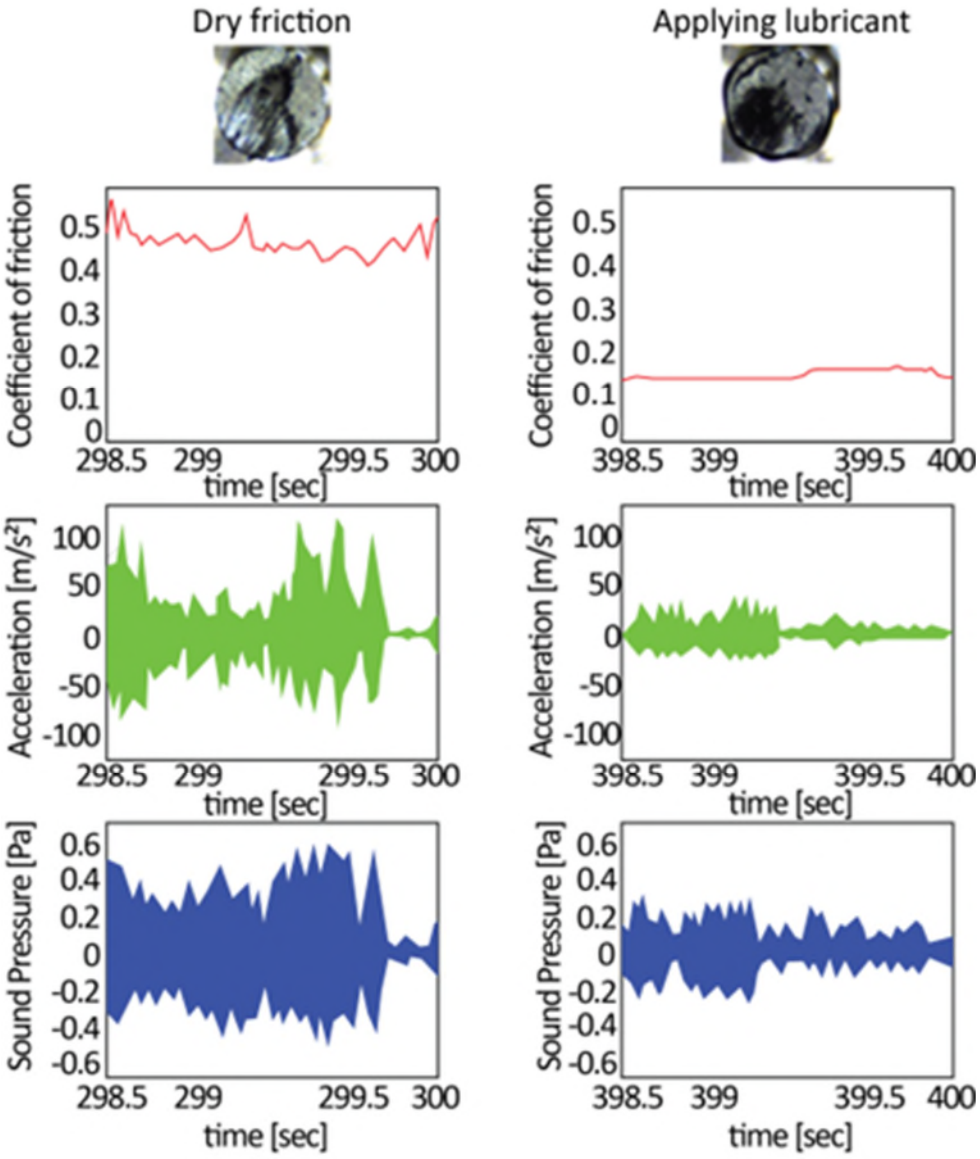

Figure 26: Surface Topology and time history of friction coefficient (top), vibration (middle) and sound pressure (bottom) for the contaminated lubrication by wear debris in the reciprocating test after (a) 298.5 s and (b) 598.5 s. Reproduced with permission from Ref.[83], © Springer 2017

Another research correlating wear and friction was performed by Mo, et al [84]. The experimental study was done on groove-textured surfaces. It was found that there was no correlation between the noise generated and the coefficient of

friction which agrees with other research [85].The noise was mainly generated due to the wear debris accumulating on the worn surfaces thus changing the topography of the surface. Groove-textured surfaces also generate less noise than smooth-surfaces as it allows the wear debris an easier escape from the contact points.

Chen et al. [86] categorised four different phases of squeal generation under wear. In the first stage, no squeal is emitted. In the second stage, squeal is not emitted as the coefficient of friction is too small. In the third stage as the coefficient of friction increases, squeal is emitted. On the final stage, the squeal disappears.

Several other researchers studied how temperature affected the wear rate [87–90]. For low temperatures, the wear rate was mostly constant. However, as the temperatures exceed a certain value, commonly 500 degrees Celsius, then the wear rate increases exponentially with increasing temperature (as shown in Fig. 27).

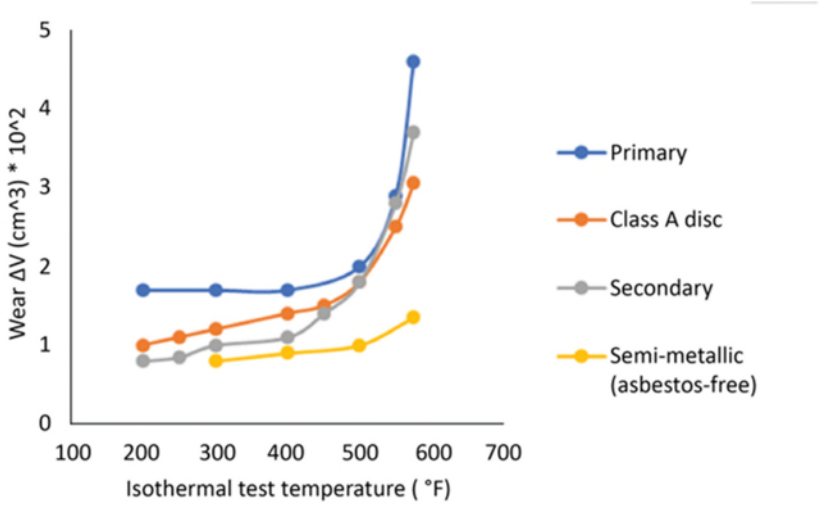

Figure 27: Variation in frictional wear with temperature. Reproduced with permission from Ref.[90], © Elsevier 1974

The role of wear in friction noise was also investigated by Duarte et al. [87]. They focused on the role of wear debris accumulating between the surfaces and developed a power spectrum model for the friction force. The presence of

loose debris has a strong impact on the friction force and the generation of friction noise. The experiment was carried out using an aluminium pin sliding on a steel disc. Two sets of experiments were performed. The first set was performed without the presence of debris whereas the second set was performed with wear debris blowing and accumulating between the surfaces as shown in Fig. 28.

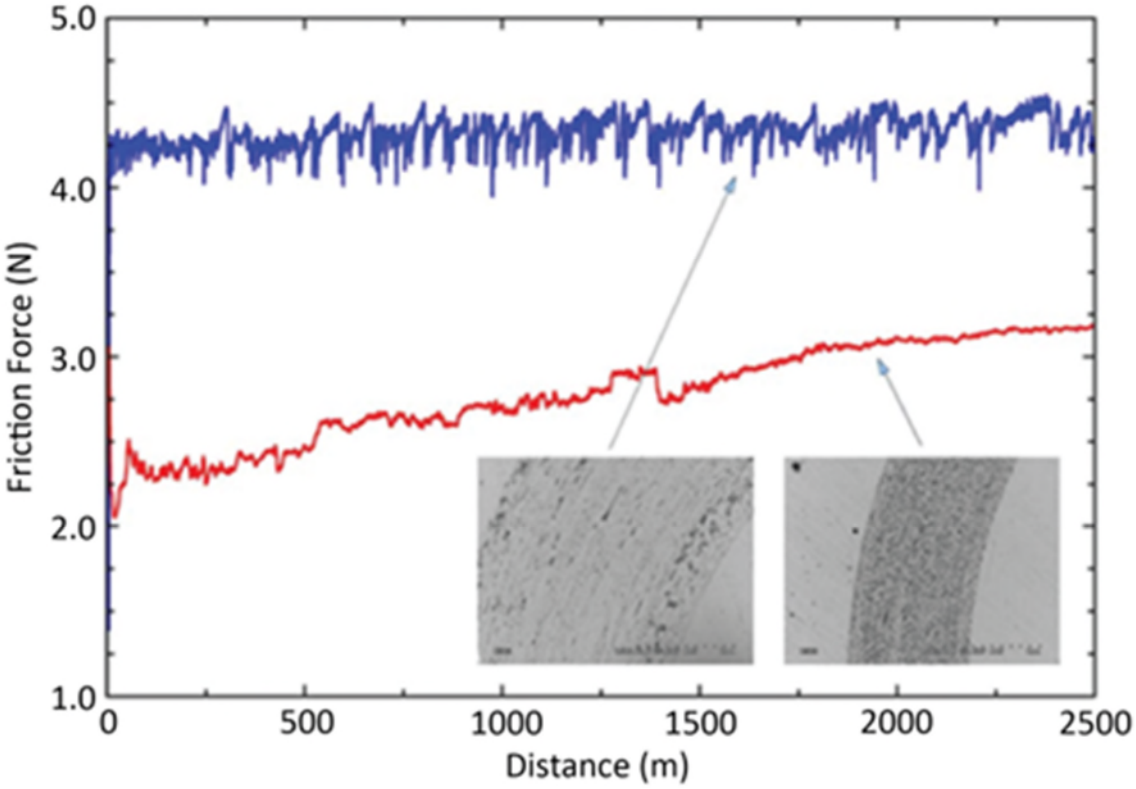

Figure 28: Running averages of the friction force vs time derived from experiments carried out on SAE 52100 steel with an alumina pin at a load of 5 N and a sliding speed of 10 cm/s. Data were taken at 20 Hz and averages were done over successive ranges of 50 s. Reproduced with permission from Ref.[90], © Elsevier 1974

Jibiki et al. [88] studied the friction noise that was caused by fretting. They used a crossed-cylinder configuration comprised of carbon steel and mild steel and calculated the friction force, as well as the noise that was generated during fretting. The fretting cycle consists of two phases: tension and compression. Friction noise only occurs during the tension phase, but never during the compression phase as shown in Fig. 29.

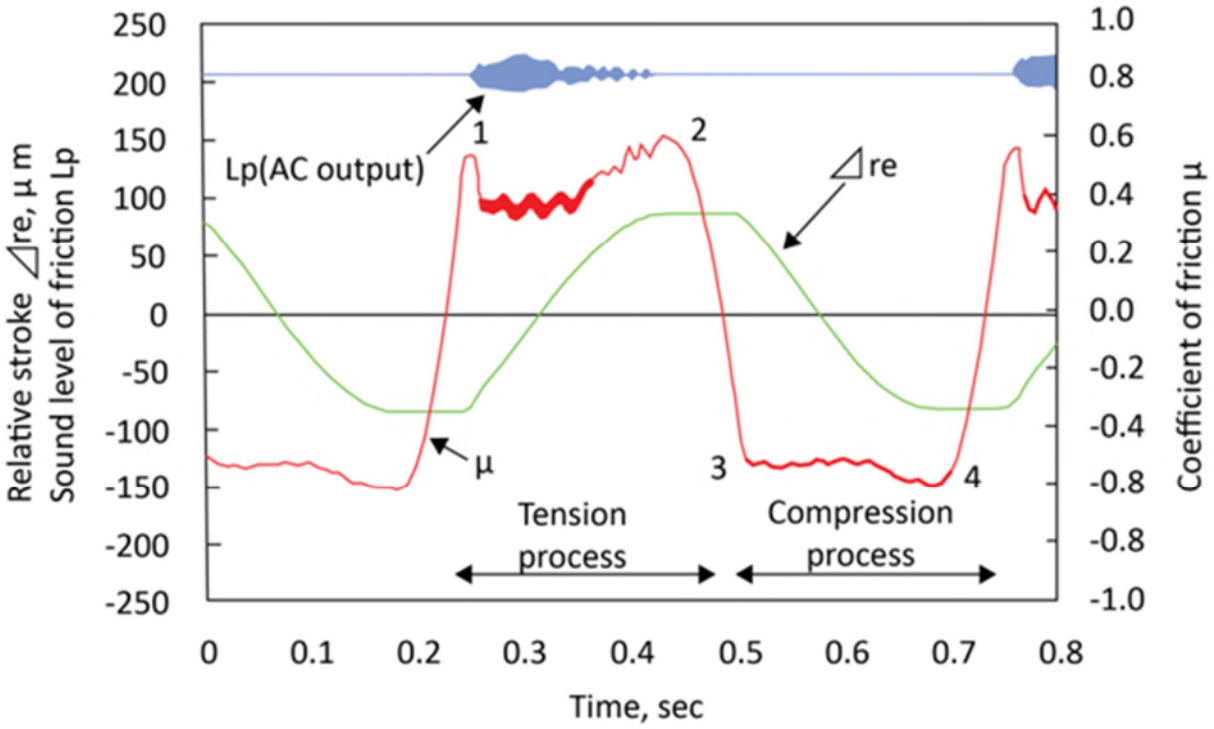

Figure 29: Typical example showing waveforms of friction noise (AC output), coefficient of friction, and relative stroke. Reproduced with permission from Ref.[92], © Elsevier 2001

Their model allowed to experimentally correlate the amount of wear and the friction noise. Several other studies examined how the accumulating wear debris would change the contact conditions [93, 94].

In summary, it was shown that the airborne noise was correlated to wear during the friction processes. For example, as wear increases, and the amount of wear debris accumulate, this leads to an increase in friction noise due to the wear debris. Temperatures also have an indirect impact on the friction noise. Higher temperatures directly increase the wear rate, and this leads to an increase in the friction noise. However, the coefficient of friction does not impact the generation of airborne noise. All the research presented in this section were experimental. A potential direction for future research could be to implement an analytical model of heat generation along with the friction and wear models. It would then be possible to apply it under a wider range of conditions

2.5.2 Effect of acoustic performance on the friction process

Acoustic emissions are transient elastic stress waves generated at the source by the rapid release of strain energy within a material. These radiating stress waves are detected at the surface of the body by a suitable transducer. Those can occur due to different phenomena such as asperity contact, micro-crack initiation and growth and plastic deformation. Those are the same phenomena that are linked to friction and wear. As such, it is possible to link wear to acoustic performance the same way it was linked to the noise. Boness and McBride [89] studied the acoustic emission produced under different wear conditions. This is shown in Fig. 30:

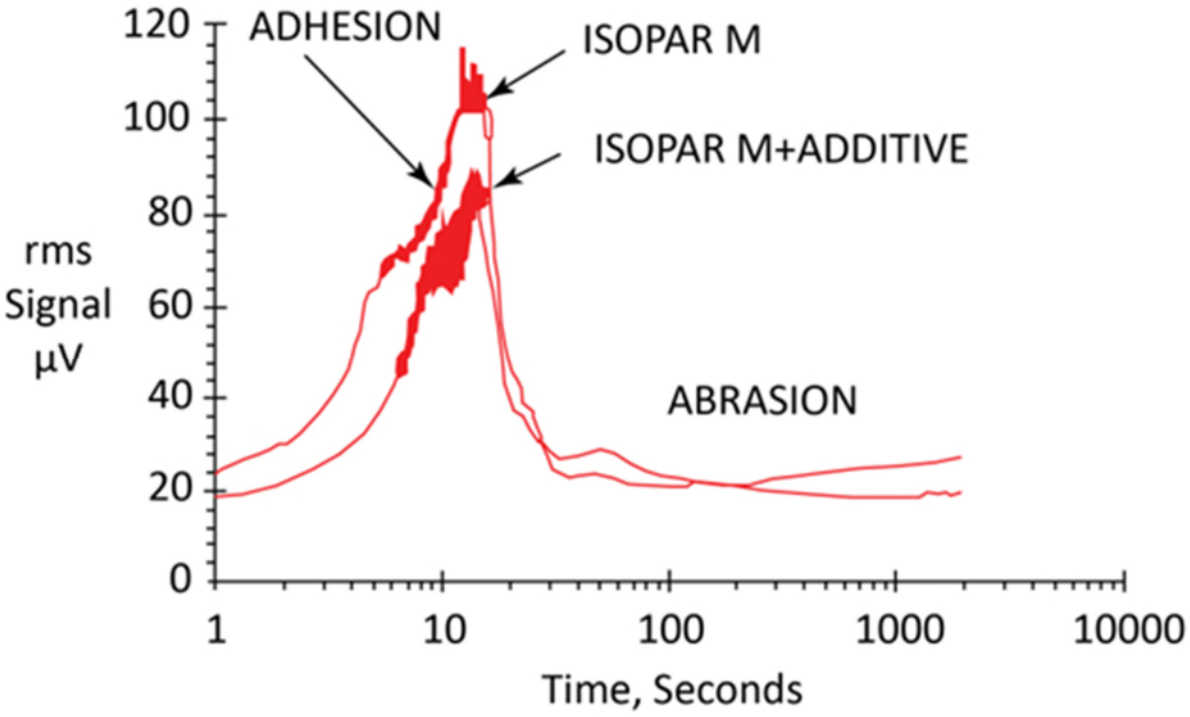

Figure 30: RMS signal vs. time. Reproduced with permission from Ref.[95], © Elsevier 1991

As can be seen from the figure, adhesive wear leads to a massive acoustic signal. During abrasive wear, the signal is a lot lower. This correlates with other research which suggest that adhesive wear is also what produces the higher noise as opposed to other wear mechanisms. It was also shown that adding third-body abrasive particles also reduces the acoustic emission produced as shown in Fig. 31:

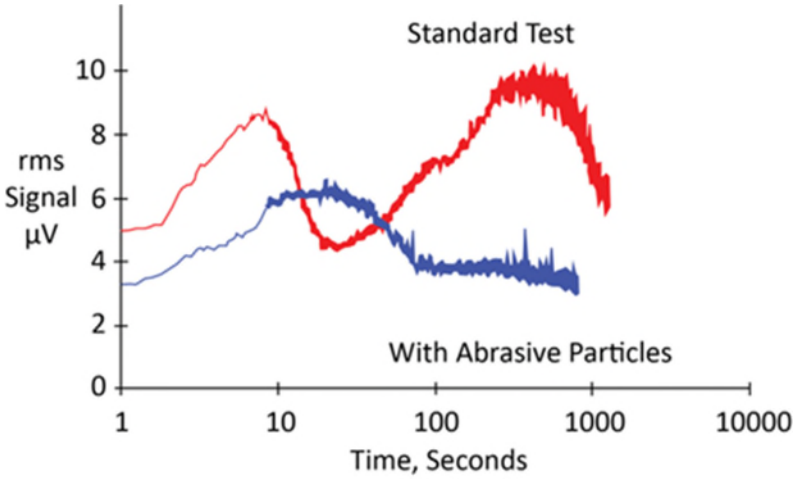

Figure 31: RMS signal vs. time. Reproduced with permission from Ref.[95], © Elsevier 1991

The RMS signal also increases a lot for the test without abrasive particles as opposed to the test with abrasive particles. Boness et al. [90] also studied how the acoustic emission varied between lubricated and unlubricated contacts. This is shown in Fig. 32:

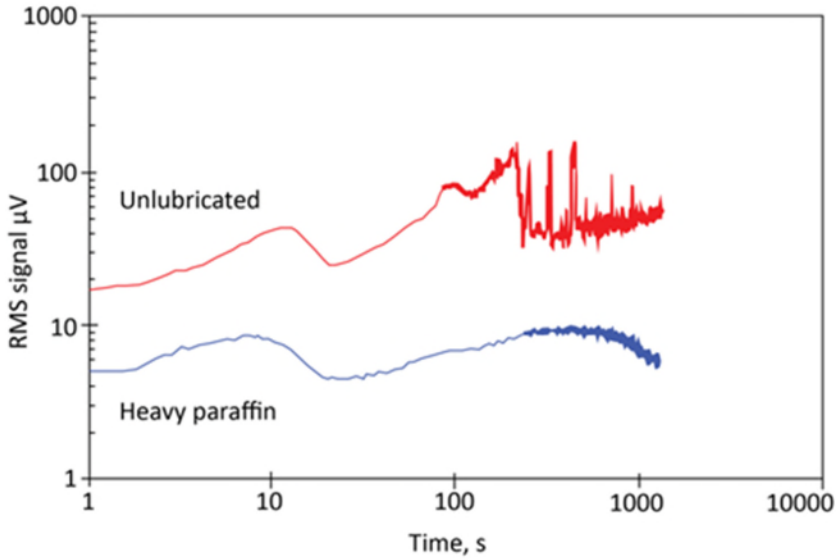

Figure 32: Acoustic emission – RMS vs. time. Reproduced with permission from Ref.[96], © Elsevier 1990

The RMS signal is much higher for unlubricated contacts than it is for lubricated contacts. This is also in correlation with the noise generation. Dry contacts lead

to a higher noise generation than lubricated contacts. The wear is also much higher, as shown in Fig. 33:

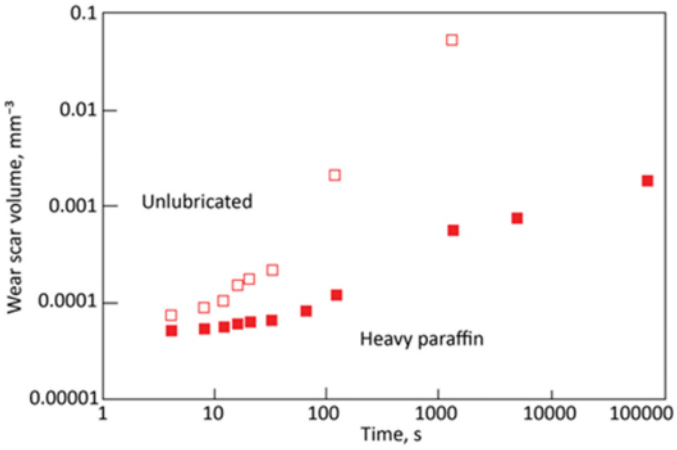

Figure 33: Wear scar volume vs. time. Reproduced with permission from Ref.[96], © Elsevier 1990

This agrees with other research that link an increase in wear to an increase in noise. Thus, an increase in acoustic emission will also lead to an increase in noise. Benabdallah and Aguilar [91] investigated the relationship between the acoustic emission and the friction and wear of the surfaces. This is shown in Fig. 34:

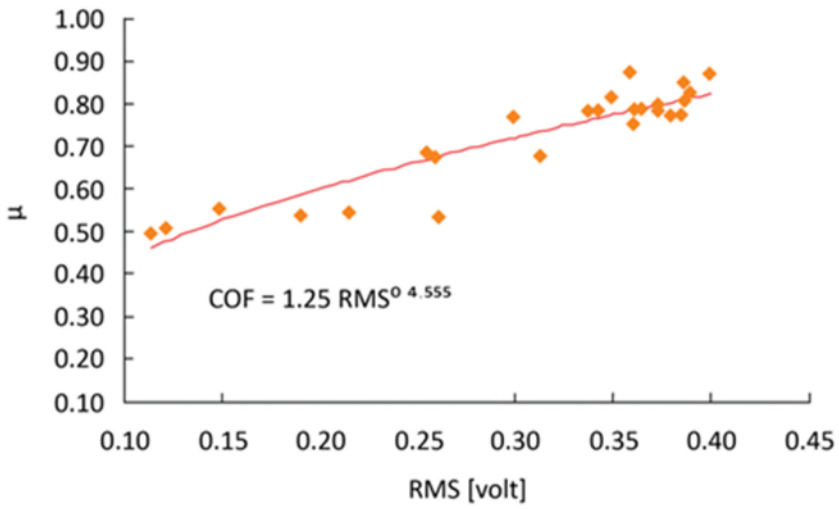

Figure 34: Relationship between COF and AE RMS voltage. Reproduced with permission from Ref.[97], © Informa UK Limited 2008

As the coefficient of friction increases, so too does the acoustic emission. The relationship between the frictional work and the wear rate are shown in Figs. 35 and 36:

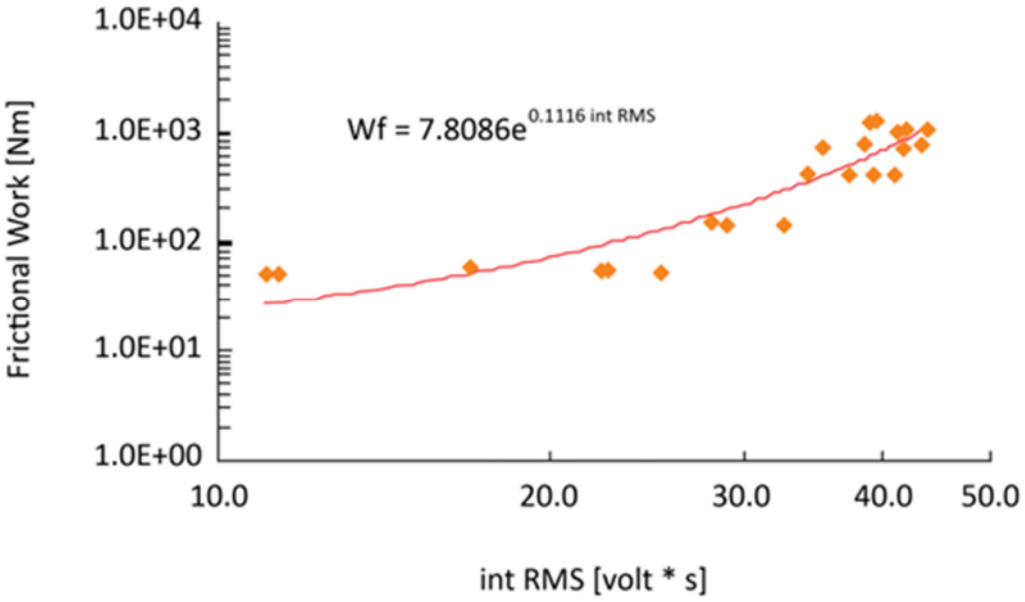

Figure 35: Frictional Work as a function of IntRMS. Reproduced with permission from Ref.[97], © Informa UK Limited 2008

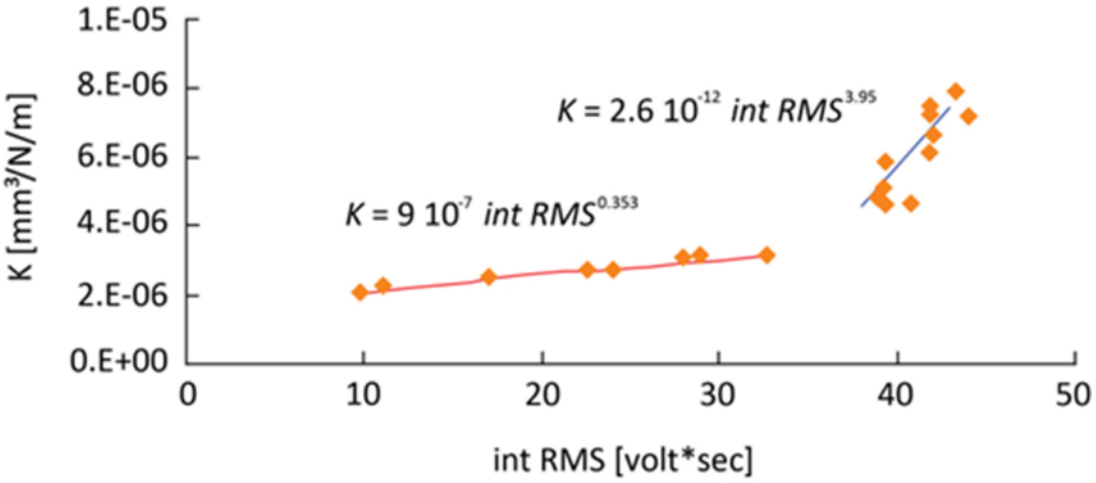

Figure 36: Wear rate as a function of Int RMS. Reproduced with permission from Ref.[97], © Informa UK Limited 2008

where *int RMS* = $\int RMS\, \mathrm{d}t$. Both the wear rate and the frictional work increase with respect to the acoustic emission. It is worth noting that there are two

distinct regions for the wear rate. It was found that the difference occurs when the sliding speed increases past 0.18 m/s.

The conclusion that can be drawn from the research into the impact of friction and wear on acoustic processes is that the acoustic emissions increase as the wear rate increases. The acoustic emissions are also impacted by the coefficient of friction as they increase as the coefficient of friction increases. This is different to the generation of airborne noise seen in the previous section.

2.6 Modelling friction and wear

2.6.1 Wear models

There has been extensive research on different wear models. Meng and Yadav provided a comprehensive review on the different wear models in the literature and their origins [98, 99]. It was found that there are no general equations for wear. There are substantial varying parameters with different meanings. This is because wear is dependent on a lot of different factors and not all of them are understood. Barwell [92] described the process of wear formation and the mechanisms of wear in different practical applications. The four examples chosen to illustrate the mechanisms of wear were scuffing, rolling contacts, fretting corrosion, and simple sliding. Their effects on industrial machineries can be seen in engine cylinders, engine bearings, or gears. There are a lot of factors due to the wide variations of material properties and rubbing surfaces that determine how wear will proceed and whether it will lead to machine failure and there are still vast amounts of ongoing research in the industry [93]. Some of the wear model used are described in Table 1.

The main limitation of the wear models previously mentioned is that they are not analytical models, and they are suitable only for a specific set of applications. Fillot et al. [94] devised a general analytical model for a predictive wear equation. This analytical model introduces the third-body concept which places importance on the particles that have been detached during the wear process. The third-body concept includes the flow of those particles inside the contacts in the wear equations. With a third-body concept, the mechanisms of wear

become a lot more different. For example, the third body will support the load, affect the velocity, and prevent the two surfaces from direct contact. This, in turn, acts as a layer of protection reducing the degradation of the surfaces. A diagram showing the third-body concept is shown in Fig. 37

Table 1: Common wear models. Most models are specifically designed for a particular wear type and thus cannot be generalised. The models are split into three categories: Numerical, Empirical, and theoretical.

Model type	Author, year	Wear type	Advantages	Limitations
Numerical model	Shen et al. (2010) [95]	Sliding wear	Input parameters easily calculated through ABAQUS	Based on Archard Wear model and is only empirical. Precision is limited by mesh quality. Computationally expensive with fine meshes
Numerical model	Hassan and Mohammed (2016) [96]	Sliding wear	Artificial Neural Networks provides high accuracy in modelling the sliding wear processes	Artificial Neural Networks requires a lot of data for training and validation purposes. Skewed data or data containing errors can cause the ANN to be trained in the wrong direction causing invalid outputs
Empirical model	Rhee (1970) [97]	Sliding wear	Providing the correct input parameters are used, the correlation is good	Restricted applicability. Furthermore, input parameters are highly dependent on the test conditions and can be hard to establish
Empirical model	Archard and Hirst (1956) [98]	Sliding wear	The experimental results correlate well with this model once the equilibrium position is reached. This model is also simple	Only works in unlubricated conditions
Theoretical model	Archard (1959) [99]	Sliding wear	This model presents a simple approach to determining the flash temperatures at the contact interface during the wear processes	The ideal situations presented in the model may not be accurate depending on the actual test conditions
Theoretical model	da Silva and Pintaude (2008) [100]	Sliding wear	The Archard model was modified by introducing an uncertainty on the wear coefficient. The worn height was treated as a stochastic process which presented better results	This model does not consider the roughness coefficient
Empirical model	Quinn (1971) [101]	Oxidational Wear	This model presents good results for the wear of metals in unlubricated conditions	The model only works for mild wear in unlubricated conditions and only if the appropriate input parameters are used
Numerical model	Öqvist (2001) [102]	Sliding wear	The model is fast and provides accurate results at each time step	The model only works on a macroscopic scale and cannot determine how the wear occurs on the molecular scale
Numerical model	Mukras et al. (2009) [103]	Sliding wear	The parallel implementation of the intermediate cycle-update procedure where the geometry is not updated at every step but at the end of a cycle with a predetermined number of steps drastically reduces computational time while still providing reasonable accuracy	In the absence of parallel computing resources, the intermediate cycle-update procedure loses its advantage. Other implementations such as the step-update procedure (where the geometry is updated after each step) are also computationally expensive
Empirical model	Savio et al. (2009) [104]	Sliding wear	The model shows a satisfactory estimate of the surface roughness evolution during the polishing process	The model has limited applicability. Furthermore, it cannot explain the microscopic interactions occurring during the wear processes

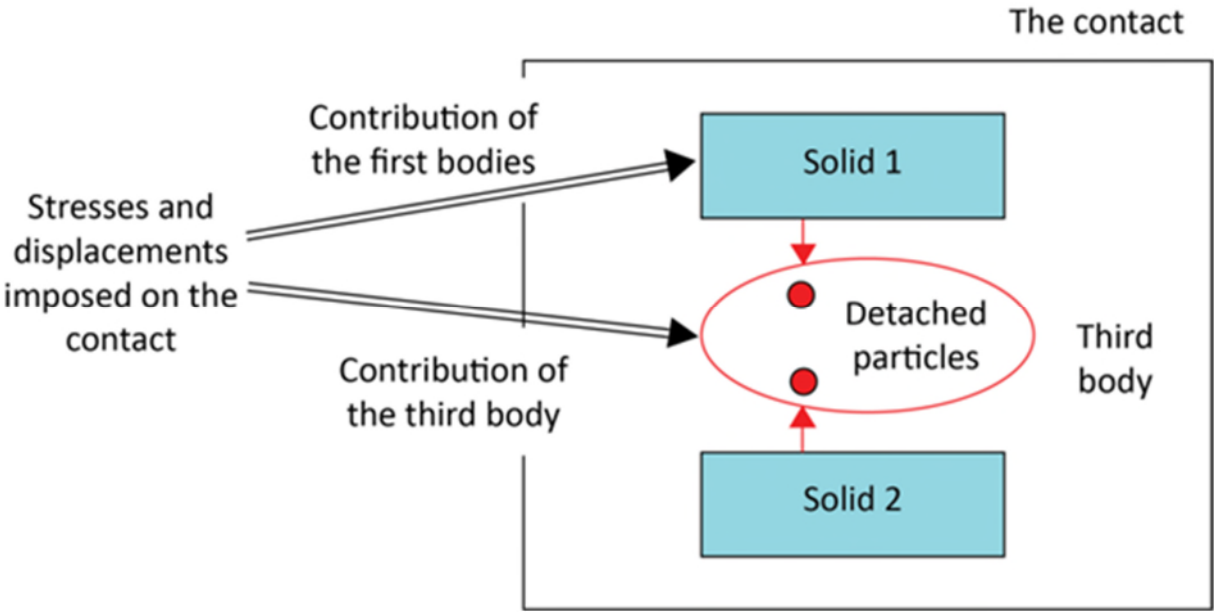

Figure 37: Contribution of the third body to the stresses and displacements imposed to the contact.

2.6.2 Friction Models

Most of the research previously mentioned used the Coulomb's model of friction. However, there are several other existing models. Some of them are extensions and refinements of Coulomb's model. Friction models can be categorized in two distinct categories. There are empirical models (such as Coulomb's model) and physics-based models.

2.6.2.1 Empirical Models

General friction models were developed as alternatives to the Coulomb friction model. This is because the Coulomb model of friction greatly oversimplifies the frictional phenomena. It is widely used in the engineering world, where dynamic effects are not concerned. Furthermore, the Coulomb model of friction is also a common piece of the more advanced models that are available. The main problem with the Coulomb model is that it cannot handle the environment of zero velocity, hence the properties of motion at starting or zero velocity crossing, which are static and rising static friction. More advanced models based on the Coulomb model include the viscous friction model (where the friction force is proportional to the sliding velocity), or the Stribeck model (which

still models the friction force as a function of velocity but includes both the standard Coulomb model and the viscous model). However, it is still valid only for steady-state problems.

To simulate more complex problems, additional features become necessary. Those additional features will then allow to model dynamic behaviors. Unfortunately, the science of tribology is still far from understood [113] and so, most of those models are based on empirical evidence rather than deep scientific knowledge [114]. More complex models can be divided into two categories. The first category includes steady state models, and the second category includes dynamic models. Two common steady-state models are summarized in Table 2.

Table 2: Steady-state models

Model name	Friction phenomena	Limitations
Stribeck model	Coulomb friction Viscous friction Static friction	No presliding and no hysteresis accounted for in this model
Tustin model	Coulomb friction Viscous friction Static friction	Breaks down if the velocity exceeds a certain threshold

Unfortunately, there are a lot of disadvantages with using a static friction model. The main problem is detecting when the velocity is zero. Furthermore, the solutions to the equations of motions are non-unique [105]. Finally, numerical problems occur if static models are used to simulate forward dynamics problems. A dynamic problem is a problem that requires input forces and initial conditions, and accelerations, positions, and velocities are then solved with respect to those input forces and initial conditions [106]. Some common

dynamic models are summarised in Table 3 along with what friction phenomena can be explained by those.

Table 3: Dynamic models

Model name	Seven-parameter	Karnopp (1985) **[107]**	Canuda et al. (1995) **[108]**	Dahl (1968) **[109]**
Pre-sliding displacement	Yes	No	Yes	Yes
Coulomb friction	Yes	Yes	Yes	Yes
Viscous friction	Yes	Yes	Yes	Yes
Negative viscous friction	Yes	No	Yes	Yes
Rising static friction	Yes	Yes	Yes	Yes
Dwell time	Yes	No	Yes	Yes
Frictional memory	Yes	No	Yes	Yes
Limitations	Determining the non-linear parameters can be complex	A lot of phenomena are not considered in the Karnopp model	Discrepancies are observed in certain experimental results	Does not model the Stribeck Effect

2.6.2.2 Physics-based models

All the models previously described are empirical models. That is, they rely on empirical parameters, which can only be fit to the relevant parameters while accommodating the lack of information [110]. Furthermore, as empirical models do not account for the actual physics, the applicability of the model can become uncertain should conditions change. Other branches of friction models include physics-based models. Physics based models use robust scientific knowledge

to formulate the model. This allows for physics-based models to be more accurate at representing the various conditions and more mechanisms can be considered compared to the normal empirical models [111]. However, even though physics-based models can capture all the friction related phenomena, they are in effect much harder to implement as they require an accurate account of all the relevant quantities so missing data or unknown input data errors can create difficulties [112]. Some physics-based models are shown in Table 4:

Table 4: Physics-based models

Model author	Advantages	Limitations
Emami et al. (2017) **[113]**	Provides a good agreement with experimental results while considering the effect of adhesion and shearing in the real contact area along with hysteresis	Only valid for an intermediate range of velocities
Eriten et al. (2011) **[114]**	This model accounts for critical friction phenomena such as stick–slip, modal frequencies and damping, and pre-sliding friction. Furthermore, its physics-based nature gives it good predictive capabilities	The surface roughness parameters need to be extracted along with surface height and asperity distributions. The roughness parameters are also not time-dependant
Dankowicz (1999) **[115]**	The model can predict dynamics which qualitatively agree with other models. This model offers physics-based explanations for the friction processes	The values for the model parameters need to be determined, along with appropriate choices for the internal state variables. Determining those initial values is a complex task
de Moerlooze et al. (2010) **[116]**	This model qualitatively agrees with experimental study and accounts for normal creep, increasing static coefficient of friction with increasing dwell time, pre-sliding hysteresis with non-local memory, Stribeck and viscous effect, frictional lag, stick–slip, and dynamical oscillations	Wear and lubrication are not considered in this model

2.7 Summary

A comprehensive review was provided in this chapter on the different methodologies used to correlate friction and wear with friction noise and seeing how friction and wear would impact the sound pressure levels. This could either be done theoretically or experimentally. From a theoretical point of view, several friction models and wear models were developed separately. However, in all those cases, the acoustic emissions were not included in the purpose. The friction models that were developed as alternatives to Coulomb's model can be divided into two categories. They are either generally empirical models or physics-based models. Empirical models are based on experimental evidence. They rely on defined parameters that are fit to match the conditions for which the model is developed. This allows for an accurate model restricted to the exact purpose it was developed for even if the underlying science is not understood. Physics based models are general models that are created using general physics knowledge and thus can be applied everywhere. It is shown in this review that empirical models are still the model of choice in most friction problems and physics-based models are much less used. This is because they are still poorly understood, and their uses are still debatable. For example, De Moerlooze's model is a dry friction model that agrees with experimental results from a qualitative point of view, however, it still falls short as it does not include asperity wear or lubrication. The EPB model also presents many disadvantages. It is notably more demanding in terms of computational power (although with the increase in available technology, this problem can be diminished). Furthermore, the EPB model is unable to account for micro-displacements. The EPB model does need surface roughness measurements before it can be applied. This means that the surface roughness must be measured, the surface heights data must be processed to describe the asperity-level geometry and the height distribution. Another major problem (that is not exclusive to the EPB model) is that it does not take the evolution of the micromechanics surfaces into question. As the surface roughness changes, the EPB model's predictions will no longer be accurate. This relates to the fact that those models do not include wear. However, no other experimental parameters

are required provided that the material properties (Young's modulus, Poisson's ratio, and yield strength/hardness) are known. The EPB model is also highly dependent on the contact conditions. It is applicable for highly adhesive contacts at asperity scales. However, it is not applicable if the contacts have low adhesion. Empirical models are still the most widely used models to study friction-induced acoustic emissions. Furthermore, models studying noise and wear using lubrication are also not comprehensive. As shown in the previous sections, even current physics-based models suffer from gaps that could be addressed in further research. For example, de Moerlooze's model does not take wear or lubrication into account. On the other hand, Emami's model is not valid for all velocities.

The wear models are similar in that they are all empirical and have been created to suit a particular engineering application. Still, the most widely used wear model to this date is Archard's model due to its relatively simple assumptions. However, the Archard wear model has several shortcomings. For example, it is only valid for rough surfaces (with plastically deformed asperities). It is not valid for polymer surfaces (with elastically deforming asperities. In the case of the study of frictional noise due to wear, Archard's model is the one most widely used. Its assumptions are relatively simple. The wear is proportional to the path of friction, it is also proportional to the friction work force and finally, it is determined by the physical parameters of the process and the mechanical properties of the material. However, such model presents a lot of disadvantages that will impact its accuracy. This is due to a lack of methods to suitably estimate the wear coefficient needed for the model. The different combinations of materials, modes of operations, environments, etc., often leads to a discrepancy between the experimental results and those obtained by the calculations. Other limitations of Archard's wear model are that Archard's law is only applicable for rough surfaces (plastically deformed asperities). It is not applicable for softer surfaces like polymers (which have elastically deforming asperities). It can also be added that Archard's law does not consider material evolution. Materials that initially deform elastically, may start to deform plastically as the contact area and the subsurface hardness changes. More

advanced analytical wear models have also been developed. However, they are mainly focused on the adhesive wear mechanism and do not take friction noise into account. In all those models, the Hertzian contact laws are used, although they are modified to some extent to account for the specific application at hand (such as including the effect of adhesion). Furthermore, all the studies relating wear and frictional noise have been experimental. Numerical studies of wear do not take frictional noise into account. The same can be said with regards to friction models and noise. All studies correlating friction (be it surface roughness or friction coefficient) have been experimental, using Coulomb's law. Alternative and more advanced models, such as physics-based models have not been used regarding friction noise. Numerical studies analysing friction noise do not take wear into account.

2.7.1 Research gap

At the moment, there is no general analytical model that combines friction, wear, and acoustic emissions in a single model, suitable for a wide range of engineering applications as most currently used models are empirical and are thus only suited to the specific application for which they were modelled. A single analytical model including friction noise, friction coefficient, surface roughness, and wear volume during sliding wear could be a significant contribution to the existing literature and could also be adapted for use in a wide range of industrial applications as such a model would not be empirical by nature, and thus would not be confined to certain specific situations. Most models investigating airborne noise are also numerical and there are no airborne noise models that include the wear. This is the research gap that this general analytical model attempts to fill.

3 Research Approach

The research approach is shown in figure 38.

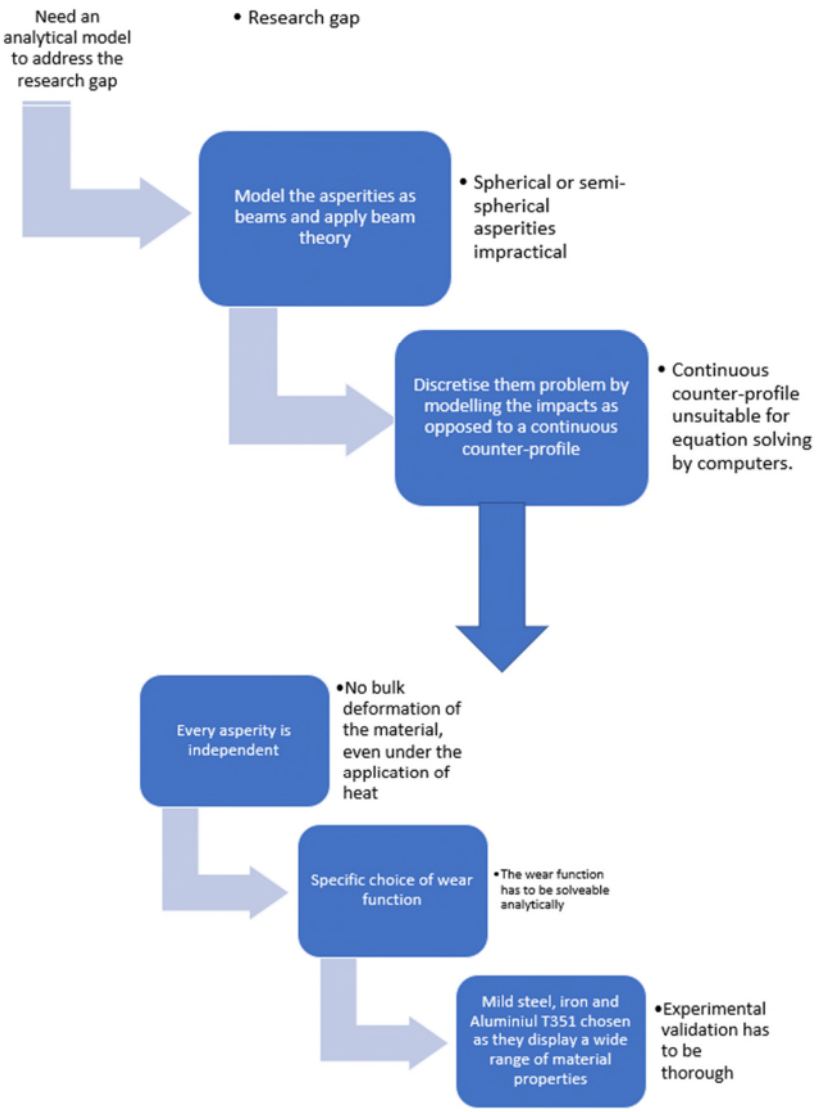

Figure 38: Flowchart of the method approach

There are two main components for the research. The first component involves the creation of the analytical model, and the second component involves the experimental validation of the analytical model.

3.1 Research Gap

In order to address the research gap, it was necessary to create an analytical model that would be able to encompass both the wear and the generated sound pressure at the asperitical level. The model would be able to predict the wear and the sound pressure generated under different operating conditions for sliding wear.

3.1.1 Model the asperities as beams and apply beam theory

The first consideration to take into account was the shape of the asperities. Modelling them as semi-spherical or spherical asperities will prove problematic too if impacts have to be calculated on the asperities. Therefore, it was opted to approach the problem using beam model theory. Beam theory can account for beam vibrations, bending, displacement and breaking. Modelling the asperities as beams thus provided to be the more suitable approach in defining asperitical shapes.

3.1.2 Discretise the problem by modelling the impacts as opposed to a continuous counter-profile

Most advanced friction models use a continuous counter-profile. However, the analytical model would need to be calculated using a software package capable of discretising the problem. As such, a continuous sliding is not a suitable method of calculation for the intended aim. Instead, it is possible to discretise the problem by approximating the continuous sliding as a series of impacts per unit time. Discretising the problem allows a software package to calculate the stresses on a per-cycle basis.

3.1.3 Every asperity is independent

Wear occurs during the sliding process and alters the initial height distribution. For simplicity, it was assumed that wear would only affect the height of the asperities. As there was a need to discretise the problem into distinct unit times, this led to the further simplification that every impact would ultimately be self-contained. This means that asperities would behave independently of one another. The corollary of that assumption is that there would be no bulk

deformation of the material. This means that macroscopic material properties could be used.

3.1.4 Specific choice of wear function

The choice of the wear function is very important. This is because it has to be versatile enough that the scope of applicability remains high, but the function needs to be analytically solvable. It was therefore developed by using the deformation and the breaking of prismatic cantilever beams as a basis for the wear formulation. The height distribution of the asperities varies according to the wear function. This allowed the creation of a differential equation that describes the relationship between the wear function and the asperitical height distributions.

3.2 Mild steel, iron and aluminium T351 chosen as they display a wide range of material properties

The experimental validation of the model was designed in such a way as to assess the accuracy of the analytical model. Despite the increased error at higher temperatures due to the deformation of the material, it was felt that higher temperatures would still be a part of the experimental scheme. The materials were chosen based on the availability of the samples and also based on their material properties. Heat-treated aluminium, for example has a high elastic zone. Iron, on the other hand, has a large plastic zone, whereas mild steel has a high amount of wear. Those varying material properties allowed to assess different parts of the analytical model.

4 Analytical Modelling

4.1 Introduction

The aim of the analytical model is to provide a quantification of the wear and the noise emitted due to the friction processes on a pin-on-disc setup. The analytical model differs from previously published empirical models in that it uses physics-based mechanics in order to quantify the wear and noise interdependencies. It also differs from previously published analytical models as those models either measure the friction processes, the wear, or the sound separately but do not provide an interdependency between them. However, friction processes are hard to model analytically and so compromises had to be made in order to lower the computational cost of the model and its complexity. Those compromises are detailed in Section 4.2. The derivation of the model was comprised of three parts. The first part of the model determines the original asperity height distribution as well as the changes in the asperity heights as wear starts to happen. The second part of the model determines the stresses on each individual asperity. This is because the stresses determines whether or not the asperities undergo wear as this depends on the material properties of the asperities. Finally, the third part of the model calculates the sound pressure emitted by the asperities that have undergone the stresses of impacts. The sound pressure and the total wear is then plotted. Section 4.3 details the analytical model. The program for the model was written in MATLAB. The code is explained in section 4.4. Finally, the analytical results given by MATLAB are discussed in section 4.5

4.2 Theory and Assumptions

The aim of the analytical model is to quantify the interdependence of sliding wear and the emitted airborne noise in a pin-on-disc setup. There are various considerations that had to be taken into account when creating such a model.

4.2.1 Assumption 1: Consideration of asperitical shapes

The model acts on an asperitical level, and as such, the first consideration regarded the shape of the asperities. The most common shape used to

examine asperitical contacts are Hertzian contacts. The asperities are modelled as spheres or semi-spheres [117]. However, this presented several concerns in the present model. Friction models using spherical contacts do not model the wear analytically. This is because developing an analytical model that calculates the energy released during impacts between spherical asperities as well as calculating the impact force and vibrational displacement in spherical or semi-spherical objects would be computationally expensive.

In order to keep the model simple enough to be able to calculate forces and displacements on a large number of asperities in a short amount of time, it was decided to model the asperities as prismatic beams. This is because beam theory is well understood and vibrational displacements of beams as well as impacts and forces of beams can be readily calculated using bending theory. The beam approach does have an impact on the accuracy of the model, as it is shown that asperities are closer to spheres than they are to prismatic beams. However, the compromise was considered acceptable. This is because other research concerned with energy emitted by asperities during friction processes also use the beam approach [118]. When two beams are in contact with one another under static conditions, deformation will occur. The deformation can be either elastic or plastic depending on the initial external force applied on the beams. This is shown in figure 39.

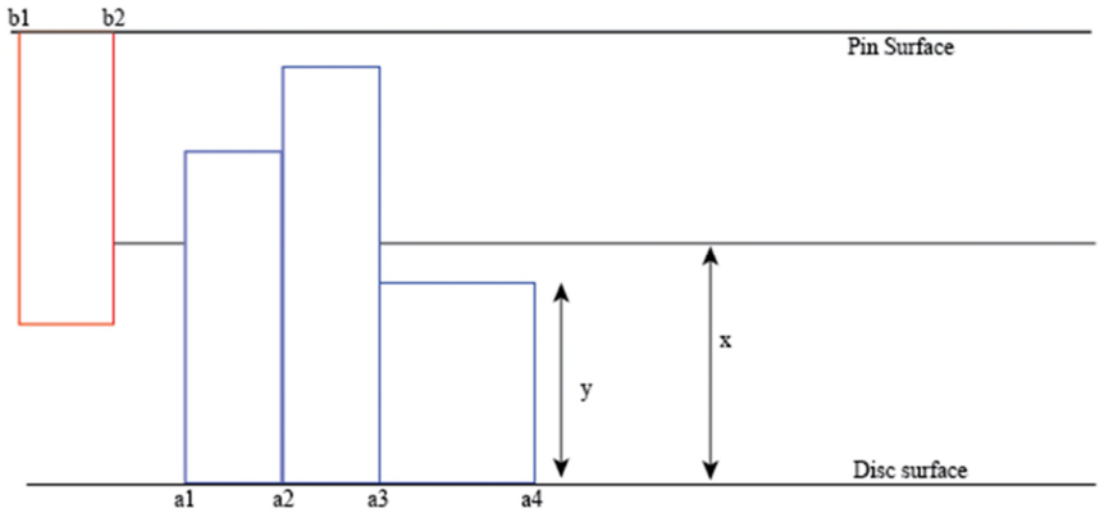

Figure 39: Conditions of contacts

a1, a2, a3, a4 lie on a plane on the bottom surface (surface of the disc), b1, b2, lie on a plane on the top surface (tip of the pin), y is the height of an asperity and x is the distance from either surface to the centreline axis (located at a mid-distance between the two surfaces). When the asperities are in contact, three conditions can occur. The two asperities can be either elastically deformed, plastically deformed, or just in contact.

Condition 1: If the average length of two contacting asperities equals the distance to the centreline, then the two asperities are just in contact.

$$\frac{y_{a_n} + y_{b_n}}{2} = x \quad \textbf{(4-1)}$$

Condition 2: If it is greater than the centreline, then the asperities are deformed. If the deformation caused by the stress is less than the elastic limit, then elastic deformation occurs.

$$\frac{y_{a_n} + y_{b_n}}{2} > x \quad \textbf{(4-2)}$$

Condition 3: If the stress caused by the deformation is greater than the elastic limit, then plastic deformation occurs

$$\frac{y_{a_n} + y_{b_n}}{2} \gg x \quad \textbf{(4-3)}$$

4.2.2 Assumption 2: Asperities are independent of one another

Whether the deformation is plastic or elastic depends on the material properties such as the elastic modulus and the yield strength. It is also assumed that all the asperities are independent of one another. This means that what happens to the previous asperity does not influence the next asperity. This assumption was made even though when an asperity on the disc is struck, it can set off a number of collisions between neighbouring asperities. However, the complexity of the model drastically increases when that happens. Neighbouring asperities may start vibrating too, which can set off even further collisions. Vibrations could be constructive leading to an increase in sound, or they may vibrate in the opposite direction thus cancelling each other out, leading to a decrease in

sound. The high number of uncertainties in such situations led to the simplification that the distance between each asperity on the disc was sufficient that interactions would not occur. Furthermore, it is assumed that the pin asperity does not wear out. This is because, during the experimental validation, the pin was replaced after each experiment and wear was not observed.

4.2.3 Assumption 3: Macroscopic material properties are assumed to hold.

During the sliding process, further assumptions are made in order to keep the computational cost down. The asperities are assumed to behave as macro-sale prismatic cantilever beam following beam theory. This is an acceptable assumption as the asperities are on a mesoscopic scale and so bulk material properties are a reasonable approximation. Furthermore, the use of a large enough scale allows bypassing the effect of humidity. The model is only valid for dry contacts. However, at small enough scales, the effect of humidity can no longer be ignored as the condensation of the ambient humidity causes water droplets to form in the cracks of the contact surfaces. Finally, the sound is assumed to be generated by two main mechanisms detailed below:

Mechanism -1: If the asperities undergo elastic deformation, then the sound is emitted due to the elastic vibration of the asperities [119]. However, some further assumptions are made for elastic vibrations. For this kind of vibrations, there can be several dynamic instabilities contributing to the radiation of sound. For instance, mode-coupling instability can lead to acoustic propagation. Furthermore, a beam will vibrate in all modes. However, it is found that the first mode of vibration will have the largest impact in the displacement and in the sound generation. The other modes end up having negligible contribution to the sound generation. As such, only the first mode is considered for the vibration of the beams.

Mechanism-2: If the asperities break under the force of the impact [120], then the mechanism for the generation of sound is different. This is due to the differences in asperity lengths. In mechanism 1, the asperity length is higher, and this induces a lower flexural stiffness. Similarly, for mechanism 2, the

flexural stiffness is higher. As such, the sound frequencies are different and so is the sound pressure.

4.2.4 Assumption 4: No elasto-plastic deformation

We assume that if the asperities undergo plastic deformation, then no sound is emitted. This is because all the energy is used in the deformation. We also assume that asperities that undergo plastic deformation do not go back to the elastic zone anymore. It is possible for asperities that undergo plastic deformation to still display some elastic behaviour in the next cycle. However, that elastic behaviour is smaller than in the previous cycles and so their contribution to the noise is more limited in subsequent cycles and so it was decided to neglect them. Furthermore, elasto-plastic behaviour was neglected to reduce the complexity of the model. This is because elasto-plasticity would provide negligible contribution to either the noise or the wear compared to a fully elastic asperity (which provides the contribution to the noise due to the vibration) and the plastic deformation (which ultimately leads to the wear). Asperities that are in elasto-plastic deformation do not remain in that state for long due to the speed of the cycles. They would quickly enter the plastic stage and eventually break. As there are no compression waves generated during plastic deformation, the asperities do not vibrate. To account for those mechanisms, the model is divided into three components. First, the model generates a distribution of heights for the asperities on the surface of the disk. Then, for every asperity that is elastically vibrating, the model calculates the vibrational displacement and velocity of the asperity. Finally, for every asperity that wears out, the model calculates the force of impact and the sound emitted as the asperity breaks and replaces the asperity with a new asperity based on the wear function.

4.2.5 Assumption 5: Only one asperity modelled on the pin

To prevent the model from being computationally prohibitive, only one asperity on the pin is modelled. This is because it is assumed that the pin would have negligible wear. For that to hold true, the pin is replaced between each experiment. The distribution of heights on the disc asperities is assumed to be

exponential as this gives a good approximation to the actual distribution of asperities [22]. As the pin strikes each asperity during the rotation of the disc, the stresses are calculated for each impact. This determines whether the asperities are elastically vibrating, plastically deformed, or broken. This is used to determine which mechanism of sound is used to calculate the sound generated by the struck asperity. Furthermore, as wear occurs on the disc, the asperitical map changes and is replaced after each rotation by a new asperitical map. To this effect, a wear function is also developed to calculate the changes in the asperitical map.

4.2.6 Assumption 6: No continuous counter-profile

It should be noted that other friction models use a counter-profile that the pin asperity would slide over However, modelling asperities as a continuous counter-profile would involve high computational costs. Therefore, the interactions are made in the form of impacts as it provides a reasonable starting postulate for the model while keeping the computational cost acceptable.

4.3 Model Derivation

4.3.1 Deriving the wear function

As the pin is assumed not to wear out, the wear model does not have to be applied on the pin, but only on the disc. The impacts between the top asperity and the bottom asperities are represented as point impacts. Wear occurs when the impact between the asperities lead to a deformation such that the total stress on the asperity exceeds the Ultimate Tensile Strength which leads to the asperities breaking off. As such, wear can be taken as a function of deformation only W(y-x). This means that an asperity at a height of y at a time t, will be at a height of $dy = y - \Delta y$ at time $t+\Delta t$ under wear as shown in figure 40.

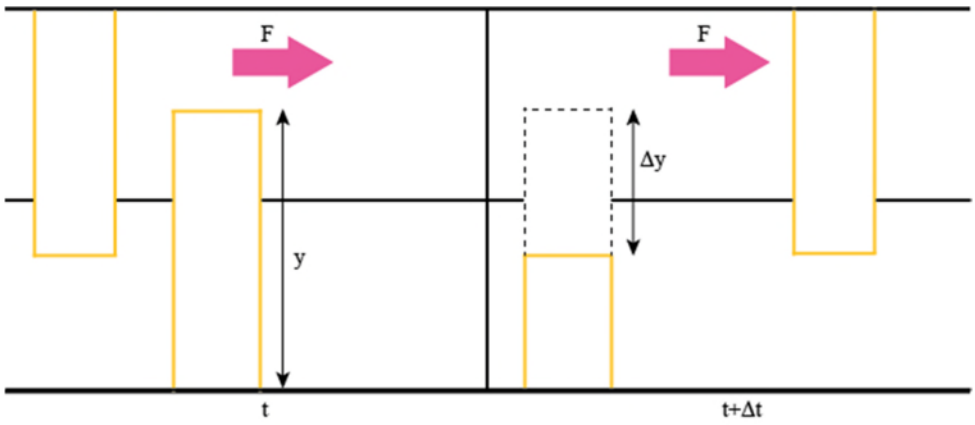

Figure 40: Height changes of an asperity under wear

An asperity at a height of y at time t will be at a height of y-Δy (Δy is the loss of asperitical height) at a time t+Δt (Δt is the time it takes for the asperity to break). This can be summarised in the following four equations:

$$\frac{\Delta y}{\Delta t} = W(y - x) \tag{4-4}$$

$$\Delta y = W(y - x)\Delta t \tag{4-5}$$

$$dy = y - \Delta y \tag{4-6}$$

$$dy = y - W(y - x)\Delta t \tag{4-7}$$

Differentiating with respect to y to get the rate of change of the wear gives:

$$\frac{d'y}{dy} = 1 - W'(y - x)\Delta t \tag{4-8}$$

$$d'y = dy(1 - W'(y - x)\Delta t) \tag{4-9}$$

The height distributions of the asperities can be given as Φ (y, t) at any time t. At any time, t + Δt, the asperities will have a height of dy. This is given by the new distribution Φ (y-Δy, t+Δt) where Δt is the time step. In the case of the pin-on-disc setup, the time step is the time between each consecutive contact on the same asperity (which is the time for one revolution). Multiplying the original roughness distribution by the wear function gives the new distribution function as shown in equation (4-10):

$$W(y-x) * \Phi(y,t) = \Phi(y-\Delta y, t+\Delta t) \quad \textbf{(4-10)}$$

By corollary, this means that dividing the new distribution function by the wear function returns the original distribution function as shown in equation (4-11):

$$\Phi(y,t) = \Phi(y-\Delta y, t+\Delta t) * \frac{1}{W(y-x)} \quad \textbf{(4-11)}$$

The changes in the height of each asperity are also linked to the wear function so that equation (4-12) holds.

$$d'y = dy * W(y-x) \quad \textbf{(4-12)}$$

This equation can be rearranged as follows:

$$\frac{1}{W(y-x)} = \frac{dy}{d'y} \quad \textbf{(4-13)}$$

The relationship between the original distribution function and the subsequent distribution function can therefore be expressed as follows by combining equation (4.11) and (4.13):

$$\Phi(y,t) = \Phi(y-\Delta y, t+\Delta t)\frac{dy}{d'y} \quad \textbf{(4-14)}$$

Rearranging gives:

$$d'y\Phi(y,t) = \Phi(y-\Delta y, t+\Delta t)dy \quad \textbf{(4-15)}$$

With the relationship established, a partial differentiation equation can be formed to relate the asperity height to the wear of the material. This is done by taking the Taylor expansion of the function.

$$dy(1-W'(y-x)\Delta t)\Phi(y,t) \quad \textbf{(4-16)}$$
$$= dy\Phi(y,t) - dy\Delta y\frac{\partial}{\partial y}\Phi(y,t) + dy\Delta t\frac{\partial}{\partial t}\Phi(y,t)$$

This is a first-order Taylor expansion. This equation can be rearranged and then simplified by expanding the left-hand side, dividing by dyΔt, and subtracting Φ(y,t). Applying the reverse chain rule gives:

$$\frac{\partial}{\partial t}\Phi(y,t) = -(W(y-x)\Phi'(y,t) + W'(y-x)\Phi(y,t) \quad \textbf{(4-17)}$$

$$\frac{\partial}{\partial t}\Phi(y,t) = -\frac{\partial}{\partial y}(W(y-x)\Phi(y,t)) \quad \textbf{(4-18)}$$

To solve the partial differentiation equation, a substitution u is used, where u = log(Φ(y,t)).

$$\frac{\partial u}{\partial t} = \frac{\Phi'(y,t)}{\Phi(y,t)} \quad \textbf{(4-19)}$$

$$\frac{\partial u}{\partial t}\Phi(y,t) = -W(z)\frac{\partial u}{\partial y}\Phi(y,t) - W'(z)\Phi(y,t) \quad \textbf{(4-20)}$$

$\frac{\partial u}{\partial t} + W(z)\frac{\partial u}{\partial y} = -W'(z)$ when $z = y - x$

$$dt = \frac{dy}{W(z)} = -\frac{du}{W'(z)} \quad \textbf{(4-21)}$$

Changing variable gives $dz = dy$ so dt $= \frac{dz}{W(z)}$ and since $du = -W'(z)dt$, then $du = -\frac{W\prime(z)}{W(z)}dz$

The general solution can be expressed as:

$f(u,y,t) = c_1$ and $g(u,y,t) = c_2$

$f = \varphi(z) - t = c_1$, where $\varphi(z) = \int_0^z \frac{1}{W(z)}dz$

$$g = u + log[W(z)] = c_2 \quad \textbf{(4-22)}$$

At $t = 0$, let $G(y) = log[\Phi(y,0)]$

$$u - G(y) = 0 \quad \textbf{(4-23)}$$

If we use the inverse function to express the deformation as a function, then:

Let $\theta(\varphi(z)) = z$

$$y = x + \theta(f) \quad \textbf{(4-24)}$$

The final solution is therefore:

$$u = -log[W(z)] + log[W\{\theta(\varphi(z) - t)\}] + G[x + \theta(\varphi(z) - t)] \quad \textbf{(4-25)}$$

A relationship between asperitical height and wear is found:

$$\Phi(y,t) = \frac{W[\theta\{\varphi(z) - t\}]}{W(z)} exp\ (G[x + \theta(\varphi(z) - t)]) \quad \textbf{(4-26)}$$

Each quantity is defined as follows:

Φ is the asperitical height distribution function

W is the wear function

$$\varphi = \int \frac{1}{W(z)} dz$$

θ is the inverse function such that θ(φ(z)) = z

G = log(Φ(y,0)) (The logarithm of the original distribution function).

4.3.2 Calculating the stresses on each asperity due to the impacts of the pin

Treating the asperities as cantilever beams allows us to use beam theory to calculate the stresses as the pin impacts each asperity. The impact force can be calculated thusly:

$$Ft = mv \quad \textbf{(4-27)}$$

F is the impact force, t is the contact time, m is the mass of the asperity and v is the velocity of the disc. The contact time can be determined by the total number of asperities. If the pin asperity contacts all opposing asperities for the same length of time, the contact time can be determined using equation (4-28):

$$t = \frac{T}{N} \quad \textbf{(4-28)}$$

Where T is the total time taken for one rotation and N is the total number of asperities. The mass of an asperity can be calculated using equation (4-29):

$$m = pV \tag{4-29}$$

Where p is the density of the material and V is calculated as follows:

$$V = cH \tag{4-30}$$

Where c is the cross-sectional area of the asperity and H is the height.

The total number of asperities present on the disc depends on the width of each asperity. Assuming an exponential distribution of width, similarly to the height distribution gives us the necessary information. The sum of the widths of the asperities (until the total distance travelled by the pin in one rotation is reached) gives the number of asperities. The force of impact on each asperity can then be calculated. From this, the maximum bending moment can also be calculated. The point of impact on the asperity must also be calculated. It is done by calculating the horizontal and vertical distance travelled by the pin asperity.

The asperity on the pin is under positive load, it will move down at a constant acceleration as it carves the wear track on the disc as shown in figure 41. The disk asperities also travel at a constant horizontal velocity. The linear velocity of the disk can be calculated. Knowing the velocity of the disk and the width distribution of the asperities, the time between contacts (hence the time the pin must travel down before reaching the next asperity) can be calculated as follows:

$$TBC = \frac{s}{v} \tag{4-31}$$

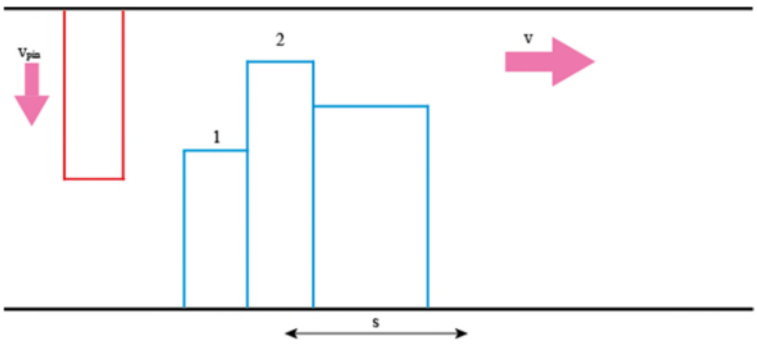

Figure 41: V is the relative velocity of the pin. s is the width of an asperity. TBC is the time taken for the pin to go from position to position 2.

Where TBC is the time between contacts, and s is the width of the asperity. As for the pin, its downwards velocity as it reaches the next asperity can be calculated as follows:

$$v_{pin} = u + g * TBC \quad \textbf{(4-32)}$$

Where v_{pin} is the initial velocity of the pin at the next point of contact, u is the initial velocity at the previous point of contact, g is the acceleration and TBC is the time between contacts. With the velocity calculated, the downwards displacement of the pin can be calculated. This determines if the pin has enough time to meet the next asperity and if so, at what point:

$$s_{pin} = ut + \frac{1}{2} g * TBC^2 \quad \textbf{(4-33)}$$

If the height difference between two successive asperities is less than the distance travelled by the pin, then contact is made, and the distance is equal to $H - s_{pin}$.

And thus, the maximum stress equals:

$$\theta = \frac{M}{S} \quad \textbf{(4-34)}$$

Where S is the section modulus which depends on the cross-section of the asperity.

The maximum stress can then be compared to the maximum tensile strength of the material. For each asperity, if the stress exceeds the strength of the material, the asperity breaks, and wear occurs. If it does not but exceeds the yield strength, then the material is plastically deformed. If neither of those conditions are achieved, then the asperity is elastically vibrating.

4.3.3 Sound produced due to elastically vibrating asperities

To calculate the sound produced due to an elastically vibrating asperity, its displacement is first calculated using equation (4-35):

$$D(x,t) = X(x) * \ [A\ cos(\omega t) + B\ \ sin(\omega t)] \quad \textbf{(4-35)}$$

Where ω is the angular frequency. The displacement is both time-dependant and position-dependant. According to Volterra's dynamics of vibration [121], X(x) is given by:

$$D(x) = \frac{1}{2}\left\{[cos(\lambda x) - cosh(\lambda x)] + \left[\frac{-cos(\lambda L) - cosh(\lambda L)}{sin(\lambda L) - sinh(\lambda L)}\right][sin(\lambda x) - sinh(\lambda x)]\right\} \quad \textbf{(4-36)}$$

The constants A and B must be found. A depends on the initial position at time t = 0. B depends on the initial velocity. B = 0 because the asperity is not vibrating at time t = 0. At X = L, X(L) = 1. A is given in equation (4-37):

$$A = \frac{2}{L}\int_0^L D(x, t = 0)X(x)\ dx \quad \textbf{(4-37)}$$

By solving this equation, A is found to be given by equation (4-38):

$$A = \left[\frac{-4WL}{EI\rho A\lambda^4(\lambda L)e^{\lambda L} + e^{2\lambda L} - 1)}\right] * \left[3\,sin(\lambda L)\left(e^{2\lambda L} + 1\right) - 2(\lambda L)^3 e^{\lambda L} + cos(\lambda L)\left(3 - (\lambda L)^3\left(e^{2\lambda L} + 1\right) - 3e^{2\lambda L}\right)\right] \quad \textbf{(4-38)}$$

Where λ is a coefficient given by equation (4-39):

$$\lambda = \left(\frac{\rho A}{EI}\omega^2\right)^{1/4} \quad \textbf{(4-39)}$$

The displacement in this case corresponds to the deflection of the beam. E is the elastic modulus, and I is the moment of inertia.

If the system is underdamped (as it would be), then the damping ratio can be calculated.

First, the critical damping is determined by:

$$c_c = 2m\omega \quad \textbf{(4-40)}$$

The damping coefficient can be calculated as follows:

$$C = 4bL\sqrt{\frac{2m}{\pi k_b T}P} \quad \textbf{(4-41)}$$

Where b is the beam width, k_b is the Boltzmann constant, T is the ambient temperature and P is the ambient pressure.

The damping ratio is then calculated as follows:

$$\xi = \frac{C}{c_c} \quad \textbf{(4-42)}$$

The damped displacement can be calculated as follows:

$$X = De^{-\xi\omega t}cos\,(\omega t) \quad \textbf{(4-43)}$$

Where t is the time of the next impact (which is the time of one rotation)

On subsequent cycles, asperities that were already struck in the preceding cycle would still be vibrating due to the impact. An equivalent impact force can be calculated using deflection equations [122]. The equivalent impact force is the force that the vibration of the asperity is inducing, as shown in figure 42:

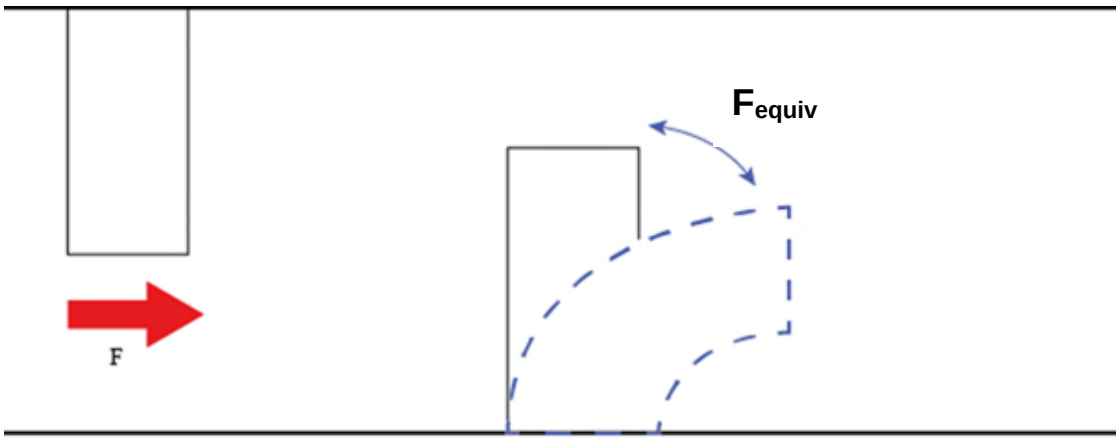

Figure 42: F is the impact force caused by the top asperity. F_{equiv} is the force generated by the vibration of the bottom asperity due to the previous impact

The equivalent impact force can then be calculated by:

$$F_{equiv} = \frac{6XEI}{a^2(3L - a)} \quad \textbf{(4-44)}$$

The moment and stress can thus be calculated as before by adding the equivalent impact force and the true impact force together as shown in equation (4-45). This is because the total force would be the sum of the force induced by the vibrating asperity as it was struck in the previous cycle and the force of impact caused by the next impact of the pin on the already vibrating asperity in the next cycle.

$$F_{Total} = F + F_{equiv} \quad \textbf{(4-45)}$$

The vibrational velocity of an elastically vibrating asperity can be calculated as follows:

$$V = -\xi\omega t D e^{-\xi\omega t} cos(\omega t) - D e^{-\xi\omega t} sin(\omega t) \quad \textbf{(4-46)}$$

The acoustic power can then be calculated using equation (4-47):

$$P = \rho_0 c S \sigma V^2 \quad \textbf{(4-47)}$$

where ρ_0 is the air density, c is the speed of sound in air, S is the cross-sectional surface area, σ is the radiation efficiency, and V is the vibrational velocity [123]. The sound power level is given by equation (4-48):

$$L_w = 10\ log_{10}\left(\frac{P}{P_r}\right) \quad \textbf{(4-48)}$$

Where P_r is the reference power (= 10^{-12} W). The sound pressure level is given by equation (4-49):

$$L_{p1} = L_w + 10\ log_{10}\left(\frac{Q}{4\pi r^2}\right) \quad \textbf{(4-49)}$$

Where Q is the directivity factor. It could be either 1 (full sphere propagation), 2 (half sphere propagation), 4 (quarter sphere propagation) or 8 (eighth sphere propagation). The sound pressure can then be calculated using equation (4-50):

$$P = P_0 * 10^{\frac{1}{20}L_{p1}} \quad \textbf{(4-50)}$$

Where P_0 is the reference pressure ($20*10^{-6}$ Pa).

4.3.4 Sound produced due to breaking asperities

If the asperities are broken, the kinetic energy caused by the impact between the two asperities is converted to sound and heat energy (as shown in figure 43):

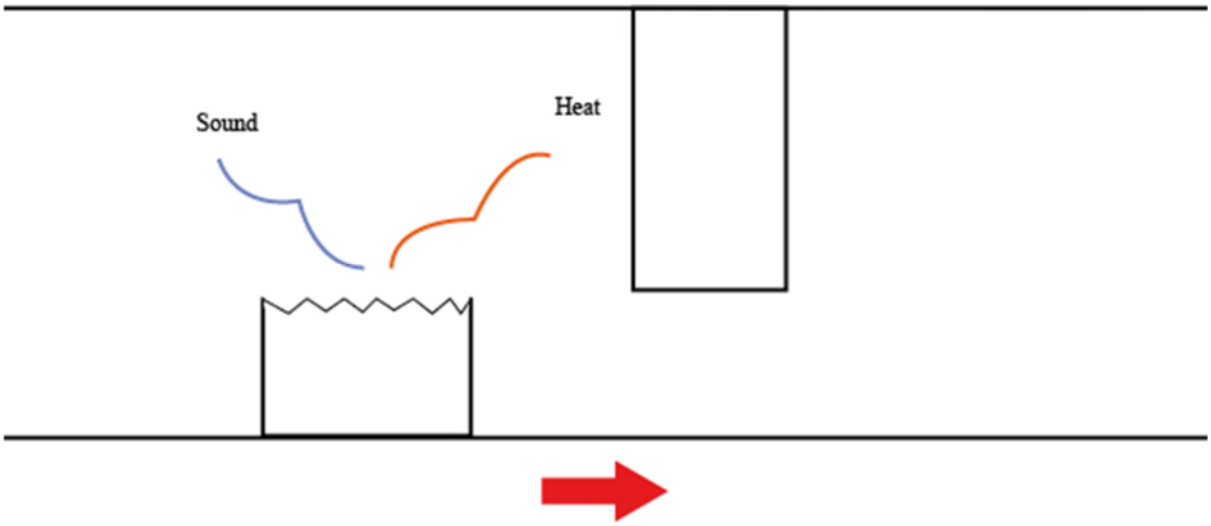

Figure 43: Sound and heat is released as the asperity breaks

The energy can be calculated using equation (4-51) [124]:

$$\gamma = H\pi r^3 \beta \quad \textbf{(4-51)}$$

Where H = hardness, and β = 0.5 (if half of the energy is converted into sound and the rest is converted into heat). The sound power is related to the energy as given by equation (4-52):

$$P = Ac\gamma \quad \textbf{(4-52)}$$

Where A is the cross-sectional area of the asperity and c is the speed of sound in air. The sound power level, the sound pressure level and the sound pressure can be calculated using the previous equations. The total pressure level (combining the elastic vibration of one asperity and the breaking of one asperity) can be calculated using equation (4-53):

$$L_{total} = 10\,log_{10}\left(\frac{{L_{p1}}^2 + {L_{p2}}^2}{{L_0}^2}\right) \quad \textbf{(4-53)}$$

Where L_0 is the reference pressure level (= $2*10^{-5}$ Pa) and L_{p2} is the pressure level caused by breaking of one asperity.

In the case of breaking asperities, once the asperity has broken off (assuming it breaks off at its base), a new asperity is generated at its place, creating a new asperitical map, the new asperitical map must be determined using equation (4-26). However, the wear function must be calculated. Under the assumption that the asperity behaves as a cantilever beam allows us to calculate the stress and the deflection of the asperity when acted on by a point force. This is shown in figure 44:

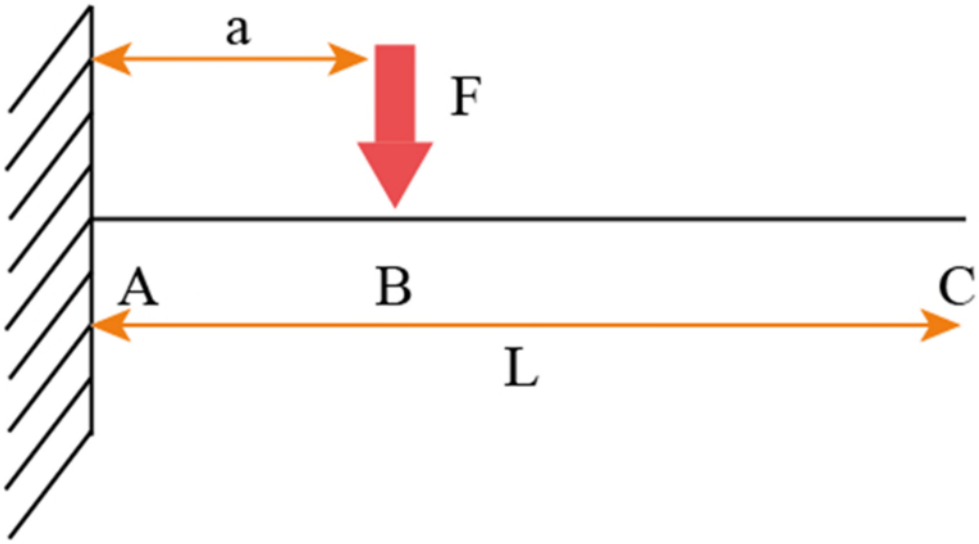

Figure 44: Forces acting on a cantilever beam

The total critical deflection at C is the sum of the deflections from A to B and the deflection from B to C. The critical deflection from A to B is given as follows:

$$z = \frac{Fa^3}{3EI} \quad \textbf{(4-54)}$$

This can be rewritten as:

$$z = \frac{\theta S a^2}{3EI} \quad \textbf{(4-55)}$$

From there, we can establish a function a(z):

$$a(z) = \left(\frac{3EI}{\theta S}\right)^{1/2} z^{1/2} \quad \textbf{(4-56)}$$

The critical deflection from B to C is given as follows:

$$z = \frac{3Fa^3b}{6EIa} \quad \textbf{(4-57)}$$

Similarly, a function b(z) can be established:

$$b(z) = \frac{2EI}{\theta S a(z)} z \quad \textbf{(4-58)}$$

Substituting for a(z), we get:

$$b(z) = \frac{2EI}{\theta S \left(\frac{3EI}{\theta S}\right)^{1/2}} z^{1/2} \quad \textbf{(4-59)}$$

Since we are assuming that the asperity breaks off at its base, then W(z) = a(z) + b(z), so:

$$W(z) = Az^{1/2} + Bz^{1/2} \quad \textbf{(4-60)}$$

Where:

$$A = \left(\frac{3EI}{\theta S}\right)^{1/2} \quad \textbf{(4-61)}$$

$$B = \frac{2EI}{\theta S \left(\frac{3EI}{\theta S}\right)^{1/2}} \quad \textbf{(4-62)}$$

It can be rewritten as:

$$W(z) = Cz^{1/2} \quad \textbf{(4-63)}$$

Where C = A+B.

Using this wear function and substituting it in the partial differential equation allows us to generate a new asperitical map when the previous one is broken

off. This is repeated after each cycle to calculate the total sound and wear. It should be noted that the effect of wear debris has been neglected during the generation of the new asperitical map. The effect of wear debris would be hard to incorporate analytically since their effect on friction noise can be either positive or negative and reports on this matter are conflicting. However, due to the speed at which the disc spun, the wear debris were mostly propelled away from the wear track and the wear tracks looked mostly free of debris. As such, it was felt reasonable that the wear debris would not be incorporated into the new asperitical map.

4.3.5 Statement of academic contribution

This model presents four important contributions. Section 4.3.1 provides a detailed methodology to model the change of the asperity heights as wear progresses during a sliding friction process. Section 4.3.2 provides a suitable wear function that can be analytically solved and thus, suitable to be used in conjunction with the formulation presented in section 4.3.1. Finally, sections 4.3.3 and 4.3.4 present different ways of obtaining the quantification for the sound pressure depending on which mechanism is involved during the friction process. Combined together, this analytical model is able to quantify both the wear and the sound pressure as the friction process goes on. This can be used in a predictive manner. For example, given the sound pressure data, it is possible to derive the wear as the model shows the interdependency between the two.

4.4 MATLAB program

The MATLAB program was developed following the analytical model. At the beginning of the program, all variable parameters are pre-initialised. This includes the material properties, the height distribution of the asperities, the impact forces, the vibrational displacements, the velocity, etc. The pre-initialisation of the variables allows the program to create arrays of specific sizes. This is purely done to save computational time.

The program also generates the initial asperity height distribution. In the analytical model, the original height distribution is generic. There are generally two distributions that can be considered. Those are detailed in the following section.

4.4.1 Choosing an initial distribution function

To model the initial asperitical height distribution, a statistical contact method is chosen. It is assumed that the asperities follow a probabilistic distribution function. There are two important distribution functions that could be used: the exponential distribution function and the Gaussian distribution function.

4.4.1.1 Exponential Distribution function

A simple exponential distribution function is a “fair approximation to the uppermost 25 percent of the asperities of most surfaces” according to Greenwood. The exponential distribution function is given by equation (4-64):

$$\Phi(z^*) = e^{-z^*} \quad \textbf{(4-64)}$$

Where z* = z/σ. Z = the height of asperities measured from the mean of asperity heights, σ = standard deviation of asperity heights and Φ = distribution function of asperity heights. This is illustrated in figure 45:

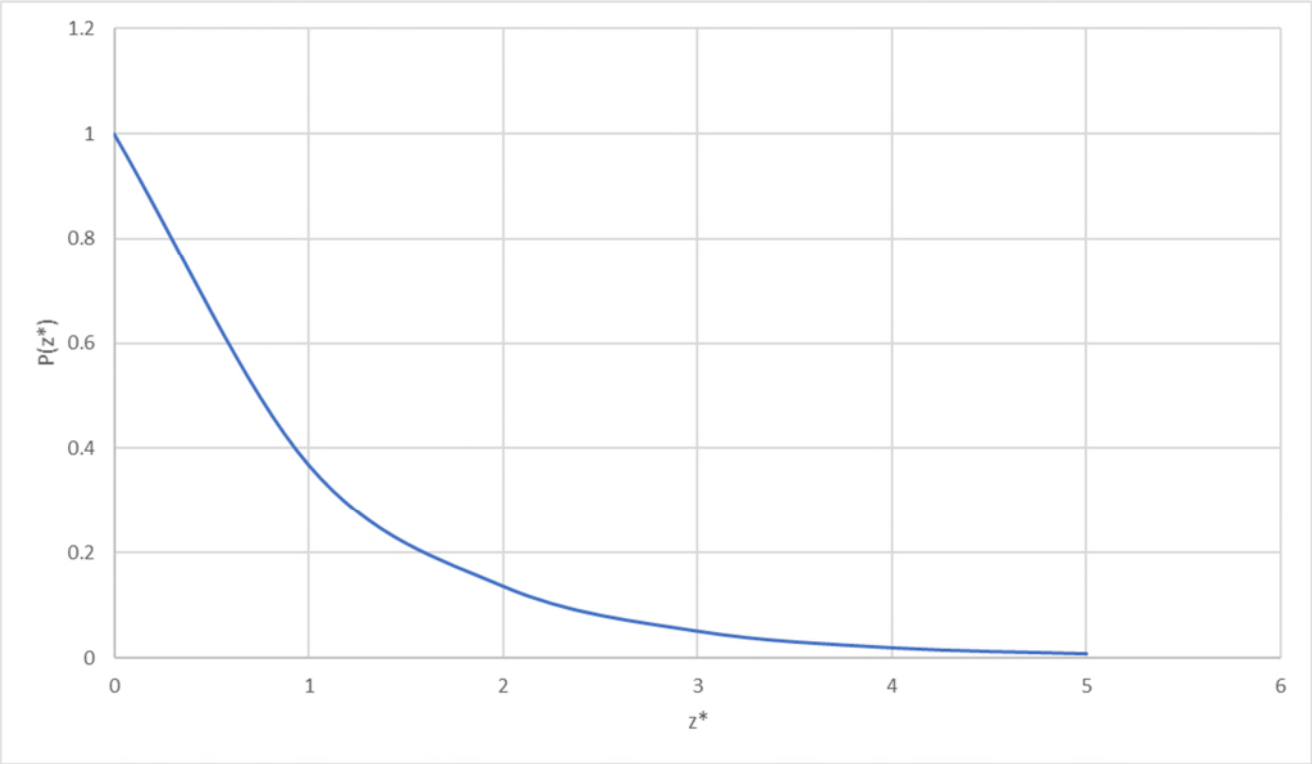

Figure 45: Distribution of asperity heights following an exponential probability density function

Greenwood also presented another exponential type of distribution that could be used. It is given by equation (4-65):

$$\Phi(z^*) = ce^{-\lambda z^*} \quad \textbf{(4-65)}$$

Where c and λ are constant coefficients.

Using an exponential distribution, it becomes possible to solve the relevant contact equations for the contact loads, the real area of contact and the number of contacting asperities analytically. The exponential distribution is used by several other researchers as well [125]. However, in several of Greenwood's literature, he presented the simple exponential distribution function as inadequate and proposed to use the modified exponential distribution instead [126]. In more recent works, Greenwood has advocated for the use of the modified exponential distribution function but without the coefficient c as c is assumed to be equal to 1 [127]. In the case where a gaussian distribution would represent a case better than the exponential distribution, it is always possible to

modify the coefficient constants to match the Gaussian distribution function more accurately. This makes the exponential distribution function a more versatile function to use [128]

4.4.1.2 Gaussian Distribution function

The classic Greenwood-Williamson model on asperity distribution was formulated by using a Gaussian distribution function. This means that the asperity height distribution followed a Gaussian probability density function. It was suggested that; based on experimental evidence, the height distribution for many engineering surfaces tends to be Gaussian. Even when the asperity heights are not entirely Gaussian, the uppermost peaks of the asperities form a reasonable approximation to a Gaussian distribution function. The Gaussian distribution function is shown in equation (4-66):

$$\Phi(z^*) = \frac{1}{\sqrt{2\pi}} e^{-\frac{1}{2}z^{*2}} \quad \textbf{(4-66)}$$

It is illustrated in figure 46.

Unlike the exponential distribution, contact mechanics for Gaussian distribution functions cannot be solved analytically. As such, numerical methods are used and assumptions for physical parameters are made.

Since Gaussian distributions are harder to work with, a modified exponential distribution is used in the MATLAB program. There are two cases of interest. In the analytical model, the pin is assumed to not wear out or bend. As such, it remains elastic. The asperities on the disc can either remain elastic or plastic. The two contact situations are therefore elastic-elastic and elastic-plastic. In the case of elastic-elastic, it was shown that it was possible to use a modified exponential distribution function to closely approximate the Gaussian distribution function. The simple exponential distribution function was shown to be inadequate, however, as there is a large variation at different loads between it and the Gaussian distribution function. In the case of elastic-plastic contacts, a similar result can be observed. Although, the result from the simple exponential function diverges significantly from the ones obtained using the

Gaussian distribution function, the modified exponential function provides results which are close to the Gaussian distribution function [129]. This shows that the modified exponential function is a reasonable approximation for estimating the initial height distribution of the asperities.

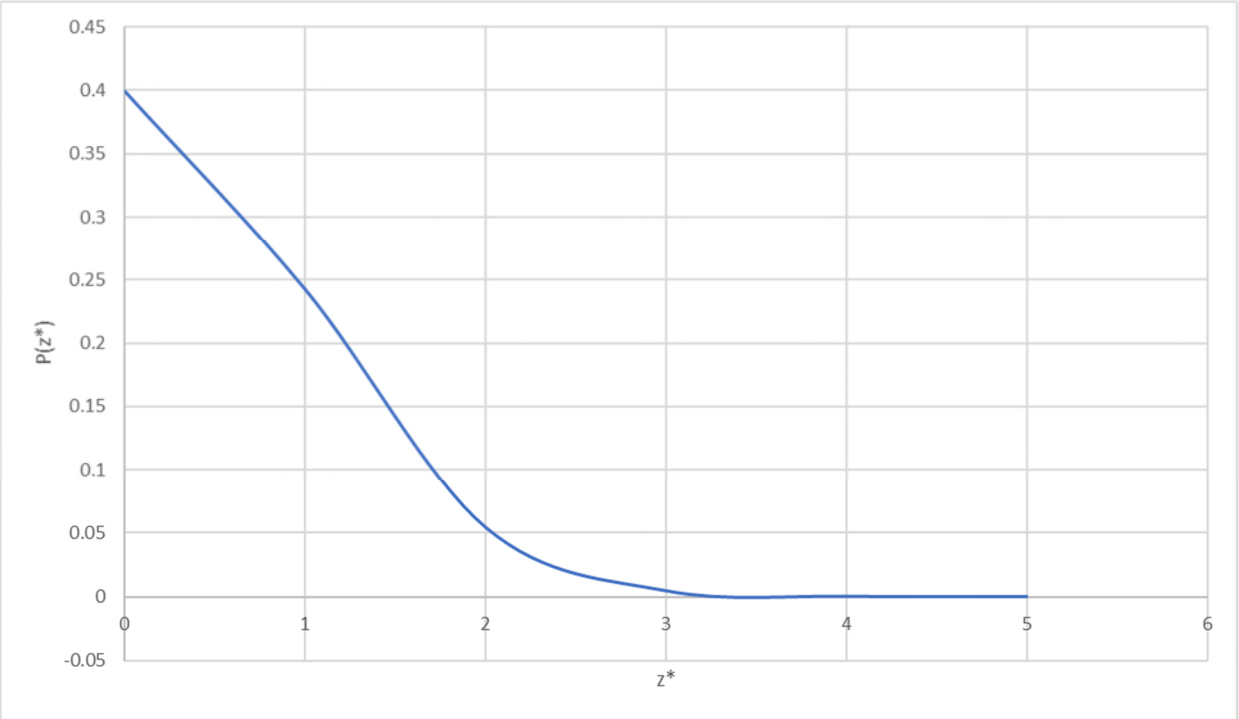

Figure 46: Distribution of asperity heights following a Gaussian probability density function

After generating the initial asperity distribution, the program first calculates which asperities on the disc are being struck by the pin as well as the stresses on each asperity as per the analytical model as shown below. Based on those stresses, the MATLAB program will assign a label to each asperity on the disc. Label “2” for asperities that are still in elastic conditions and label “4” for asperities that have worn out.

```
Vasp(k) = CrossA * R(k);
    MassAsp(k) = Vasp(k)* density;
    CritDamping(k) = MassAsp(k)*2*Omega;
    DampingCoefficient(k) = 4*(0.04e-
03)*R(k)*sqrt(((2*MassAsp(k))/(pi*BM*temp))*Pressure);
    DampingRatio(k) = DampingCoefficient(k) / CritDamping(k);
    if k ~= length(R)
        if R(k) - R(k+1) < DistPinTravel(k)
            F(k) = (MassAsp(k)*v)/t;
            M(k) = F(k)*(R(k)-(DistPinTravel(k)));
```

```
            Stress(k)=M(k)/S;
            initvel(k) = 0;
            DistPinTravel(k) = (initvel(k)* TBC(k))+
0.5*9.8*((TBC(k))^2);

for c = 1:ncols-1
    if Stress(c) > yield && Stress(c) < UTS
        Test(c) = 3;
    elseif Stress(c) >= UTS
        Test(c) = 4;
    else
        Test(c) = 2;
    end
end
```

If the asperities are elastically vibrating, then the theory detailed in 4.3.3 applies and the sound pressure can be calculated from the vibrational displacement:

```
VibrVel(c) = -DampingRatio(c)*Omega*O*displacement(c)*exp(-
DampingRatio(c)*Omega*O)*cos(Omega*O)-displacement(c)*exp(-
DampingRatio(c)*Omega*O)*sin(Omega*O);
        P(c) = airdens*soundvel*CrossA*radeff*(VibrVel(c)^2);
```

If the asperities are worn out, then the volume of the asperity is added to the total wear volume; and a new asperity is generated in its place by substituting equation (4-63) into (4-26).

```
R(L) = ((G*J*sqrt((((J^2)/4)*(b^2))-(J*b*((R(L)+x)^0.5))+(R(L)+x))-
initvel(L))/(J*((R(L)+x)^0.5))-initvel(L))*exp(log10(G*exp((-
G*(x+(((J^2)/4)*(b^2))-(J*b*((R(L)+x)^0.5))+R(L)+x)))));
```

The program then calculates the energy released by the impact along with the sound pressure as per section 4.3.4.

```
E(c) = Hardness*pi*((d/2)^3)*Beta;
        P(c) = CrossA*soundvel*E(c);
```

The full MATLAB code is provided in appendix A.

4.5 Analytical results and discussion

The analytical results are shown in figures 47-50:

Figure 47 shows that mild steel has the highest amount of wear under a 10 N load and aluminium T351 has the lowest. This is consistent with other research and also expected as aluminium T351 is heat treated to be wear-resistant and so has a higher ultimate tensile strength. This leads to fewer asperities breaking and more asperities remaining in the elastic regime and for longer periods of time. Furthermore, the difference between the ultimate tensile strength and the yield strength means that the corresponding plastic zone is much larger in

aluminium T351 than in either iron or mild steel. A larger plastic zone means that the asperities spend a longer amount of time in plastic deformation and take longer to wear out. Those results are therefore consistent with material properties.

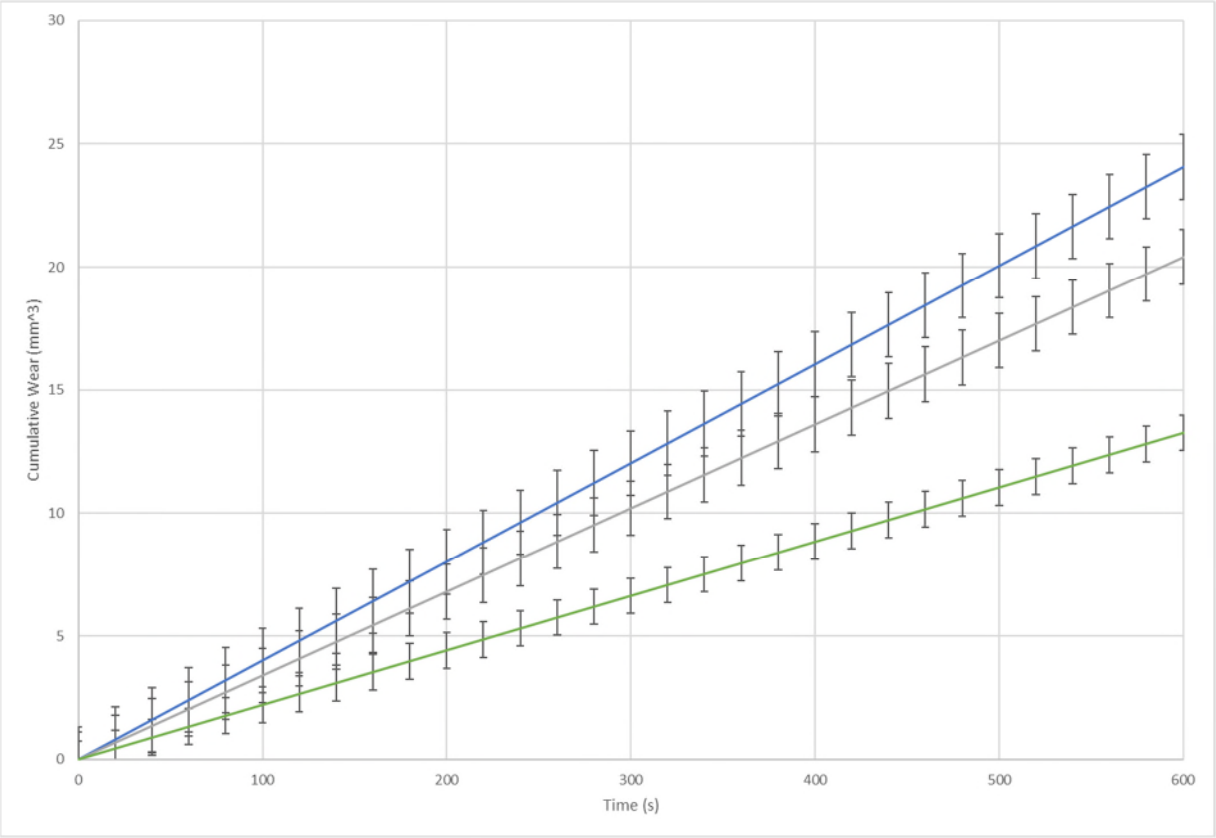

Figure 47: Cumulative wear under a 10N load for mild steel (blue), iron (grey), and aluminium T351 (green)

As seen in other research, a higher wear correlates to a higher sound pressure. The analytical model supports this conclusion as the sound pressure is much higher at a higher load, than at a lower load. This correlates to a higher wear.

Aluminium is shown to have the lowest wear. This is due to the higher UTS value of aluminium T351. However, it is shown to have higher wear than under a 10 N load. This is consistent with existing research. A higher load on the pin asperity leads to a higher impact force. The vibrational displacement of the elastically vibrating asperities is therefore higher and so the transition to the plastic deformation (which ultimately leads to wear is also higher).

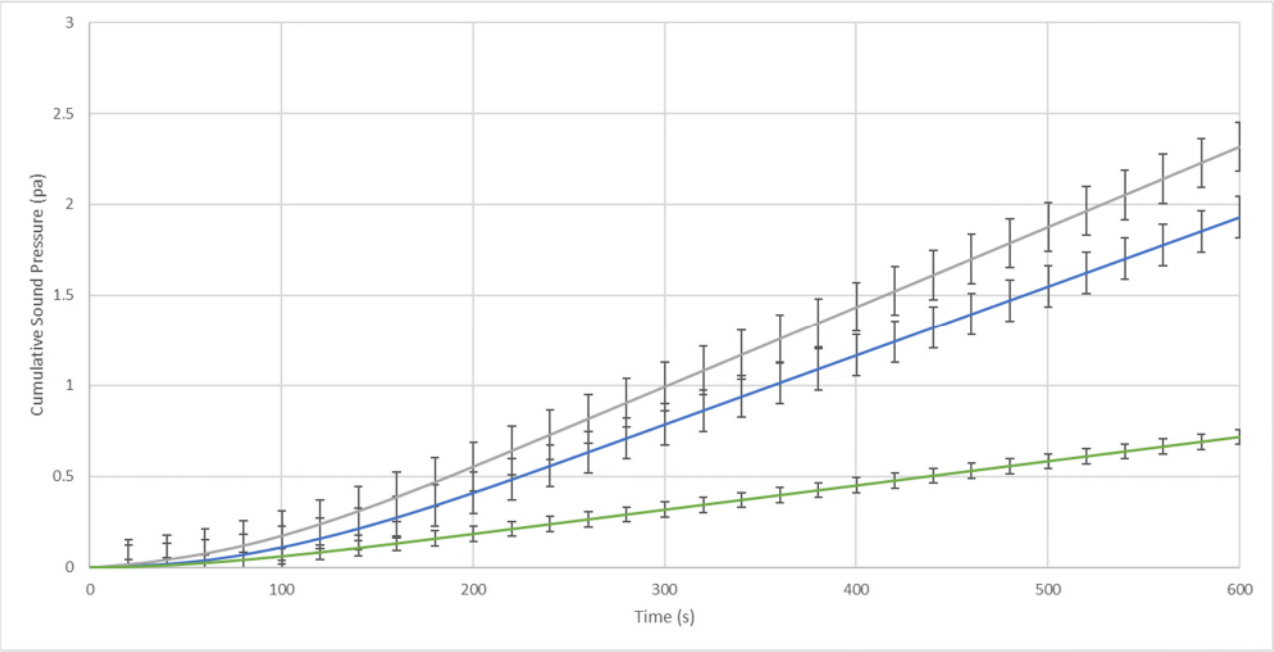

Figure 48: Cumulative Sound Pressure under a 10 N load for mild steel (blue), iron (grey) and aluminium (green)

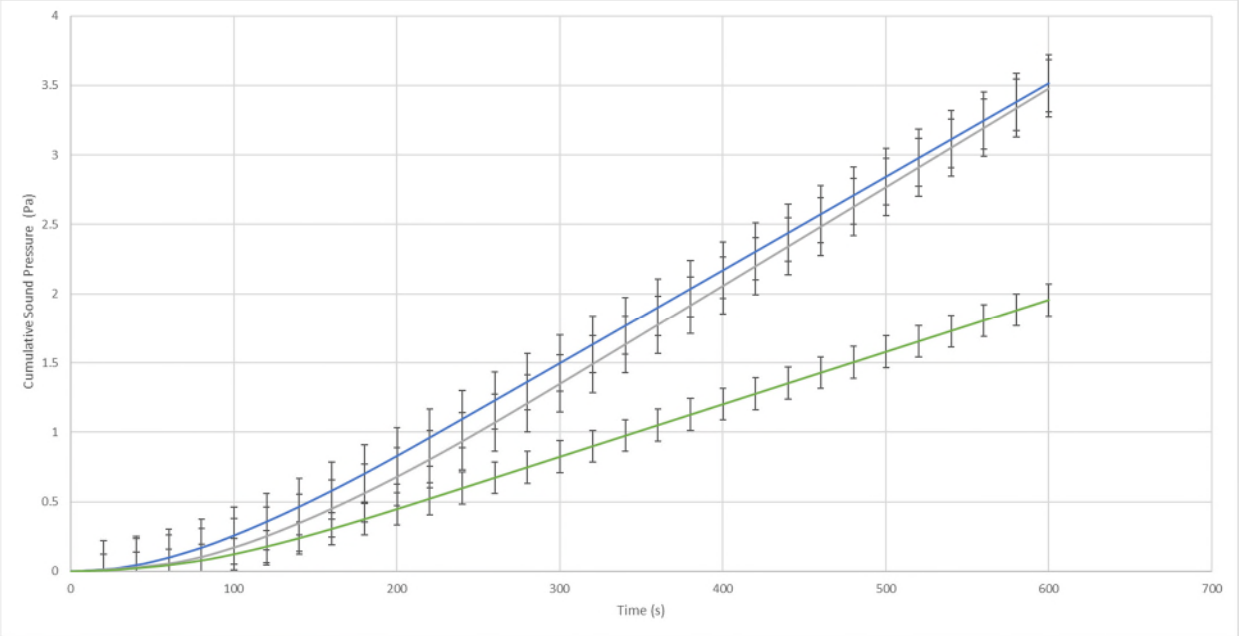

Figure 49: Cumulative Sound Pressure under a 20 N load for mild steel (blue), iron (grey) and aluminium (green)

The shape of the graphs is of an interesting nature. At constant velocity, the increase in wear is linear. This is expected from an analytical perspective as the solution to the differential equation is linear. From the sound pressure graphs, the relationship is also mostly linear with a differed start. This occurs because the starting cycles provide a low sound pressure generation due to the fact that there is very little wear at the beginning. However, as the wear increases, the sound pressure generation reaches an “equilibrium” state and provides a constant increase.

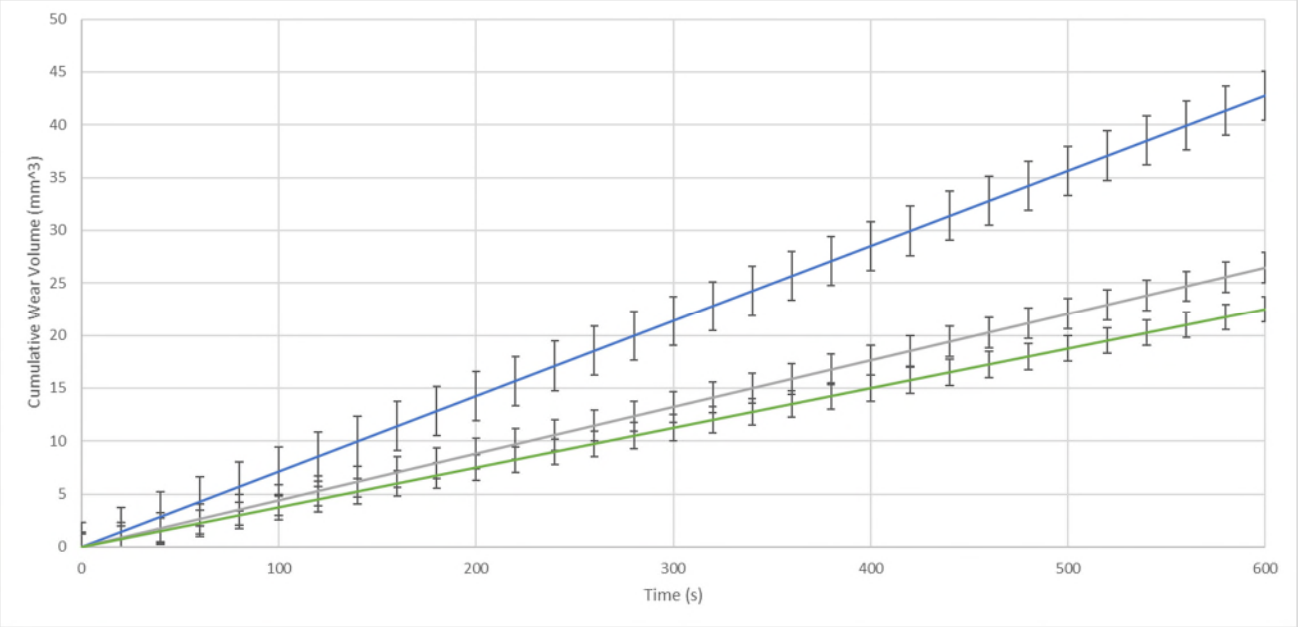

Figure 50: Wear under a 20 N load for mild steel (blue), iron (grey) and aluminium (green).

The effect of temperature was also investigated. The temperature factor in the MATLAB model is used to calculate the damping coefficient as follows:

```
DampingCoefficient(k) = 4*(0.04e-
03)*R(k)*sqrt(((2*MassAsp(k))/(pi*BM*temp))*Pressure)
```

As the temperature increases, the damping coefficient decreases. This leads to an increase in the damping ratio:

```
DampingRatio(k) = DampingCoefficient(k) / CritDamping(k)
```

As such, the vibrational displacement is higher:

```
Ddisplacement(c) = displacement(c)*exp(-
1*DampingRatio(c)*O)*cos(Omega*O);
```

This predictably leads to a higher sound generation and higher wear as the asperities will quickly plastically deform and break. The analytical results for the sound pressure and wear at 60°C are shown in figures 51 and 52.

Aluminium has a higher wear amount than iron as the aluminium used in the high temperature experiments was not heat-treated. The sound pressure is also much higher for aluminium. It is interesting to note, however, that despite having a higher wear, iron under a 20 N load has a lower sound pressure than aluminium under a 10 N load. This could be due to the fact that the plastic zone for iron is much higher than that for aluminium. As such, since most asperities transition quickly to the plastic zone due to the higher load, they remain in the plastic zone for a longer amount of time. This reduces the number of asperities contributing to the noise generation and so noise remains lower; even at higher loads.

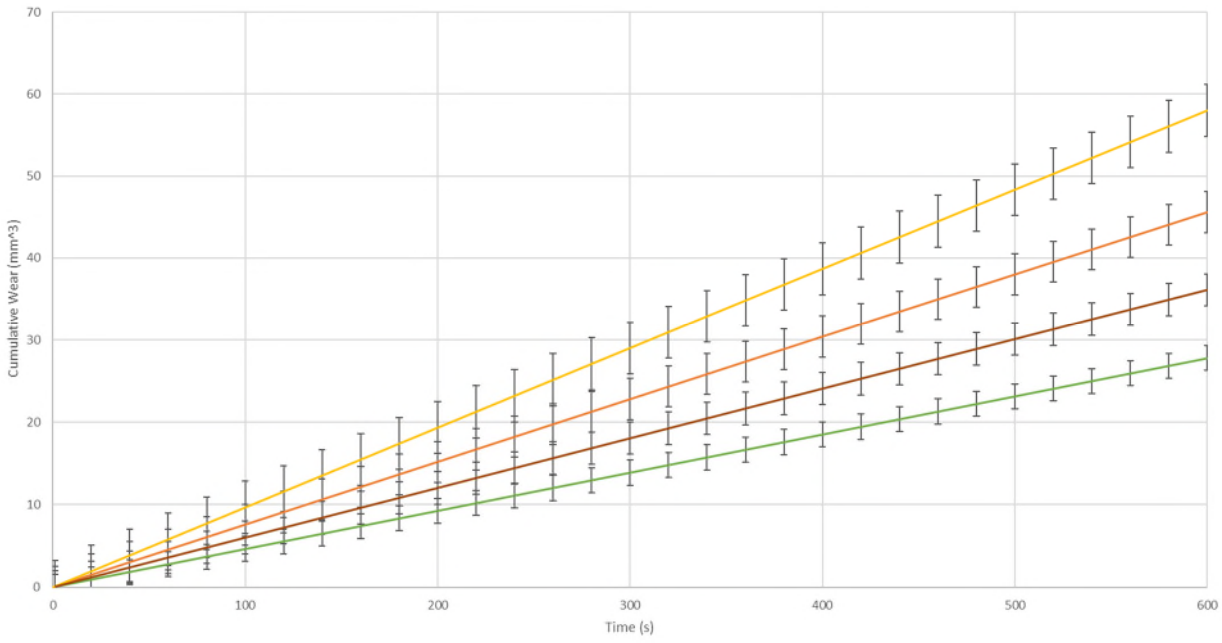

Figure 51: Cumulative Wear of iron (orange) and aluminium (yellow)under a 20 N load and iron (green) and aluminium (brown) under a 10 N load at 60° C

From an analytical perspective, the shape of the graphs at room-temperatures and at higher temperatures is the same. This is because there are no changes to the underlying functions with respect to the temperature. The inclusion of

temperature is used to calculate the energy of the impacts which then affects the vibrational velocity or the wear of the asperities.

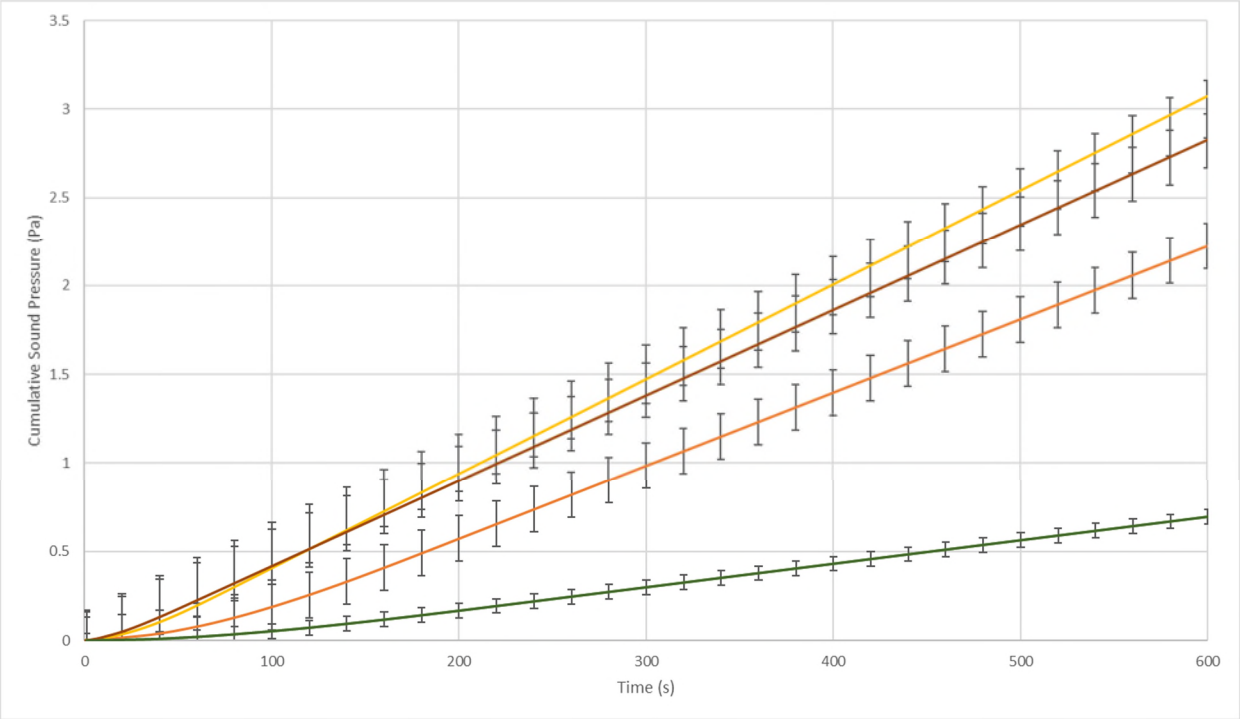

Figure 52: Cumulative Sound pressure for iron (orange) and aluminium (yellow) under a 20 N and iron (green) and aluminium (brown) under a 10 N load at 60 °C

5 Experimental Validation

In order to validate the analytical approach, a set of pin-on-discs experiments were performed on various materials at constant sliding speeds under varying load conditions. No lubrication was used in the experiments. The experimental validation was comprised of two stages. In the first stage, the experiments were performed under lab temperature conditions. In the second stage of the experimental validation, heat was applied to the samples in order to examine the behaviour of the samples at temperatures above room temperatures. This was used to assess the accuracy of the analytical model at higher temperatures. The two stages are detailed in the following two sections.

5.1 First stage of the experimental validation

The first stage of the experimental validation involved performing a set of pin-on-disc experiments to assess the accuracy of the analytical results at room temperature. The experiments were performed according to the following experimental scheme. All experiments were performed at 300 RPM and each experiment ran for 10 minutes. It was initially decided that both the loads and the speeds would vary. However, it was found that loads higher than 20 N at 300 RPM would trigger the inbuilt force sensor safety. Furthermore, 10 N loads applied at 600 RPM would also trigger the inbuilt force sensor safety. As such, it was made clear that both the loads and the speeds would not be able to be adjusted. It would have to be either the load or the speeds. It was felt that adjusting the load while keeping the speed constant would be more relevant for the experimental validation. Each test was repeated 3 times and the average values for the wear and the sound were taken. The discs were made to the specifications as detailed in figure 53. It should be noted that all the discs were polished using an 800-grit sandpaper in order to achieve a consistent surface roughness. In order to grind them, the discs were first put in a resin and then put in the grinding machine. Care was taken upon removal to make sure the discs were not damaged during the cutting of the resin.

Table 5: Experimental Scheme (room temperature experiments)

Experiment No.	External Load	Disc Material	Material Composition
1	10 N	Mild Steel	0.18% carbon
2	20 N		0.2 % silicon
			0.7 % manganese
			0.02 % sulphur
3	10 N	Aluminium T351	
4	20 N		
5	10 N	Iron	4 % carbon
6	20 N		3 % silicon

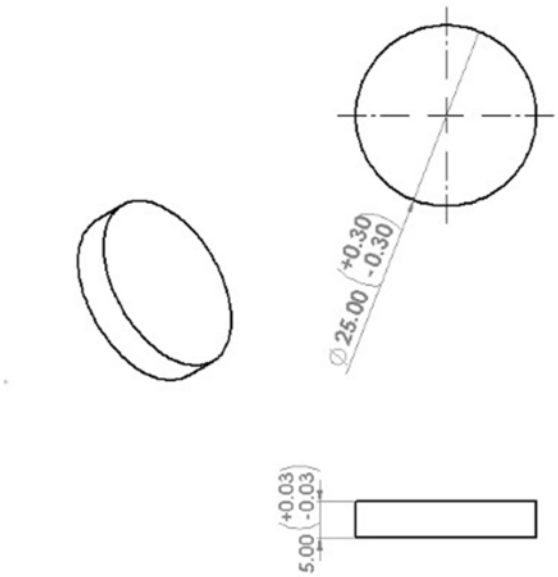

Figure 53: Disc specifications

The tribometer equipment used for the pin-on disc experiments is shown in figures 54 and 55:

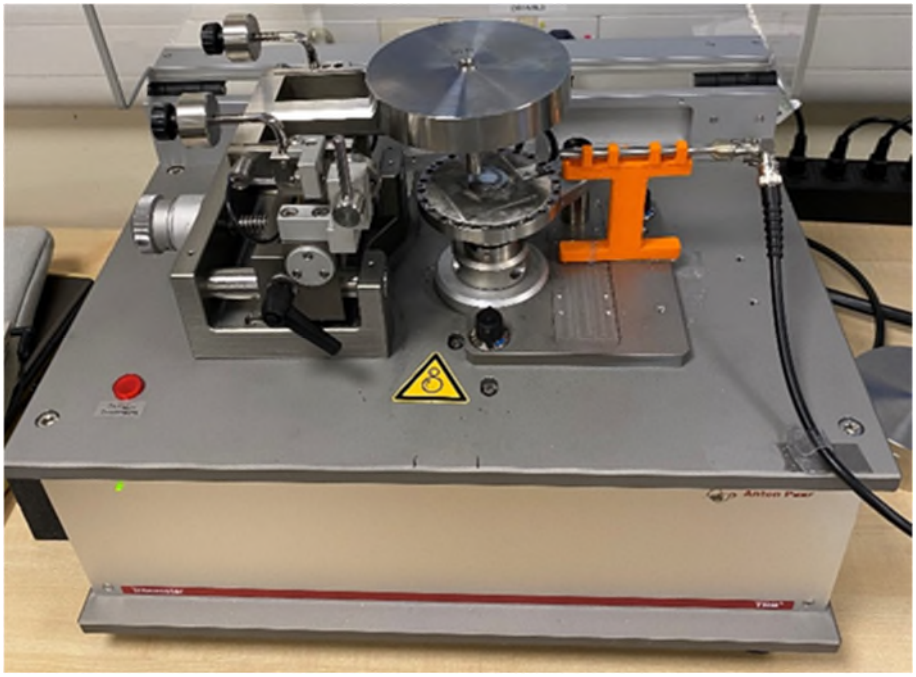

Figure 54: TRB^3 tribometer

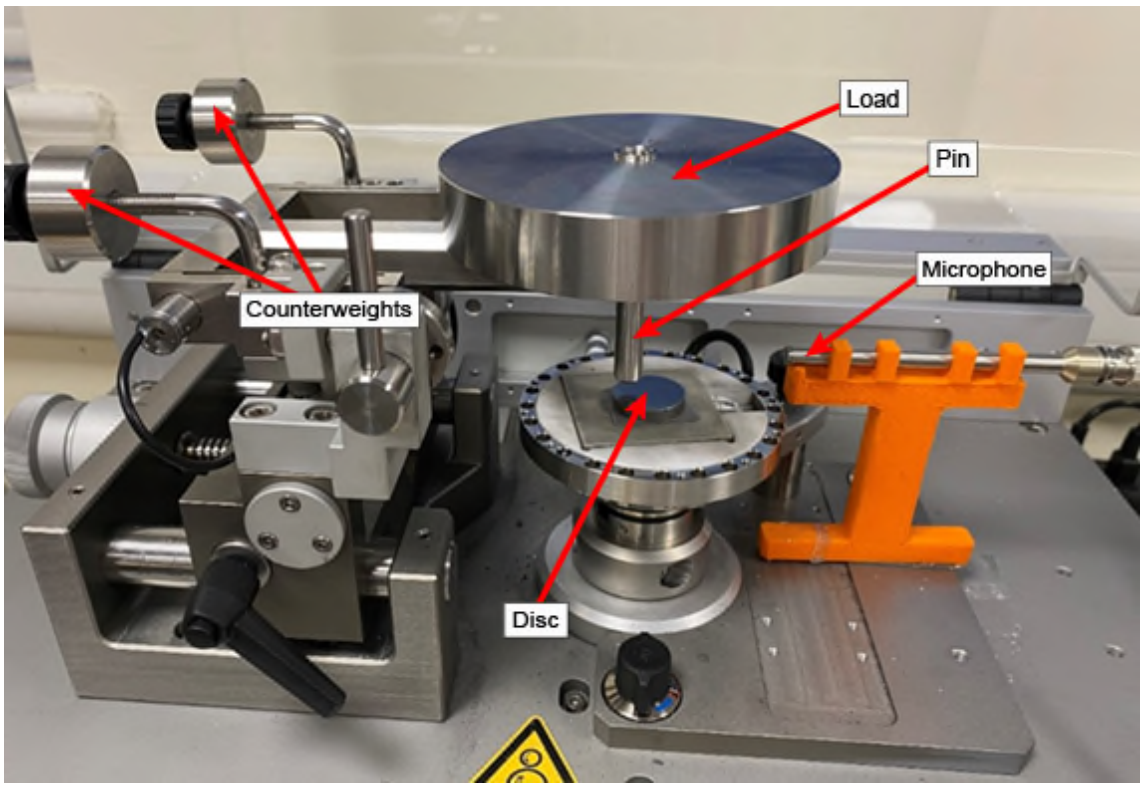

Figure 55: Close-up of the tribometer

In order to make sure that the load on the disc is the same as specified in the experimental scheme, the counterweights were essential as they were used to mitigate the weight of the pin. The stationary 3 mm radius pin (stainless steel 440C) was set up on a rotating disc. To be consistent with the model assumption that the pin would not wear out, it was checked between each experiment and visually inspected for signs of wear. The load was added on top of the pin and a rubber O-ring was used to minimise sources of vibration due to the movement of the tribometer. The microphone used was a GRAS condenser microphone with a maximum operating frequency of 20 kHz. The dynamic range of the microphone ranges from 18 dB to 133 dB. As such, it is best suited for measuring medium sound pressure levels at medium frequencies which is what the experimental validation required. The microphone used is able to measure the sound pressure directly as it was felt that sound pressure was the most appropriate component to measure and analyse. Sound frequencies were not captured because the relationship between the change in the sound frequency spectrum and the wear is much less straightforward to predict than the change in sound pressure and the wear. The sensitivity of the microphone was 47.46 mV/Pa. The full specifications of the microphone are shown in the following table:

Table 6: Microphone specifications

Polarisation/Connection		0 V /CCP
Frequency Range (±1 dB)	Hz	5 to 10 k
Frequency Range (±2 dB)	Hz	3.15 to 20 k
Dynamic range lower limit	dB	18
Dynamic range upper limit	dB	133
Set sensitivity	mV/Pa	47.46
Set sensitivity	dB re 1V/Pa	-26
Output impedance	Ω	<50
Power supply min to max	mA	2 to 20
Output Voltage min	V	8
DC Bias voltage min	V	16

Furthermore, the microphone was pointed directly at the source of the sound and placed as close to the pin as possible (around 10 cm away from the pin). Therefore, since the angle of incidence was exactly 0°, the accuracy was optimal. However, a few compromises were made in the experimental validation which could have had an effect on the results. For example, it is possible that the acoustic wave is multidirectional. The microphone was able to capture only one of the directions. It was assumed that this would be the most relevant direction. However, a more accurate way of setting up the microphone would have been to use an array microphone (which is a set of independent microphones) that could have been connected at different locations around the sample. The tribometer was ill-suited for this, however, and so it was not done. The tribometer was connected to a DAQ card (NI9174) which was then connected to a computer for the recording of the sound pressure measurements. The DAQ card is shown in figure 56. The sampling frequency of the operating equipment was set in a way that would compromise between the accuracy of the data and the number of recorded data samples. This is due to limitations within the data processing software that would limit the number of available measurement points. The sampling frequency of the penetration depths measurement of the tribometer was set at 100 Hz. The sampling frequency of the sound pressure data was set at 25.6 kHz. The sampling frequency of the penetration depth is a hardware limitation of the tribometer. As for the sound pressure measurements, the high sampling frequency increases the accuracy of the results during the processing of the data. To bypass the Excel limitations on the number of data points, the data was then decimated so that it would fit in Excel.

Figure 56: Close-up of the DAQ card

In order to check the consistency of the surface roughness for each sample, a set of interferometer images were taken. This surface roughness profile for each sample confirmed that the initial choice of asperity distribution (exponential distribution) was a suitable approximation to the real asperitical distribution. The interferometry measurements were taken at 3 random points on each sample and the average roughness values were calculated. In the interests of time, not all samples were tested in the interferometer as it was assumed that they would be mostly consistent since they were made to the same specifications. One sample from each set of experiments was tested. The results from one mild steel sample are shown in figure 57:

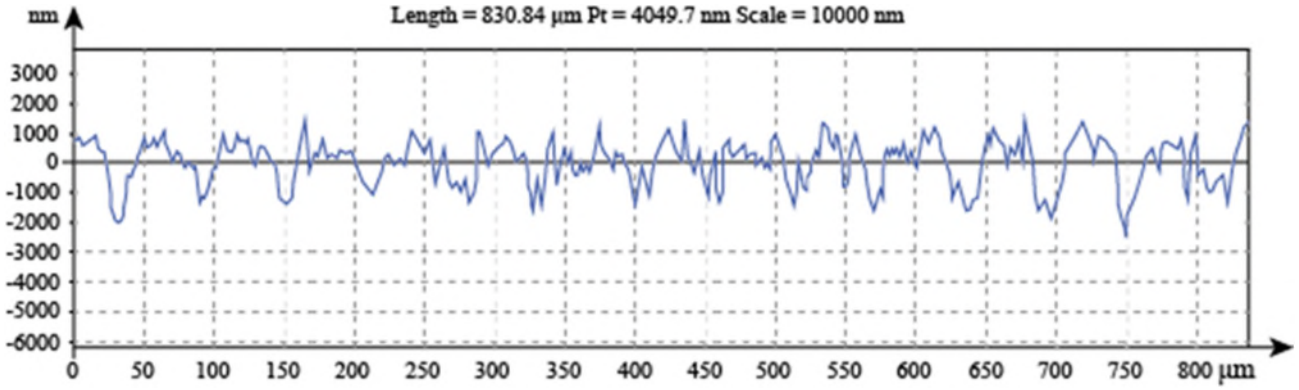

Figure 57: Surface Roughness profile for the mild steel sample

The surface roughness profile on the sample suggests that an exponential distribution is appropriate to model the asperity height distributions. As such, in the theoretical model, Φ (y, t) is assumed to be exponential and the mean value recorded by the interferometer was used in the original exponential distribution. A Gaussian distribution would be reflected by a smoother curve than the one shown in figure 56 and the rougher the curve is, the closer it is to an exponential distribution [130]

SEM images were also taken on a select number of samples at the end of each measurement cycle. The SEM images were used to determine what the main causes of sound generation would be. As shown in figure 58, the samples have undergone extensive wear. Plastic deformation can also be seen on the samples. However, the original assumption was that plastic deformation would not cause sound generation. This is because all the energy is used to deform the asperities plastically. Since there are no vibrations in asperities that have been deformed plastically, there can be no sound generation either. The SEM images were taken roughly on a 200 µm scale. This confirms that the mesoscopic scale is a reasonable approximation to use for the asperities. At that scale, it is reasonable to assume that the material properties of the asperities follow the same properties as the bulk material.

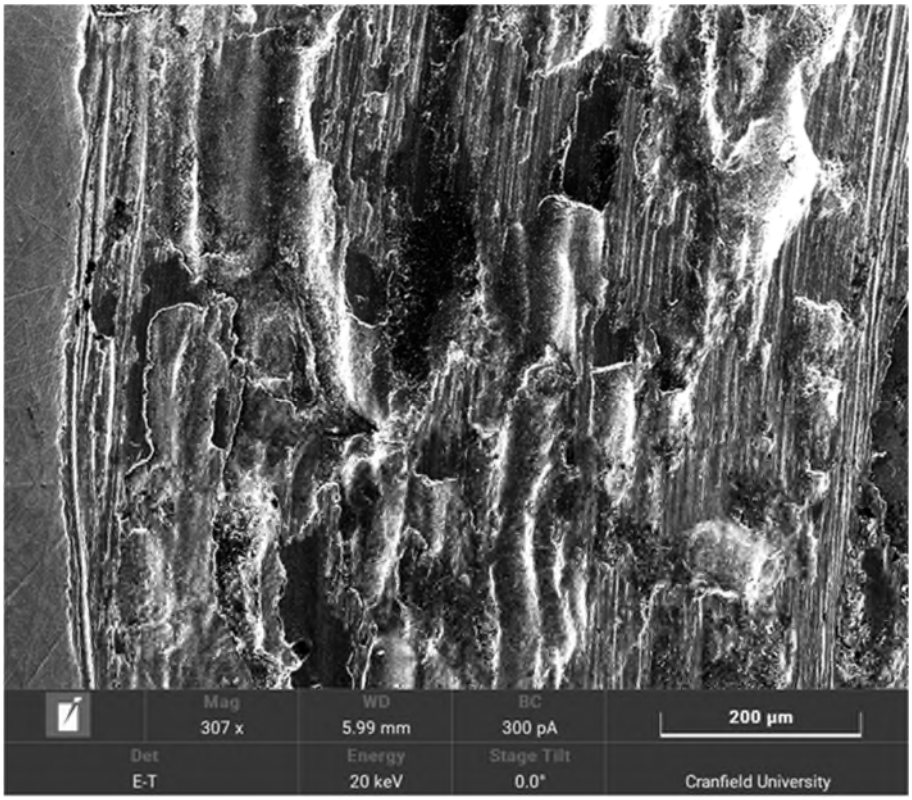

Figure 58: SEM image of the iron sample

Finally, a flowchart of the experimental scheme is shown in figure 59:

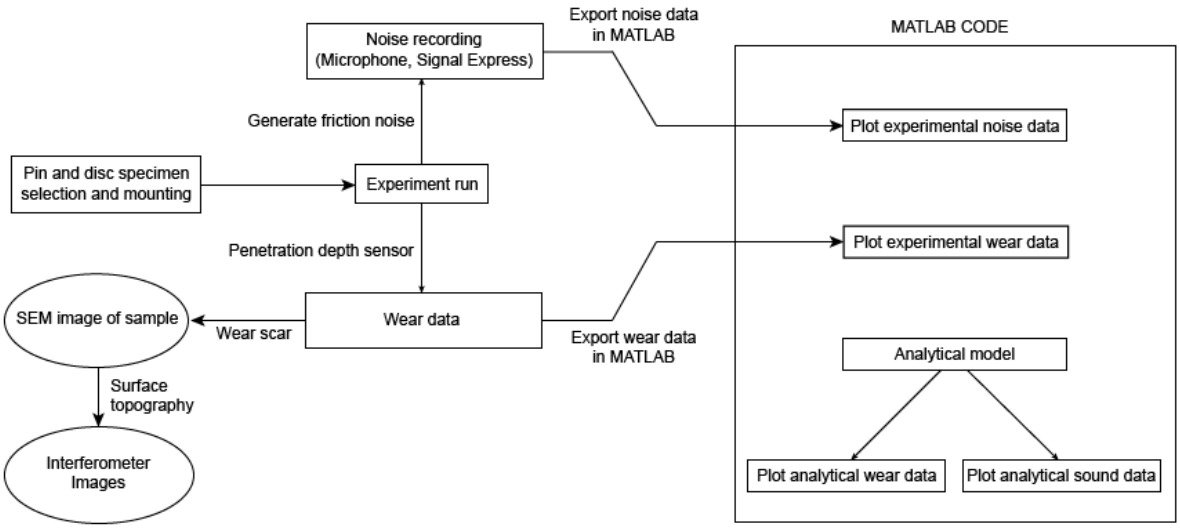

Figure 59: Flowchart of the experimental scheme

5.2 Second stage of the experimental validation

The second stage of the experimental validation was used to assess the accuracy of the analytical model at higher temperatures (above room conditions). In order to achieve that objective, a heating module was connected to the tribometer. It is shown in figure 60:

Figure 60: Tribometer heating unit

Using the heating module, a desired temperature could be set on the tribometer that would heat up the sample. The experimental scheme of the second validation experiments is shown in table 6. There were no modifications to the RPM and the runtime of each cycle. Each experiment was performed at 300 RPM for 10 minutes and repeated 3 times. The average values for the wear and the sound pressure were recorded. Similar to the first validation stage, the interferometry tests and SEM images were taken on select samples.

Table 7: Experimental scheme for the high-temperature experiments

Set No.	No. of Samples	Material	Load (N)	Temperature (°C)
1	1	Iron	10	Lab Temperature
2	3			60
3	1		20	Lab Temperature
4	3			60
5	1	Aluminum	10	Lab Temperature
6	3			60
7	1		20	Lab Temperature
8	3			60

As per the experimental scheme, one additional experiment was performed at room temperature to act as a control. One of the SEM images for the iron sample at 60 °C is shown in figure 60. As can be seen from the figure, there are a few differences between the SEM image at higher temperatures and the SEM image at room temperatures. At room temperatures, a larger number of asperities are undergoing plastic deformation at the end of the cycle. The SEM image showed a mixture of plastic deformation and wear. However, at higher temperatures, fewer asperities are undergoing plastic deformation. The SEM images shows extensive wear and little plastic deformation. This leads to a higher wear at the end of the cycle and thus a higher sound pressure. This is because asperities under plastic deformation do not contribute to either noise or wear. However, asperities that wear out do contribute to sound pressure.

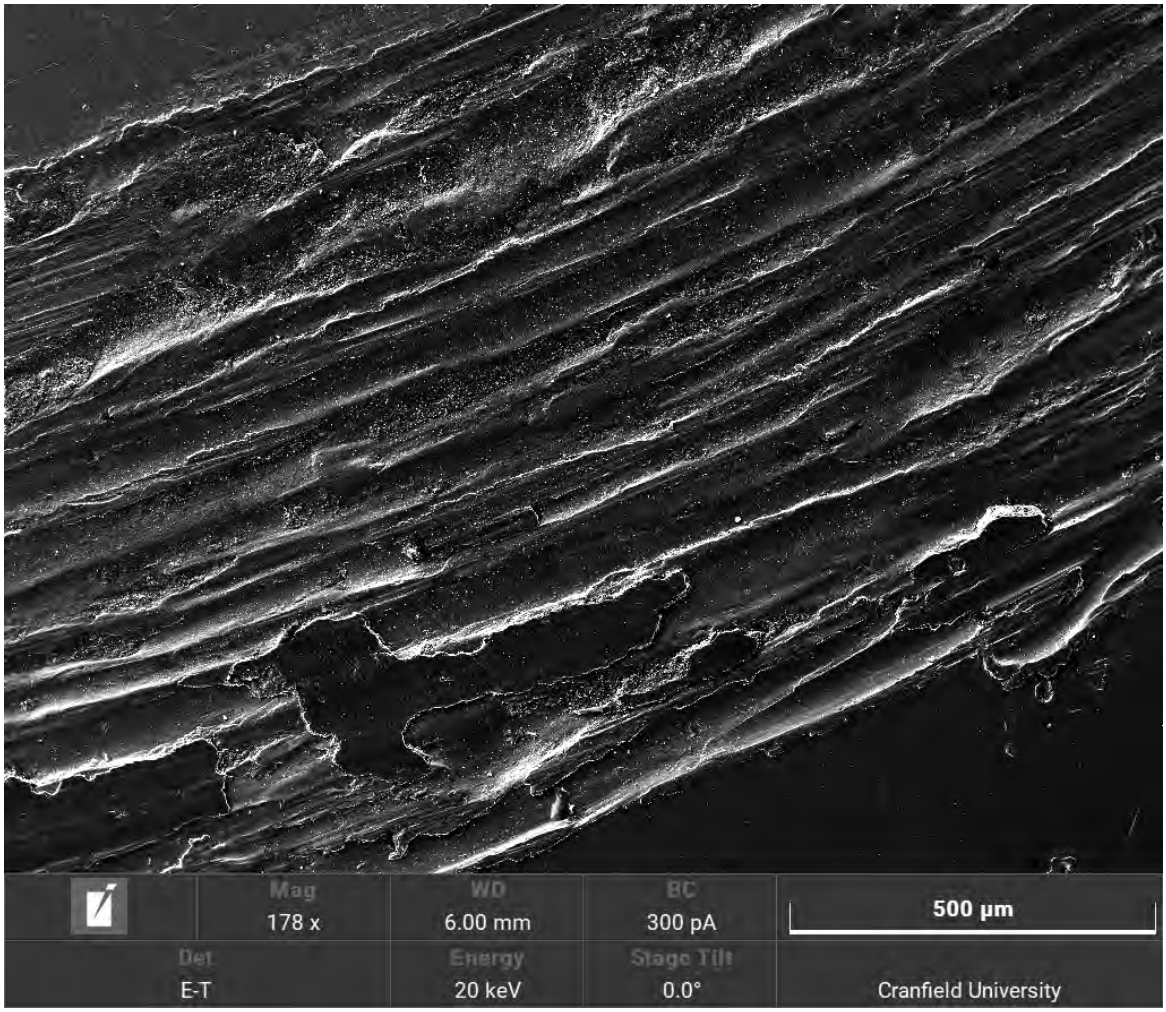

Figure 61: SEM image of an iron sample at 60°C

5.3 Processing the data

5.3.1 Wear data

The raw data output from the tribometer was the penetration depth. It was then necessary to convert the penetration depth into a wear volume that could be used in the analytical model. In order to do so, the area of the pin was calculated using equation (5-1):

$$A = \pi * r^2 \quad \textbf{(5-1)}$$

Where r is the radius of the pin. Using equation (5-1), it was possible to then calculate the area swept by the pin using equation (5-2):

$$A_{swept} = A * s \quad \textbf{(5-2)}$$

Where s is the distance travelled by the pin in one unit time. This represents the area swept by the pin. To calculate the wear volume, the area swept by the pin was then multiplied by the difference in penetration depth according to equation (5-3):

$$W = A_{swept} * (P_n - P_{n-1}) \quad \textbf{(5-3)}$$

Where P_n is the penetration depth value at time n and P_{n-1} is the penetration depth value at time n-1. It should be noted that the quantity of interest was the total wear volume and not the wear volume at any instant time. And so, the wear volume at every time step was summed with the wear volume at the previous time step. This gives the cumulative wear volume at every cycle, so the final value of the wear is the total wear volume at the end of the experimental run.

5.3.2 Processing the sound data

The raw data given by the microphone was the sound pressure data. In this case, the data was oversampled. This is because the maximum operating frequency of the microphone was 25.6 kHz. This resulted in more samples that could be used. Therefore, decimation was employed by downsampling the input data. It was downsampled by a factor of 50 in order to produce a suitable amount of data. The decimation process is shown as follows:

$$Y_i = X_{i*m+s} \quad \textbf{(5-4)}$$

For i = 0, 1, 2,…, size -1.

$$size = \left(\frac{n-s}{m}\right) \quad \textbf{(5-5)}$$

Where n is the number of elements in the input (undecimated data). m is the decimating factor (50). s is the start index (0), and size is the number of elements in the post-decimation results.

6 Experimental results and discussion

6.1 Lab temperature experiments

The wear data under a 10 N load and 20 N load are shown in figures 61 and 62 below.

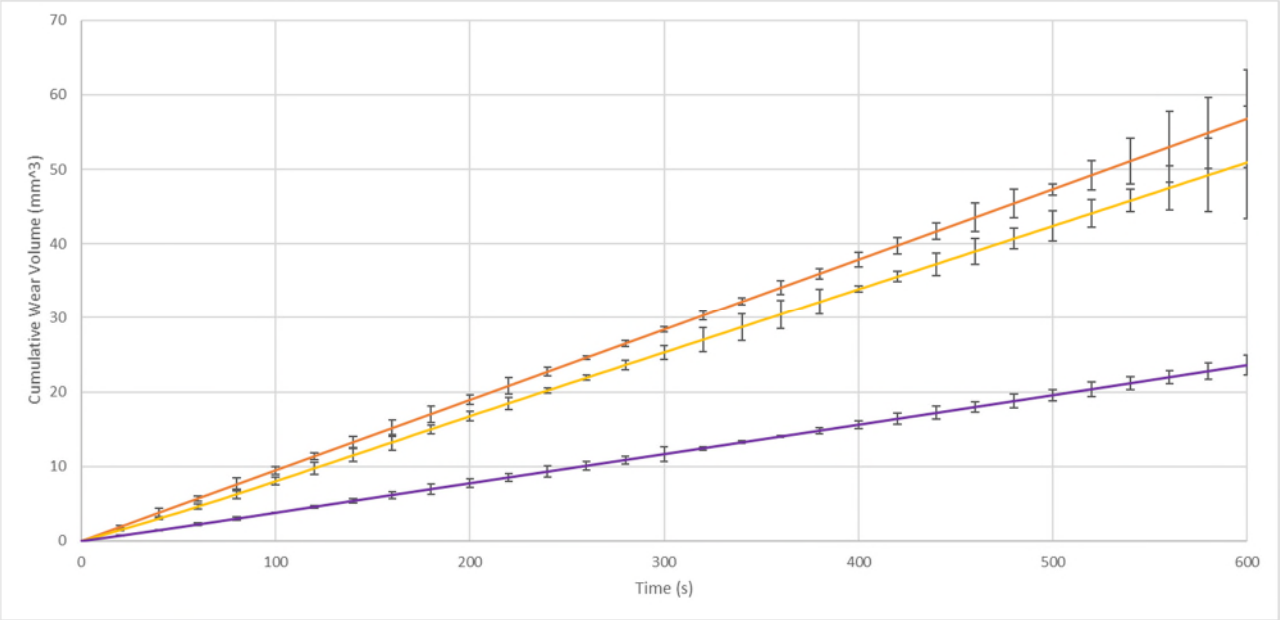

Figure 62: Cumulative Wear under 20 N load of mild steel (orange), iron (yellow) and aluminium (purple)

Figures 62 and 63 show that as the load increases, the wear also increases. This is consistent with existing research. Mild steel shows the highest wear with aluminium T351 showing the lowest amount of wear. This can be explained by material properties. The wear is caused by the breaking of the asperities. Aluminium T351 is heat-treated to be wear resistant. This means that it has a higher yield strength and ultimate tensile strength than either mild steel or iron. A higher yield strength means that the asperities will remain under elastic conditions for a higher amount of time before they enter the plastic zone. A higher ultimate tensile strength means that the asperities will take longer to break. Asperities under elastic or plastic deformation do not contribute to the wear (though asperities under plastic deformation can break and lead to the wear on subsequent cycles).

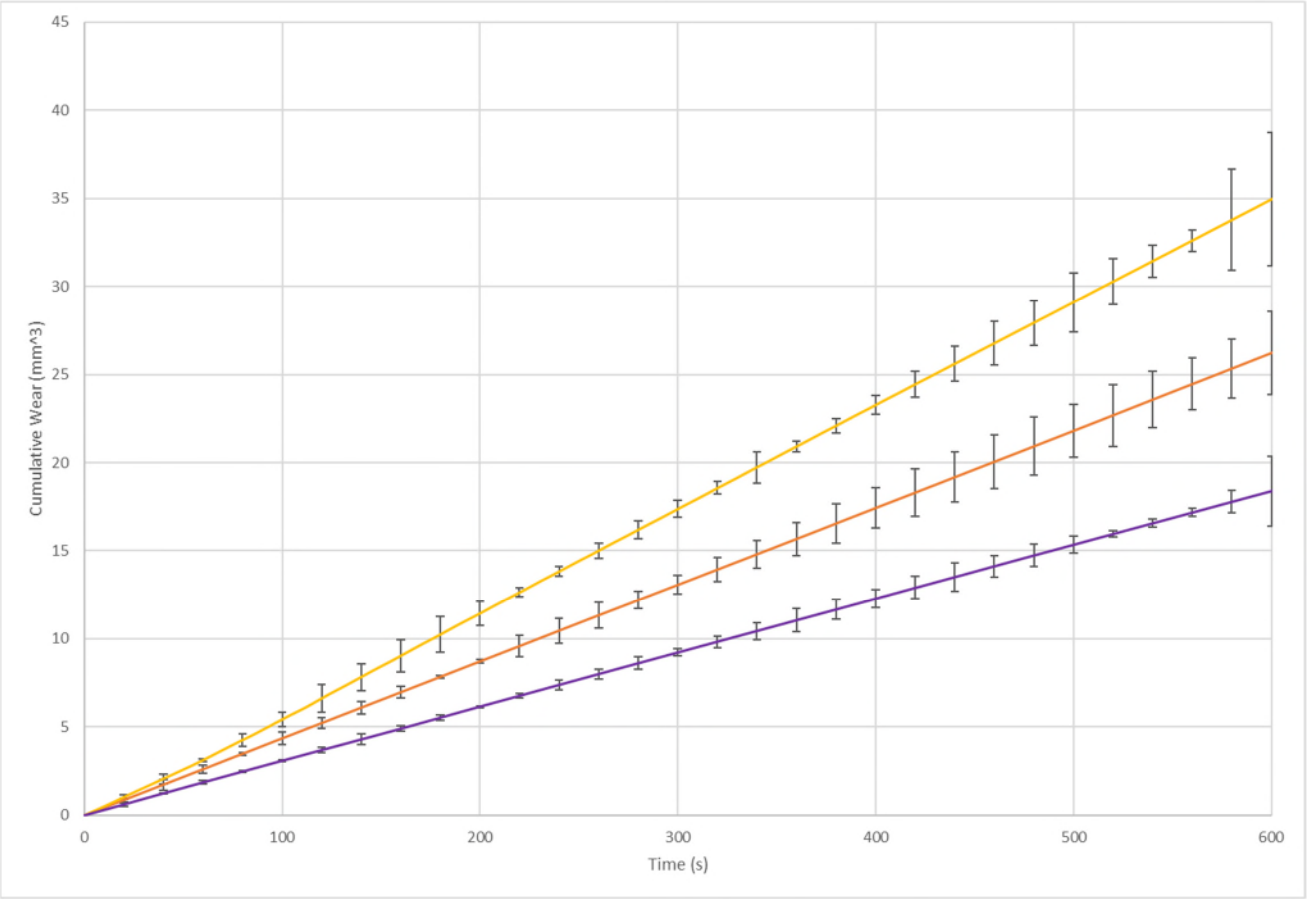

Figure 63: Cumulative Wear under 10 N load for mild steel (orange), iron (yellow) and aluminium (purple)

Figures 64 and 65 show the sound pressure for the samples at room temperature. It can be seen from those graphs that the sound pressure is much higher under a higher load than under a lower load. Furthermore, aluminium still has the lowest sound pressure whereas mild steel and iron have a much higher sound pressure. The sound pressure is correlated to the wear. As the asperities vibrate, they generate sound. However; the sound generation due to vibrating asperities provide a lower contribution to the sound generation due to the wear. As such, as wear increases; the sound pressure also increases. It should be noted, however, that asperities that undergo plastic deformation provide no contribution to the sound generation. Therefore, materials which have a large plastic zone generate comparatively less sound. For example, iron generates little more sound under 20 N load than it does under 10 N. This is because 10 N

is enough to cause most asperities to enter the plastic zone. A 20 N load just increases the number of asperities in the plastic zone and comparatively generates less wear than materials with a smaller plastic zone.

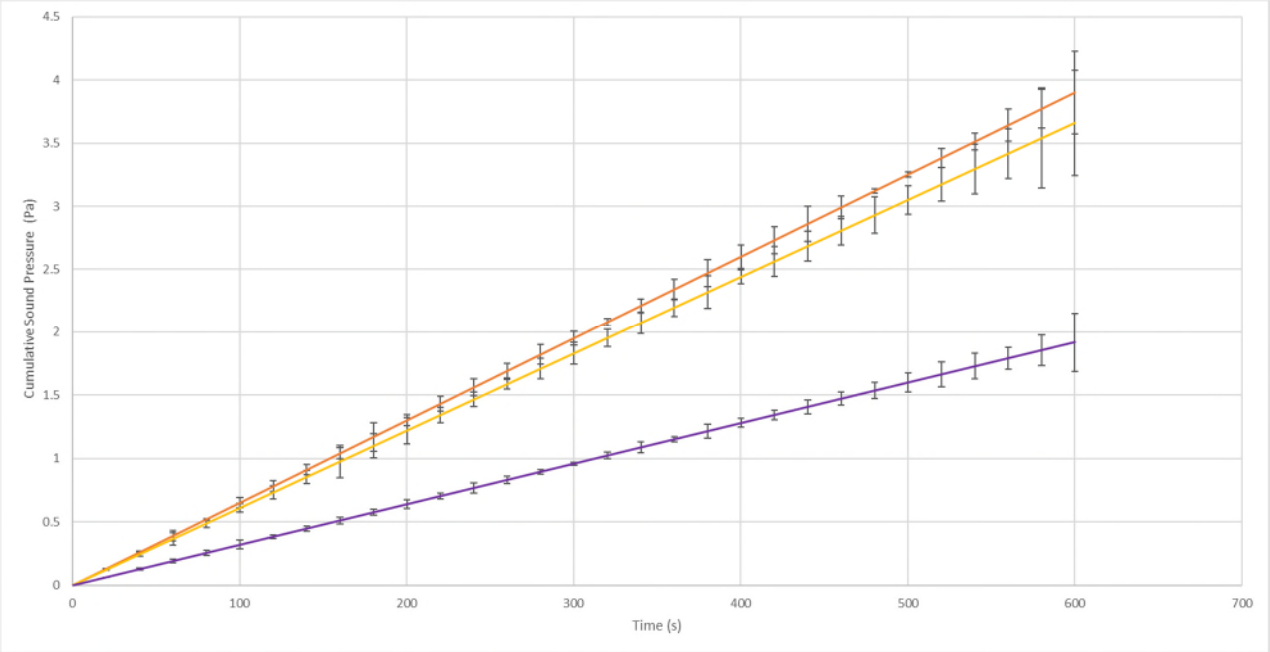

Figure 64: Sound pressure under 20 N load for mild steel (orange), iron (yellow) and aluminium (purple)

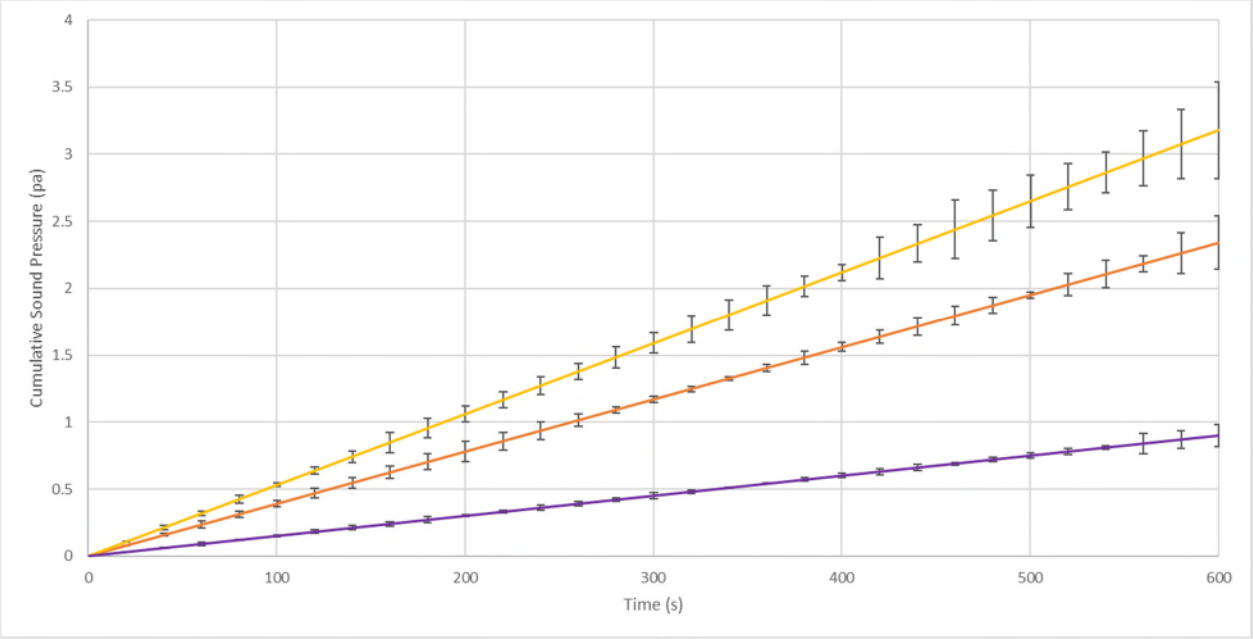

Figure 65: Sound pressure under 10 N load for mild steel (orange), iron (yellow) and aluminium (purple)

6.2 High temperature experiments

The experimental and wear and sound pressure data for the high temperature experiments at 60 °C are shown in figures 66 and 67.

As expected, a higher temperature generally leads to a higher wear both for a 10 N load and for a 20 N load. This is because a higher temperature leads to a higher impact energy. This extra energy causes a higher impact force and thus leads to more wear. The aluminium sample has the highest wear and the highest sound pressure both at 20 N load and at 10 N load. However, similarly to the analytical model, the iron sample shows a higher wear at 20 N load but a lower sound. Again, this is due to the large plastic zone which effectively reduces the number of asperities that are contributing to the sound in a unit time. Because the load and the impact energies are high, asperities quickly transition from the elastic zone to the plastic zone due to the low yield strength. However, due to the large plastic zone, they remain in it for much longer and this leads to a lower noise.

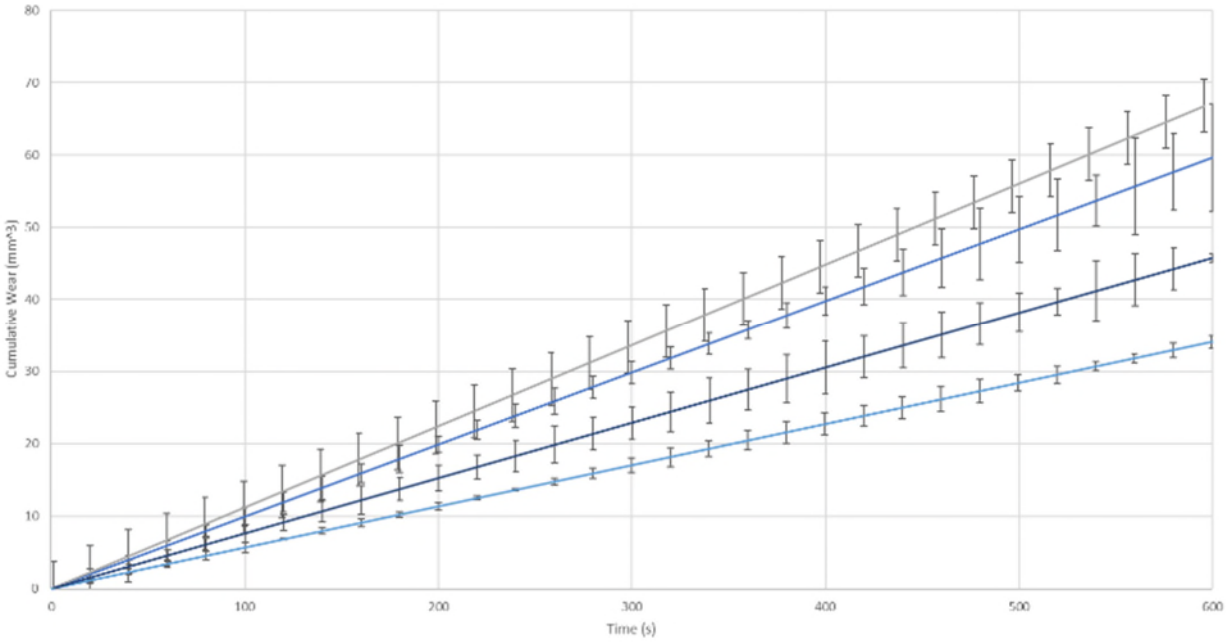

Figure 66: Wear of aluminium (grey), iron (blue) at 20 N load and aluminium (violet), iron (teal) at 10 N load.

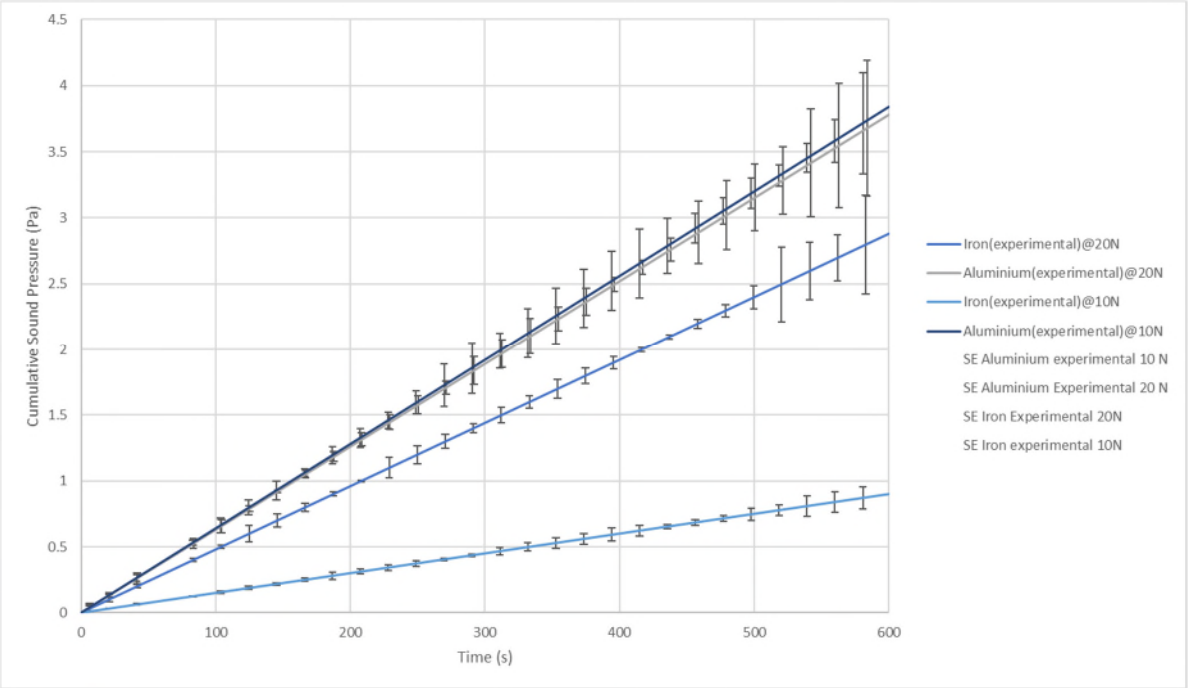

Figure 67: Cumulative Sound pressure of aluminium (grey), iron (blue) at 20 N load and aluminium (violet) and iron (teal) at 10 N load.

7 Comparison between the experimental and analytical results

7.1 Lab-temperature experiments

Figures 68 and 69 show the results at lab temperatures for both the analytical model and the experimental validation for the wear and the sound respectively under a 10 N load. Figures 70 and 71 show the results at lab temperatures for both the analytical model and the theoretical model for the wear and the sound respectively under a 20 N load.

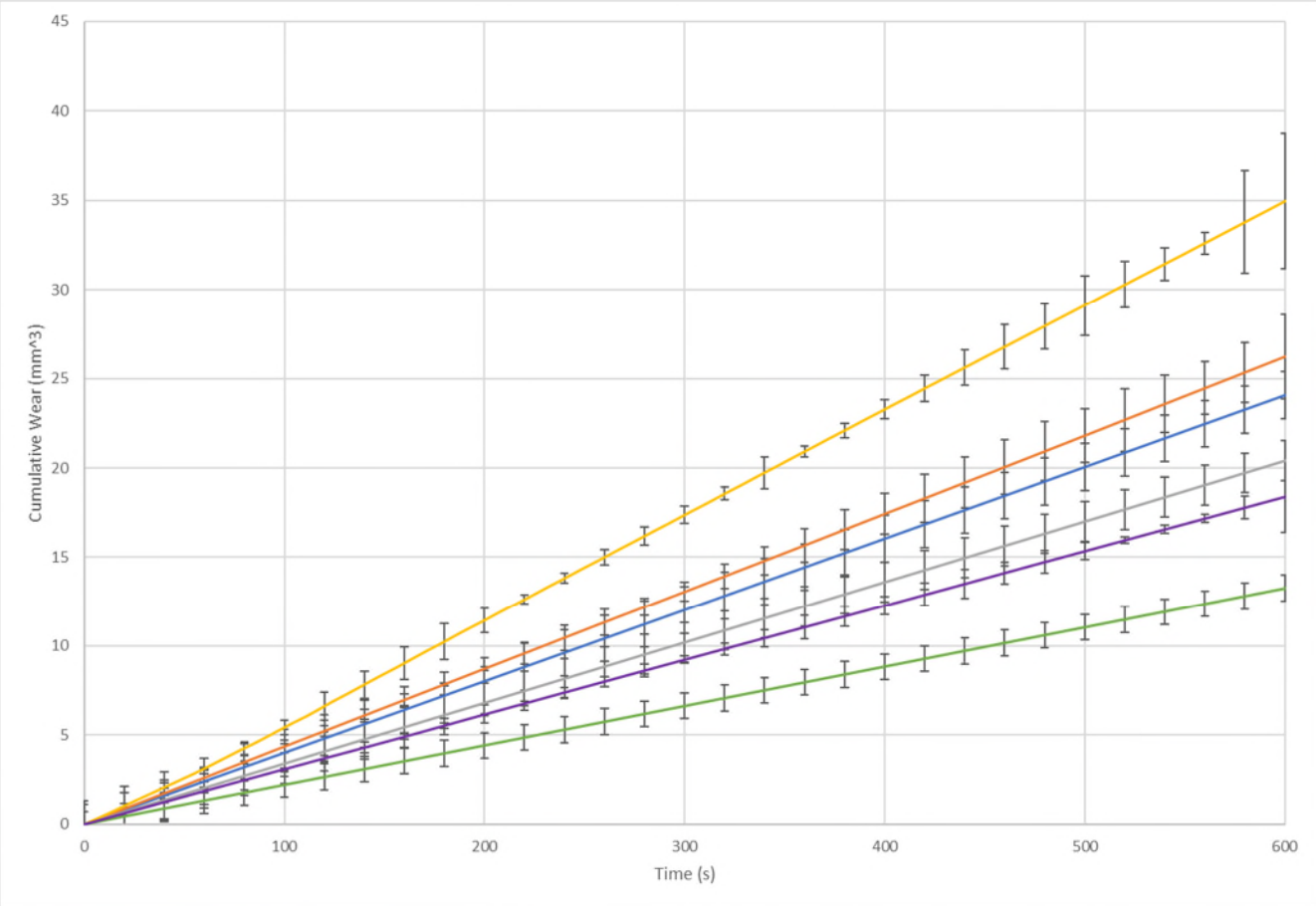

Figure 68: Theoretical wear results for iron (blue), mild steel (grey), and aluminium (green). Experimental wear results for iron (orange), mild steel (yellow) and aluminium purple under a 10 N load

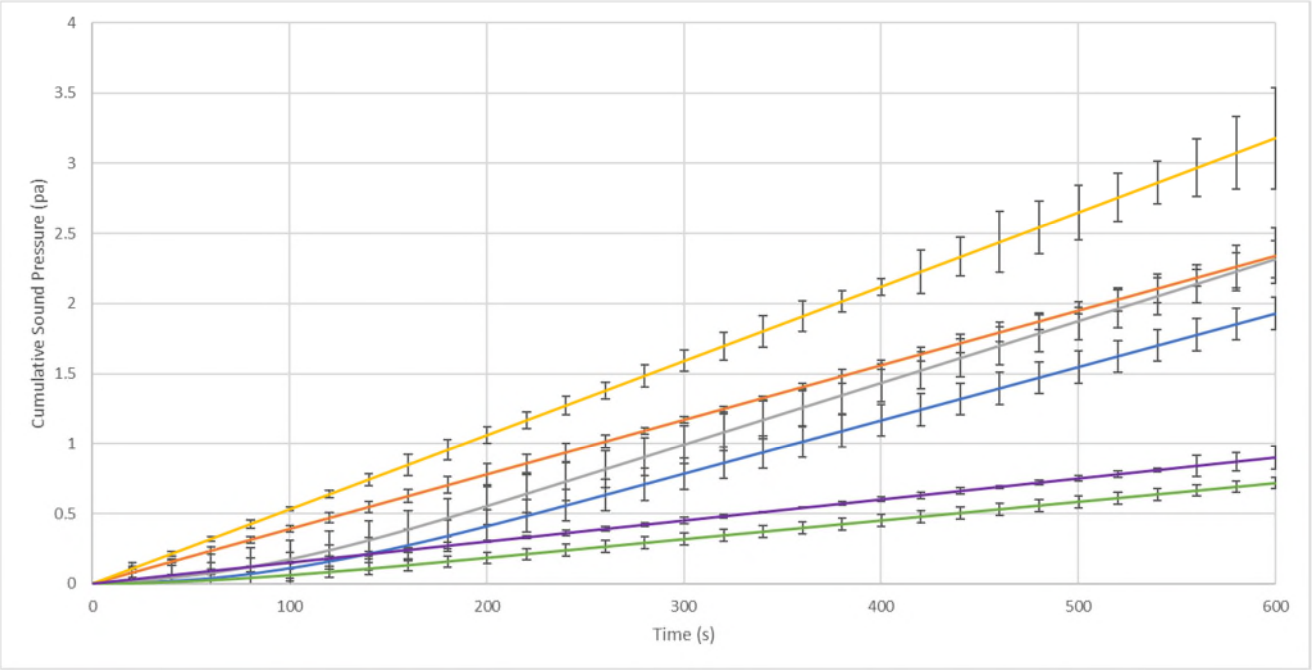

Figure 69: Theoretical sound pressure results for iron (blue), mild steel (grey), and aluminium (green). Experimental sound pressure results for iron (orange), mild steel (yellow) and aluminium purple under a 10 N load

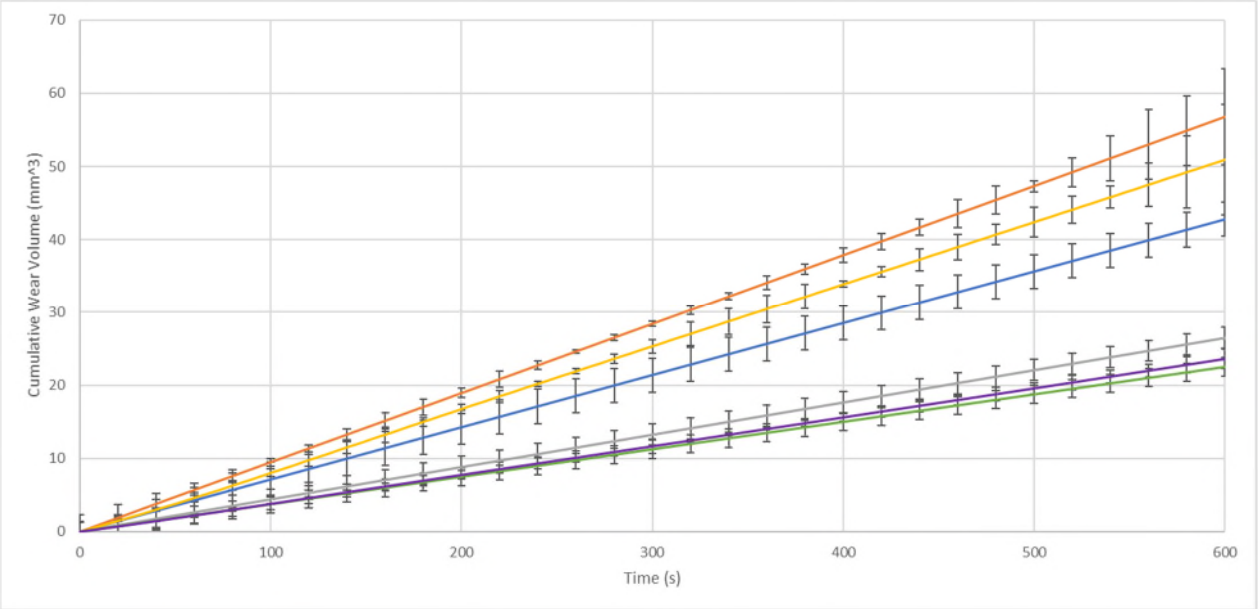

Figure 70: Theoretical wear results for iron (blue), mild steel (grey), and aluminium (green). Experimental wear results for iron (orange), mild steel (yellow) and aluminium purple under a 20 N load

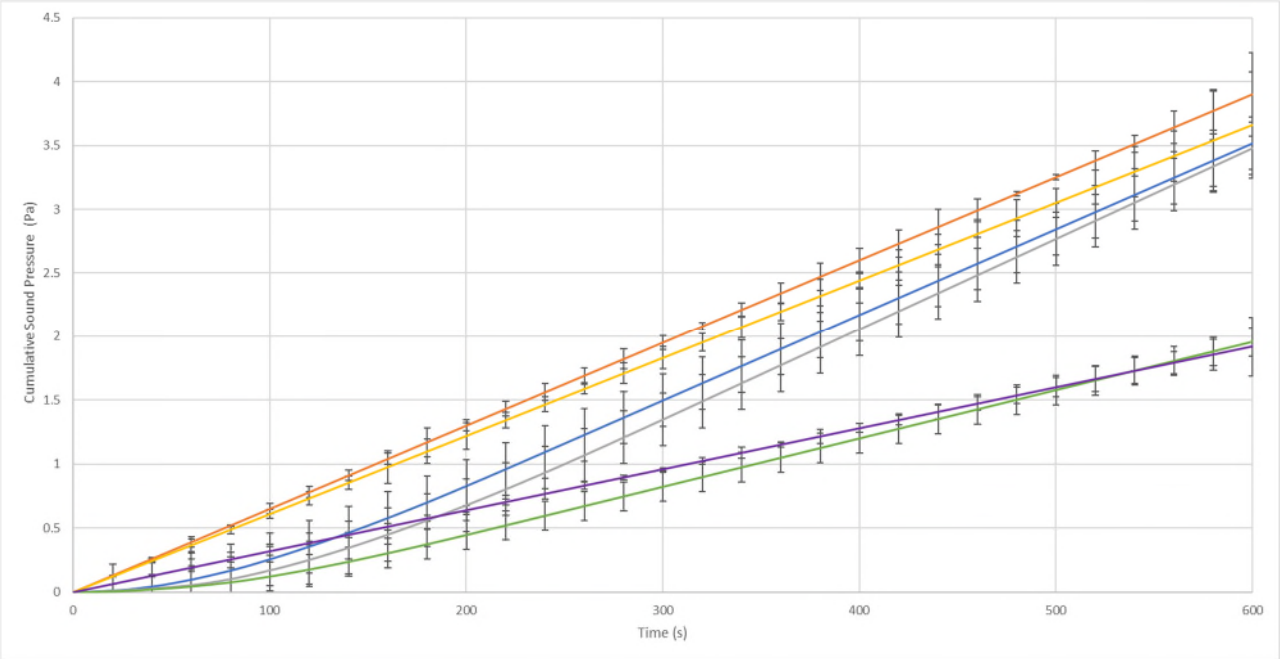

Figure 71: Theoretical sound pressure results for iron (blue), mild steel (grey), and aluminium (green). Experimental sound pressure results for iron (orange), mild steel (yellow) and aluminium purple under a 20 N load

7.1.1 Predicted and observed wear

From those results, out of the three materials, aluminium T351 undergoes the least wear. This is expected as heat treated aluminium is more wear resistant than either pure iron or mild steel. It can also be observed that the wear increases with increasing load [131]. The errors are calculated between the observed wear and the predicted wear. They are around 10 % for aluminium, 15 % for iron and 30 % for mild steel, which shows the larger error. The wear has been underestimated in the theoretical models. This could be due to several factors. First, the model was simplified. For example, the major assumption made is that the impact is a point impact on the asperities. However, this would not be the case in a real setup. The impacts would be a distributed impact across the asperity. However, modelling that would require a finite-element analysis on each asperity to determine how the force would be distributed and this is not done as it would be too computationally expensive. Similarly, the top asperity is assumed to be a single asperity contacting with one asperity at a time on the bottom surface. However, in the experimental setup, the pin would

be made from hundreds of asperities all interacting with hundreds of asperities on the bottom. This could be incorporated in this model as a refinement of the existing model. Moreover, the asperities were assumed to be independent. This resulted in an underestimate for the wear, as in a real asperitical distribution, it is possible that one asperity could impact the neighbouring asperity, thus causing a higher force than was estimated in the model. Finally, the asperities are modelled as cantilever beams out of simplicity. Therefore, they are assumed to behave as macroscopic cantilever beams

7.1.2 Predicted and observed sound pressure

From figures 63 and 64, a few numbers of different results can be deduced. First, the sound pressure generated is higher under a higher load than under a lower load. This is consistent with the existing research [132]. A higher sound generation is correlated to a higher wear [133], therefore, it is reasonable to assume that as the sound increases, so does the wear. Both the experimental and theoretical results show good correlation. Since the sound pressure is computed in the analytical using the wear, the magnitude of the error is similar for the sound pressure as it is for the wear. This is because the sound pressure is dependent on the wear. The sound increase is mostly linear as the experiment goes on. In those three materials, another conclusion that can be drawn is that iron generates the higher sound volume at 10 N followed, by mild steel. Aluminium generates the lowest amount of noise. This is because the aluminium is wear-resistant due to its heat treatment. The asperities spend a longer period in the elastic zone due to the high yield strength. Due to a lower number of breaking asperities, the sound produced by the aluminium disc is lower than for the other materials. This also correlates with a lower wear. The results also show that the amount of sound produced by the theoretical model has been underestimated. This could be because there are other sources of sound produced in the experiment that the model does not account for such as any external vibrations of the setup (although care has been taken to minimise them). The wear has also been underestimated in the theoretical model. Since

the wear is a major contributor in the production of sound, then that means that if the wear has been underestimated, then the sound produced is too.

7.2 High-temperature experiments

Figures 72 and 73 show the results at 60°C for both the analytical model and the experimental validation for the wear and the sound respectively under both a 10 N load and a 20N load.

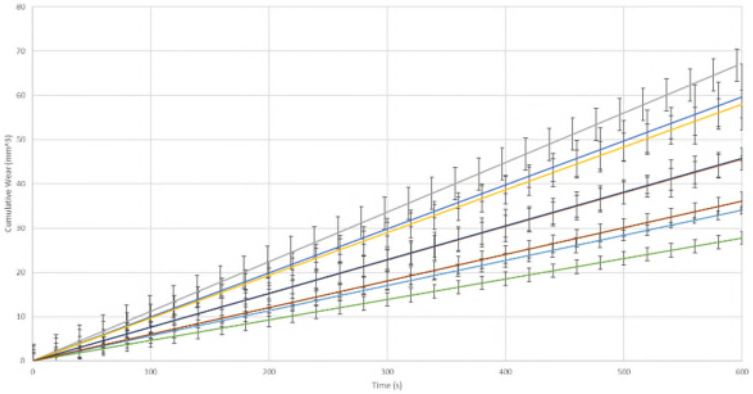

Figure 72: Theoretical wear results for iron (orange), aluminium (yellow) under 20 N load and iron (green), aluminium (brown) under 10 N load. Experimental wear results for iron (blue), aluminium (grey) under 20 N load and iron (teal), aluminium (violet) under 10 N load

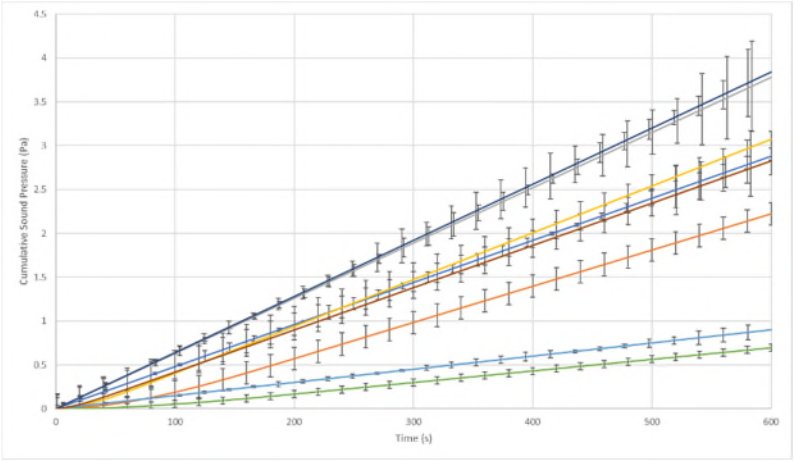

Figure 73: Theoretical sound pressure results for iron (orange), aluminium (yellow) under 20 N load and iron (green), aluminium (brown) under 10 N load. Experimental sound pressure results for iron (blue), aluminium (grey) under 20 N load and iron (teal), aluminium (violet) under 10 N load

7.2.1 Predicted and observed wear

The error between the analytical data and the theoretical data is larger in the case of the high-temperature experiments. This is because the limitations highlighted in section 6.1.1.1 are exacerbated by the initial application of heat. The model does include initial heat application as part of the theoretical calculations as this data is used to calculate the vibrational displacements and energy. However, as heat is applied to a sample, flash temperatures become more important. Flash temperatures are short-lived sudden increases in temperatures that occur due to the sliding friction processes. Those temperatures occur when asperities are struck since according to the theoretical model, not all of the energy is released as sound. Roughly half of the energy is released as heat. Due to the heat that is already initially applied to the sample, the combined effect of the applied heat and the flash temperatures do increase the wear rate. The model does not account for those. As the wear is already underestimated even with the absence of heat, the application of heat increases the error.

7.2.2 Predicted and observed sound pressure

Similarly, to the wear, the sound pressure is underestimated in the theoretical model due to the limitations of the model that were outlined in section 6.1.1.2. However, the error for the sound pressure is lower than the error in the wear. This is due to the ductility of the materials at higher temperatures. There are two contributors to the sound pressure: the elastic vibrations and the wear. The wear is a larger contributor than the elastic vibrations of the asperities. This is why as the wear increases; the sound pressure also increases. However, the size of the plastic zone affects the sound generation. If the plastic zone is large and the asperities enter the plastic zone quicker at higher temperatures, then less asperities are elastically vibrating at any given time and they remain in the plastic zone for long enough that; despite the increase in wear, enough asperities are in the plastic zone at any given time that this introduces an offset in the sound pressure generation as asperities in the plastic zone do not contribute to the sound pressure. This means that the higher wear has less of

an impact on the sound generation at a higher temperature than at a lower temperature. This explains the lower error in the theoretical model

8 Conclusion

This thesis presents a literature review that identifies a research gap due to the lack of an analytical approach to quantify the wear and sound pressure interdependencies during a sliding friction process. This thesis also presents a theoretical approach to predict the wear volume and the sound pressure generated during a sliding process for various materials under different loads in order to fill the research gap. The current approach implies that only two mechanisms are responsible for the generation of sound. The first mechanism is the elastic vibration of the asperities, and the second mechanism is the energy released during the breaking of the asperities. The results show that as the total sound pressure increases, so does the wear volume. This leads to the possibility of quantifying the wear present in the material by analysing the cumulated sound pressure that occurs during the sliding process. The theoretical model only requires the material properties to compute the wear and the predicted sound pressure which makes it a simple model to use in practical applications. However, there are several drawbacks to the model that limits its accuracy. For example, the initial assumption that the top surface is a single asperity causing a point impact on each disc asperity is an oversimplification that leads to the wear being underestimated. Similarly, the sound pressure estimated by the model has also been underestimated, although the error margin is less. Overall, the theoretical results qualitatively agree with the experimental results. This means that after further refining the model, such as by considering a distributed force of impact or lubrication, the ability to predict the wear generation based on the sound pressure generated could provide a non-destructive means of assessing the wear of materials

8.1 Achievement of objectives

The aimed objectives were as follows:

1. Identify the current research gap by performing a thorough literature review on the current work pertaining to the research topic.

2. Create an analytical model that encompasses the wear and the noise emitted during a sliding friction process at asperitical level.
3. Devise an experimental scheme that can be used to validate the theoretical approach. The experimental scheme includes a pin-on-disk experiment involving various materials under various loading conditions.
4. Validate the theoretical approach using the chosen experimental scheme.

8.1.1 Objective 1: Identify the current research gap by performing a thorough literature review on the current work pertaining to the research topic.

To achieve the first objective, a thorough literature review was performed. The literature review describes in the detail the research that was performed in the area, starting from the fundamentals of the physical area of contact and the asperities. It also describes the concept of friction and the wear at microscopic level. The literature review contains the depiction of several experimental, numerical, and analytical models ranging from the fundamental models of friction and wear, such as the Coulomb laws of friction and Archard's Wear models to the more advanced theoretical models. The literature review also considers the acoustics and the research performed on the airborne noise emissions during friction processes. The literature review shows that so far, a general analytical model that incorporates the sound produced and the wear into a unified model does not exist yet.

8.1.2 Objective 2: Create an analytical model that encompasses the wear and the noise emitted during a sliding friction process at asperitical level

To achieve the second objective, the model was split into four components. The first three components involved the behaviour of the asperities during the sliding friction process and the third component dealt with the noise mechanism. The asperities were assumed to be in one of three states. Either they would vibrate elastically, deform plastically or break. The sound mechanism would be different for two of those states (plastic deformation would not lead to sound generation).

In order to account for the wear, a separate model was developed that dealt with the asperitical changes during each cycle. As asperities break, they are replaced by new asperities. A mathematical relationship involving the height distribution of the asperities and a wear function was developed. The wear function would allow the original height distribution of the asperities to update via each subsequent cycle in order to account for the replacement of broken asperities with new asperities. To develop that model, a set of key assumptions were made in order to decrease the computational cost of the model and to simplify it. For example, only one of the surfaces was modelled (which was the surface undergoing wear). The other surface was assumed to not wear out. The asperities were also modelled as prismatic cantilever beams. This means they were assumed to be on a large enough scale that they follow macroscopic material properties. The flash temperatures were also not modelled. Flash temperatures occur during the sliding friction process where a sharp rise in temperature happens at the contact interface. The flash temperature dissipates quickly when the sliding stops. Finally, the impacts were modelled as point impacts as opposed to the more accurate distributed impacts.

8.1.3 Objective 3: Devise an experimental scheme that can be used to validate the theoretical approach. The experimental scheme includes a pin-on-disk experiment involving various materials under various loading conditions

To achieve the third objective, it was necessary to create an experimental scheme that would be able to assess the accuracy of the analytical model under different loading conditions and for various materials. The experiment scheme was comprised of two parts. The first part involved room-temperature experiments and the second part involved the initial application of heat using the heating module supplied. A suitable tribometer was chosen that could support automatic wear measurement along with a heating module that can provide the initial heat application. The tribometer also required a LEMO output that could be used to connect an external microphone on it. Different loads and temperatures were used but the sliding speed remained constant. A GRAS pressure microphone was used that could provide sound pressure

measurements. Interferometer measurements were also taken to provide the initial average roughness value and SEM images were taken to provide a visual for the samples.

8.1.4 Objective 4: Validate the theoretical approach using the chosen experimental scheme

The fourth objective involved performing the experiments in order to validate the theoretical results. The experiments were performed following the experimental scheme. The aim of the experiments was to corroborate the theoretical results under a varied range of different materials and loading conditions. Different materials have different physical properties, notable their degree of elasticity so it was important to test different materials Furthermore, loading conditions would also have an impact on the wear. As such, different loading conditions were also tested. Finally, the literature review has shown that the sliding speed and the initial temperature also has an importance on the wear.

The results from the theoretical and the experimental approaches were compared, and several conclusions were drawn from there. It appeared that the results were more accurate for lower wear and the error would increase as the wear increased. This could be due to a lower accuracy in determining the plastic region of a material. As such, more plastic materials that suffer from plastic deformation would give less accurate results than materials that go straight from elastic vibration to breakage (little plastic region). Three materials were tested in the experimental scheme: iron, mild steel and aluminium T351 Mild steel was shown to have the highest amount of wear, both from an experimental and theoretical perspective. This was also shown to have the highest error.

8.2 Contribution to knowledge

8.2.1 Asperity contribution to noise generation

The developed analytical model can predict the noise generated and the volume loss due to wear in a sliding friction process. This is done by analysing the behaviour of the asperities along with the mechanisms of sound generation.

The model is able to account for the different material properties such as the hardness, the elastic modulus and the UTS. External factors such as the temperature, loading conditions and sliding speed are also taken into account. Most of the properties involved in the modelling are generic enough in order to extend the possible scope of applications. Other factors such as the initial roughness distribution and the wear function are also left as generic as possible. They can be modified to suit particular applications if needed. For example, the initial roughness distribution was assumed to be exponential. But other forms of distributions exist, such as Gaussian distributions which are also used in other models

8.2.2 Analytical wear model

The wear model was developed in a way that can be easily modified to suit particular needs and conditions. This is because the wear model remained generic with as little assumptions as possible. The wear function was developed with the idea of prismatic cantilever beams. However, outside of that initial assumption, the model still remains generic and can be adapted with a different asperitical shape by modifying the initial wear function to suit another application. The model incorporates the sound generation based on the state of each individual asperity on the surface in a way that has not been done before. This is because, even though asperity-based analytical models of friction do exist, they do not include the wear or the noise into account. Similarly, numerical models of friction that exist do examine the relationship between the friction processes and the noise emitted (or in some cases, the acoustic emissions) but they do not take the wear into account either. This model unifies the friction, the wear, and the noise emissions into one general asperity-based model

8.3 Future work

Further work could go into further expanding the scope of applicability of the model as well as improving its accuracy. One way would be to model both surfaces of the samples (the pin surface and the disc surface). In the present model, only one surface is modelled with an asperitical height distribution. Using

the same method, it could be possible to model the second surface with another asperitical height distribution. Modelling both surfaces would provide a more accurate way of simulating asperity interactions. At every time step, the program could check the heights of every asperity, and this would allow the program to determine which of those asperities would cause an impact. This would likely increase the sound pressure and the wear of the analytical model. For both of these surfaces, one way to increase the accuracy of the model at the expense of computational cost would be to model a distributed impact force as opposed to a point impact. In a distributed impact, the asperity would break at the point at which the stress exceeds the ultimate tensile strength and not always at the base. The present model assumes a point-impact. This means that the asperity, despite being modelled as a cantilever beam, almost behaves as a point mass system. This simplifies the problem at the expense of accuracy. Using a distributed force of impact would likely result in a lower wear overall as not all the asperities will break at their base. However, the lower wear would be balanced out by the fact that several asperities would be interacting with one another as opposed to a single asperity interacting with another single asperity. Overall, implementing both refinements would lead to an increase in wear.

The effect of wear debris was ignored in the model. This was appropriate regarding the experimental conditions at which the validation was performed. However, it might not be appropriate for wider applications in which wear debris would cause an impact on the wear and the friction noise generated. There are conflicting reports on the effects of wear debris on the friction noise and overall wear rate and this might be difficult to model analytically. Wear debris act as a third body. As they start to accumulate, the abrasive particles on the wear debris might lead to a higher wear rate. However, as more wear debris accumulate, they might instead act as a protective layer, similar to lubrication, thus reducing the wear rate. Another avenue for further work which ties in to the third body concept is to incorporate the effect of lubrication. At present, the model focuses on direct asperity interactions between opposing asperities. Lubrication reduces direct asperity interactions. Instead, asperities interact with the lubricant. In this case, the third body is the lubricant. During the friction

process, the amount of lubrication is reduced and thus, as sliding friction process, direct asperity interactions increase as the lubricant. This would prove complicated to model analytically. Furthermore, examining the interdependencies of the asperities on both surfaces could lead to interesting observations. This is because what happens to one asperity might influence the neighbouring asperities.

Finally, temperature is an important factor in the generation of wear as a higher temperature leads to a higher wear volume. Flash temperatures might also affect the wear rate. Flash temperatures are short-lived, sharp rises in temperature due to the contact between the asperities. In general, there are three temperature factors that can be considered. The temperature of the surroundings, the temperature of the sample and the asperity flash temperature. For all intents and purposes, the temperature of the surroundings can be classified as a constant. The two temperatures of interest are the temperature of the sample. It would be initially equal to the surrounding temperature if no heat is applied. Friction processes could cause a sharp rise in temperature during the sliding process. Further work could include a temperature component that could consider how the flash temperatures will affect the wear rate.

There were also experimental limitations and so further work could go into expanding the scope of the experimental validation. The experimental setup limited the application of temperature, and it also limited the speed and loads that could be applied to the samples. This is because it is difficult to test a wide range of parameters within a lab setting. The speeds and loads were limited due to the safety force sensor on the tribometer. The operation of the tribometer would shut down if the tangential force exceeded a certain value. Furthermore, the temperature was also a limiting factor in a lab setting. Further work could introduce temperatures above 100 °C and loads higher than 20 N.

The analytical model could also be improved by introducing ambient humidity as a variable. Humidity has an impact on the wear rate. This is because, at small scales, water droplets formed by condensation will form cracks on the surfaces. However, at that scale, macroscopic material properties would no longer hold,

and microscopic material properties would have to be used. A further refinement of the model would be to introduce ambient humidity and switch to micro-scale material properties.

9 References

1. *Influence of tribology on global energy consumption, costs and emissions.* **Holmberg, K. and Erdemir, A.** 2017, Friction, Vol. 5, pp. 263-284.

2. *A critical review on different types of wear of materials.* **Devaraju, A.** 11, 2015, International Journal of Mechanical Engineering and Technology, Vol. 6, pp. 77-83.

3. *A Review on Tool Wear Monitoring System.* **Waydande, Prashant, Ambhore, Nitin and Chinchanikar, Satish.** 5A, 2016, Journal of Mechanical Engineering and Automation, Vol. 6.

4. *The relationship between acoustic emissions and wear particles for repeated dry rubbing.* **Hase, Alan, Wada, Masaki and Mishina, Iroshi.** 5-6, 2008, Wear, Vol. 265, pp. 831-839.

5. *Mitigating the Brake Squeal Noise Occurrence of Car Disc Brake through Modification of Caliper-Bracket.* **Chilbule, C., et al.** 2017, SAE Technical Paper 2017-26-0218.

6. *BS-ISO Helical Gear Fatigue Life Estimation and Wear Quantitative Feature Analysis.* **Khan, M. A., Cooper, Dennis and Starr, Andrew.** 4, s.l. : Strain, 2009, Vol. 45. 358-363.

7. *Squeal Noise of Friction Material With Groove-Textured Surface: An experimental and Numerical Analysis.* **Wang, X. C., et al.** 2015, Journal of Tribology.

8. *The Boundary Element Method in Acoustics: A Survey.* **Kirkup, Stephen.** 8, s.l. : Applied Sciences, 2019, Vol. 9.

9. *A cost comparison of boundary element and finite element methods for problems of time-harmonic acoustics.* **Harari, Isaac and Hughes, Thomas J.R.** 1, 1992, Computer Methods in Applied Mechanics and Engineering, Vol. 97, pp. 77-102.

10. **Hadfield, M. and Brebbia, C. A.** *Tribology and Design II.* Southampton : WIT Press, 2012.

11. *Selection and Use of Wear Tests for Metals.* **Bayer, R. G.** 1976, ASTM International.

12. *Embedding Wear Models into Friction Models.* **Blau, Peter J.** 2009, Tribology Letters, pp. 75-79.

13. *Fundamental Aspects of Energy Dissipation in Friction.* **Park, Jeong Young and Salmeron, Miquel.** 1, 2013, Chemical Reviews, Vol. 114, pp. 677-711.

14. *The Significance and Use of the Friction Coefficient.* **Blau, Peter J.** 9, 2001, Tribology International, Vol. 34, pp. 585-591.

15. *Acoustics of friction.* **Akay, Adnan.** 2002, The Journal of the Acoustical Society of America, pp. 1525-1548.

16. *Review and comparison of dry friction force models.* **Pennestri, Ettore, et al.** 2015, Nonlinear Dynamics, pp. 1785-1801.

17. **Gnecco, Enrico and Meyer, Ernst.** *Fundamentals of Friction and Wear on the nano-scale.* s.l. : Springer, 2015.

18. *The Friction and Lubrication of Solids.* **Bowden, F. P. and Tabor, D.** 1951, American Journal of Physics, p. 428.

19. **Bayer, R. G.** *Mechanical wear fundamentals and testing.* New York : Marcel Dekker Inc, 2004.

20. *On the origin of Amonton's friction law.* **Persson, B. N. J., et al.** 2008, Journal of Physics: Condensed Matter.

21. *Contact and Rubbing of Flat Surfaces.* **Archard, J. F.** 1953, Journal of Applied Physics, pp. 981-988.

22. *Contact of nominally flat surfaces.* **Greenwood, J. A. and Williamson, J. B.P.** 1966, Proceedings of the royal society A, pp. 300-319.

23. *Surface Energy and the Contact of Elastic Solids.* **Johnson, K. L., Kendall, K. and Roberts, A. D.** 1971, Proceedings of the Royal Society A: Mathematical, Physical and Engineering Sciences, pp. 301-313.

24. *Effect of contact Deformations on the Adhesion of particles.* **Derjaguin, B., Muller, V. and Toporov, Y.** 1975, Journal of Colloid and Interface Science, pp. 314-326.

25. *An adhesion map for the contact of elastic spheres.* **Johnson, K. L. and Greenwood, J. A.** 1997, Journal of Colloid and Interface science, pp. 326-333.

26. *On the influence of molecular forces on the deformation of an elastic sphere and its sticking to a rigid plane.* **Muller, V., Yushchenko, V. and Derjaguin, B.** 1980, Journal of Colloid and Interface Science, pp. 91-101.

27. *Measurement of Friction Noise Versus Contact Area of Rough Surfaces Weakly Loaded.* **Le Bot, Alain and Chakra, E. Bou.** 2010, Tribology Letters, pp. 273-281.

28. *The effect of nanoparticles on the real area of contact, friction and wear.* **Ghaednia, Hamed and Jackson, Robert L.** 2013, Journal of Tribology.

29. *Estimation of real contact area during sliding friction from interface temperature.* **Chey, Sung Keun, Tian, Pengyi and Tian, Yu.** 2016, AIP Advances.

30. *Relationship between the real contact area and contact force in pre-sliding regime.* **Song, Baojiang and Yan, Shaoze.** 2017, Chinese Physics B.

31. **Rabinowicz, E.** *Friction and wear of materials.* New York : John Wiley, 1965.

32. **Kato, Koji and Adashi, Koshi.** Wear Mechanisms. *Nanomaterials.* s.l. : CRC Press LLC, 2001.

33. *On the debris-level origins of adhesive wear.* **Aghababaei, Ramin, Warner, Derek H. and Molinari, Jean-François.** 2017, Proceedings of the National Academy of Sciences.

34. *Adhesion and friction of polymers.* **Myshkin, Nikolai and Kovalev, Alexander.** 2009, Polymer tribology.

35. *Instability and friction.* **Nguyen, Quoc Son.** 2003, Comptes Rendus Mécanique, pp. 99-112.

36. *The ringing of wine glasses.* **Spurr, R. T.** 1961, Wear, pp. 150-153.

37. *Effect of Geometry on thermoelastic instability in disc brakes and clutches.* **Yi, Yun-Bo, et al.** 1999, Journal of Tribology.

38. *Dissipation of Vibration in Rough Contact.* **Le Bot, A., Bou-Chakra, E. and Michon, G.** 2011, Tribology Letters, pp. 47-53.

39. *Automotive disc brake squeal.* **Kinkaid, N. M., O'Reilly, O. M. and Papadopoulos, P.** 2003, Journal of Sound and Vibration, pp. 105-166.

40. *A cellular Automaton model to describe the three-dimensional friction and wear mechanism of brake systems.* **Müller, M. and Ostermeyer, G. P.** 263, s.l. : Wear, 2007.

41. *On Tangential Friction Induced Vibration in Brake systems.* **Ostermeyer, Georg Peter.** 2010.

42. *A Study on Friction Materials for Brake Squeal Reduction by Nanotechnology.* **Nishiwaki, Masaaki, et al.** s.l. : SAE International, 2008.

43. *Mathematical Structure of Modal Interactions in a Spinning Disk-Stationary Load System.* **Chen, Jen-San and Bogy, D. B.** 1992, Journal of Applied Mechanics , pp. 390-397.

44. *Instabilities Arising From the Frictional Interaction of a Pin-Disk System Resulting in Noise Generation.* **Earles, S.W. E. and Lee, C. K.** 1976, Journal of Engineering for Industry, pp. 81-86.

45. *Disc brake squeal noise generation: predicting its dependency on system parameters including damping.* **Earles, S.W. E. and Chambers, P. W.** 1987, International Journal of Vehicle Design, p. 061217.

46. *Paper VII (i) Brake Noise and Vibration - The State of the Art.* **Crolla, D. A. and Lang, A. M.** 1991, Tribology Series, pp. 165-174.

47. *Analysis of squeal noise and mode coupling instabilities including damping and gyroscopic effects.* **Hervé, B., et al.** 2008, European Journal of Mechanics-A/Solids, pp. 141-160.

48. *Friction-Induced Vibration, Chatter, Squeal, and Chaos---Part I: Mechanics of Contact and Friction.* **Ibrahim, R. A.** 1994, Applied Mechanics Reviews, pp. 209-226.

49. *A Theory of Brake Squeal.* **Spurr, R. T.** 1961, Proceedings of the Institution of Mechanical Engineers: Automobile Division, pp. 33-52.

50. *A Bounded Region of Disc-Brake Vibration Instability.* **Ouyang, H. and Mottershead, J. E.** 2001, Journal of Vibration and Acoustics, pp. 543-545.

51. *Friction-Induced Vibration, Chatter, Squeal, and Chaos—Part II: Dynamics and Modeling.* **Ibrahim, R. A.** 1994, Applied Mechanics Reviews, pp. 227-253.

52. *Chaos in brake squeal noise.* **Oberst, S. and J.C.S, Lai.** 2011, Journal of Sound and Vibration, pp. 955-975.

53. *Friction oscillations with a pin-on-disc tribometer.* **Godfrey, Douglas.** 1995, Tribology International, pp. 119-126.

54. **Tabor, David.** Friction, Lubrication, and Wear. *Mechanical Design Handbook.* s.l. : McGraw-Hill, 2006.

55. *Evaluation of frictional characteristics for a pin-on-disk apparatus with different dynamic parameters.* **Yoon, Eui-Sung, et al.** 1997, Wear, pp. 341-349.

56. *Stick-slip detection through measurement of near field noise.* **Emira, Nadim A., Mohamad, Hamzeh T. and Tahat, Montasser S.** 2011, Journal of Mechanical Engineering Research, pp. 96-102.

57. *Stick-slip vibrations and chaos.* **Popp, K. and Stelter, P.** 1990, Philosophical Transactions: Physical Sciences and Engineering, pp. 89-105.

58. *The effect of frequency of vibration and humidity on the stick–slip amplitude.* **Abdo, Jamil, et al.** 2010, International Journal of Mechanics and Materials in Design, pp. 45-51.

59. *The Effect of Relative Humidity and Roughness on the Friction Coefficient.* **Chowdhury, Mohammad Asaduzzaman and Helali, Maksud.** 2008, The Open Mechanical Engineering Journal, pp. 128-135.

60. *Effect of Groove Surface on Friction Noise and its mechanism.* **Nam, Jae-Hyeon, Do, Hyun-Cheol and Kang, Jae-Young.** 2017, International Journal of Precision Engineering and Manufacturing, pp. 1165-1172.

61. *Influence of geometry imperfections on squeal noise linked to mode lock-in.* **Bonnay, K., et al.** 2015, International Journal of Solids and Structures, pp. 99-108.

62. *Experimental study of the contribution of gear tooth finishing processes to friction noise.* **Jolivet, S., et al.** 2017, Tribology International, pp. 70-77.

63. *A Fundamental Study on Frictional Noise : 1st Report, The generating mechanism of rubbing noise and squeal noise.* **Yokoi, Masayuki and Nakai, Mikio.** 1979, Bulletin of JSME, pp. 1665-1671.

64. *Surface-roughness measurement using dry friction noise.* **Othman, M. O. and Elkholy, A. H.** 1990, Experimental Mechanics, pp. 309-312.

65. *Experimental investigation of frictional noise and surface-roughness characteristics.* **Othman, M. O., Elkholy, A. H. and Seireg, A. A.** 1990, Experimental Mechanics, pp. 328-331.

66. *A Fundamental Study on Frictional Noise : (5th Report, The influence of random surface roughness on frictional noise).* **Yokoi, Masayuki and Nakai, Mikio.** 1982, Bulletin of JSME, pp. 827-833.

67. *The roughness effect on the frequency of frictional sound.* **Stoimenov, Boyko L., et al.** 2007, Tribology International, pp. 659-664.

68. *Numerical simulation of friction noise.* **Abdelounis, H. Ben, et al.** 2011, Wear, pp. 621-624.

69. *Vibrations Induced by Dry Friction.* **Jarvis, R. P. and Mills, B.** 1963, Proceedings of the Institution of Mechanical Engineers, pp. 848-857.

70. *A mechanism of disc brake squeal.* **North, M. R.** 1971. 14th FISITA Meeting.

71. *An augmented lagrangian treatment of contact problems involving friction.* **Simo, J. C. and Laursen, T. A.** 1992, Computers & Structures, pp. 97-116.

72. *An augmented Lagrangian contact formulation for frictional discontinuities with the extended finite element method.* **Hirmand, M., Vahab, M. and Khoei, A. R.** 2015, Finite Elements in Analysis and Design, pp. 28-43.

73. *Algorithmic symmetrization of coulomb frictional problems using augmented lagrangians.* **Laursen, T. A. and Simo, J. C.** 1993, Computer Methods in Applied Mechanics and Engineering, pp. 133-146.

74. *Models and computational methods for dynamic friction phenomena.* **Oden, J. T. and Martins, J. A.C.** 1985, Computer Methods in Applied Mechanics and Engineering, pp. 527-634.

75. *Studies in Lubrication: X. Friction Phenomena and the Stick-Slip Process.* **Morgan, F., Muskat, M. and Reed, D. W.** 1941, Journal of Applied Physics, p. 743.

76. *A new approach to roughness-induced vibrations on a slider.* **Slavic, Janko, Bryant, Michael D. and Boltezar, Miha.** 2007, Journal of Sound and Vibration, pp. 732-750.

77. *Finite element modeling for stick-slip pattern of squeal modes in disc brake.* **Kang, Jaeyoung.** 2014, Journal of Mechanical Science and Technology , pp. 4021-4026.

78. *The Relationship between Frictional Sound and Lumps Build-up at the Contact Interface in Single-pass Dry Sliding between Aluminium Pin and Flat.*

Stoimenov, Boyko L. and Kato, Koji. 2003, Transient Processes in Tribology, pp. 159-164.

79. *Effect of surface roughness on friction-induced noise: Exploring the generation of squeal at sliding friction interface.* **Wang, A. Y., et al.** 2018, Wear, pp. 80-90.

80. *Reducing friction noise of M50 matrix composites by adding Ti3SiC2.* **Chen, Yuan, et al.** 2019, Materials Research Express.

81. *Effect of Surface Roughness on Airframe Noise.* **Liu, Yu, Dowling, Ann P. and Shin, Ho-Chul.** Cambridge : s.n., 2006. The 12th AIAA/CEAS Aeroacoustics Conference.

82. *Friction-Induced Noise and Vibrations: Diagnosis and Prognosis.* **Chen, Gang.** 2013, Advances in Automobile Engineering.

83. *Experimental investigation of friction noise on lubricated contact.* **Nam, Jaehyeon, et al.** 2017, Journal of Mechanical Science and Technology, pp. 5751-5760.

84. *The effect of groove-textured surface on friction and wear and friction-induced vibration and noise.* **Mo, J. L., et al.** 2013, Wear, pp. 671-681.

85. *Friction noise caused by fretting under grease lubrication.* **Jibiki, T., et al.** 2001, The Austrian Tribology Society.

86. *Effect of surface topography on formation of squeal under reciprocating sliding.* **Guangxiong, Chen, et al.** 2002, Wear, pp. 411-423.

87. *1/f Noise in Sliding Friction under Wear Conditions: The Role of Debris.* **Duarte, M., et al.** 2009, Physical Review Letters, p. 045501.

88. *A basic study of friction noise caused by fretting.* **Jibiki, T., et al.** 2001, Wear, pp. 1492-1503.

89. *Adhesive and abrasive wear studies using acoustic emission techniques.* **Boness, R. J. and McBride, S. L.** 1991, Wear, pp. 41-53.

90. *Wear Studies using acoustic emission techniques.* **Boness, R. J., McBride, S. L. and Sobczyk, M.** 1990, Tribology International, pp. 291-295.

91. *Acoustic Emission and Its Relationship with Friction and Wear for Sliding Contact.* **Benabdallah, H. S. and Aguilar, D. A.** 2008, Tribology Transactions, pp. 738-747.

92. *Wear of Metals.* **Barwell, F. T.** 1958, Wear, pp. 317-332.

93. *Wear debris: A review of properties and constitutive models.* **Zmitrowicz, Alfred.** 2005, Journal of theoretical and applied mechanics, pp. 3-35.

94. *Wear modeling and the third body concept.* **Fillot, N., Iordanoff, I. and Berthier, Y.** 2007, Wear, pp. 949-957.

95. *Numerical simulation of sliding wear based on archard model.* **Shen, Xuejin, Cao, Lei and Ruyan, Li.** 2010, 2010 International Conference on Mechanic Automation and Control Engineering, pp. 325-329.

96. *Artificial Neural Network Model for estimation of wear and temperature in pin-disc contact.* **Hassan, Abdul Kareem F. and Mohammed, Sara.** 2016, University Journal of Mechanical Engineering, pp. 39-49.

97. *Wear equation for polymers sliding against metal surfaces.* **Rhee, S. K.** 1970, Wear, pp. 431-445.

98. *The wear of metals under unlubricated conditions.* **Archard, J. F. and Hirst, W.** 1956, Proceedings of the Royal Society A, p. 0144.

99. *The temperature of rubbing surfaces.* **Archard, J. F.** 1959, Wear, pp. 438-455.

100. *Uncertainty analysis on the wear coefficient of Archard model.* **Avila da Silva Jr., Claudio R. and Pintaude, Giuseppe.** 2008, Tribology International, pp. 473-481.

101. *Oxidational wear.* **Quinn, T. F.J.** 1971, Wear, pp. 413-419.

102. *Numerical simulations of mild wear using updated geometry with different step.* **Oqvist, M.** 2001, Wear, pp. 6-11.

103. *Numerical integration schemes and parallel computation for wear prediction using finite element method.* **Mukras, Saad, et al.** 2009, Wear, pp. 822-831.

104. *A surface roughness predictive model in deterministic polishing of ground glass moulds.* **Savio, Gianpaolo, Meneghello, Roberto and Concheri, Gianmaria.** 2009, International Journal of Machine Tools and Manufacture, pp. 1-7.

105. *Friction Models and friction compensation.* **Olsson, H., et al.** 1997, Center for Automation Technologies and Systems.

106. *Friction Modeling in dynamic robot simulation.* **Dupont, Pierre E.** Cincinnati : IEEE, 1990. IEEE International conference on Robotics and Automation. pp. 1370-1376.

107. *Computer Simulation of Stick-Slip Friction in Mechanical Dynamic Systems.* **Karnopp, D.** 1985, Journal of Dynamic Systems, Measurement, and Control, pp. 100-103.

108. *A new model for control of systems with friction.* **Canudas de Wit, C., et al.** 1995, IEEE Transactions on Automatic Control, pp. 419-425.

109. **Dahl, P. R.** *A solid friction model.* s.l. : The Aerospace Corporation, 1968.

110. *Empirical and process-based approaches to climate-induced forest mortality models.* **Adams, Henry D., et al.** 2013, Frontiers in Plant Science, p. 438.

111. *Fundamentals of friction modelling.* **Al-Bender, Farid.** 2010, American Society for Precision Engineering.

112. *The value of a physically based model versus an empirical approach in the prediction of ephemeral gully erosion for loess-derived soils.* **Nachtergaele, Jeroen, et al.** 2001, Geomorphology, pp. 237-252.

113. *Physics-Based friction model with potential application in numerical models for tire-road traction.* **Emami, Anahita, et al.** Tysons : s.n., 2017. Dynamic Systems and Control conference.

114. *A physics-based fretting model with friction and integration to a simple dynamical system.* **Eriten, Melih, Polycarpou, Andreas A. and Bergman, Lawrence A.** Washington DC : s.n., 2011. Proceedings of the ASME 2011 International Design Engineering Technical Conferences & Computers and Information In Engineering Conference.

115. *On the Modeling of Dynamic Friction Phenomena.* **Dankowicz, H.** 1999, Journal of Applied Mathematics and Mechanics.

116. *A Generalised Asperity-Based Friction Model.* **De Moerlooze, Kris, Al-Bender, Farid and Van Brussel, Hendrik.** 2010, Tribology Letters.

117. *The Elastic Contact of Rough Spheres Investigated Using a Deterministic Multi-Asperity Model.* **Yastrebov, Vladislav A.** 1, 2019, Journal of Multiscale Modelling, Vol. 10, p. 1841002.

118. *Modelling acoustic emissions generated by tribological behaviour of mechanical seals for condition monitoring and fault detection.* **Towsyfyan, Hossein, et al.** 2018, Tribology International, Vol. 125, pp. 46-58.

119. *Stick-Slip oscillations: Dynamics of friction and surface roughness.* **Bengisu, M. T and Akay, A.** 1, 1999, The Journal of the Acoustical Society of America, Vol. 105, pp. 194-205.

120. **Blau, Peter J.** Asperities. *Encyclopedia of Tribology.* Boston : Springer, 2013, p. 109.

121. **Volterra, Enrico and Zachmanoglou, E. C.** *Dynamics of Vibrations.* s.l. : Charles E. Merrill, 1965.

122. **Gere, James M. and Goodno, Barry J.** *Mechanics of Materials.* Boston : Cengage Learning, 2012.

123. *Noise Radiated by Baffled Plates.* **Norton, M. P. and Pan, J.** 2001, Encyclopedia of Vibration, pp. 887-898.

124. **Gohar, Ramsey and Rahnejat, Homer.** *Fundamentals of Tribology (2nd Edition).* London : Imperial College Press, 2012.

125. *Normal and Angular Motions at Rough Planar Contacts During Sliding With Friction.* **Hess, D. P. and Soom, A.** 1992, Journal of Tribology, pp. 567-578.

126. *Developments in the theory of surface roughness.* **Greenwood, J. A. and Williamson, J. B. P.** London : Mechanical Engineering Publications, 1977.

127. **Greenwood, J. A.** *Contact of rough surfaces.* s.l. : Kluwer Academic Publishers, 1992.

128. *Surface Roughness and Contact: An Apology.* **Greenwood, J. A. and Wu, J. J.** 2001, Meccanica, pp. 617-630.

129. *Analytical Approximations in Modelling Contacting Rough Surfaces.* **Polycarpou, Andreas A. and Etsion, Izhak.** 1999, Journal of Tribology, Vol. 121, pp. 234-239.

130. *Quantitative Roughness Characterization of Geological Surfaces and Implications for Radar Signature Analysis.* **Dierking, Wolfgang.** 5, 1999, IEEE Transactions on Geoscience and Remote Sensing, Vol. 37, pp. 2397-2412.

131. *Study on microstructure and abrasive wear behaviour of sintered Al matrix composites.* **Mazahery, Ali and Shabani, Mohsen Ostad.** 5, 2012, Ceramics International, Vol. 38, pp. 4263-4269.

132. *Experimental Study on Friction Noise of Dry Rough Surfaces.* **Abdelounis, H. Ben, et al.** Miami : s.n., 2008. STLE/ASME 2008 International Joint Tribology Conference.

133. *Experimental assessment of multiple contact wear using airborne noise under dry and lubricated conditions.* **Khan, M., et al.** 12, 2017, Proceedings of the Institution of Mechanical Engineers,Part J: Journal of Engineering Tribology, Vol. 231, pp. 1503-1516.

APPENDICES

Appendix A :MATLAB code

```
prompt = 'Diameter of the disc';
D = input(prompt)
prompt = 'UTS';
UTS = input(prompt)
prompt = 'yield';
yield = input(prompt)
prompt = 'diameter of the asperity';
d = input(prompt)
Totalsliding = pi*D;
temperature = 0;
Aswidthtemp = exprnd(0.04e-03, 1000000, 1);
tempArray = zeros(1000000,1);
increment = 1;
totalSoundPressure = 0;
while (sum(tempArray) <= Totalsliding)
    tempArray(increment) = Aswidthtemp(increment);
    increment = increment + 1;
end
firstZero = find(tempArray == 0, 1, 'first');
tempArray(firstZero:end)=[];
N = length(tempArray);
N2 = int32(N);
tempArray2 = cumsum(tempArray);
prompt = 'Ra';
mu = input(prompt)
R = exprnd(1.6900e-06, N2, 1);
qtotalswep = 0;
R = transpose(R);
R1 = R;
R1 = transpose(R1);
CrossA = (pi*(d/2)^2)/2;
prompt = 'density';
density = input(prompt)
prompt = 'speed';
RPM = input(prompt)
v = (D/2) * ((2*pi)/60)*RPM;
O = 1/(RPM/60);
t = (O) / N;
S = (pi*((d/2)^4)/8)/((4*(d/2))/(3*pi));
prompt = 'Young modulus';
Young = input(prompt)
I = (pi / 4)* ((d/2) ^4);
Omega = RPM / 60;
pinlength = 0.05;
thermalconductivity = 25;
prompt = 'initial load';
W = input(prompt)
G = mu;
A = ((3*Young*I)/(UTS*S))^0.5;
B = (2*Young*I)/ (UTS*S*A);
J = A+B;
BM = 1.38064852e23;
prompt = 'temp';
temp = input(prompt)
```

```
prompt = 'pressure';
Pressure = input(prompt)
pmet = 0;
pmet2 = 0;
q = 0;
qtotal = 0;
qtotalend = 0;
dynamicfric = 0;
thermdiffu = 9.7*10^-5;
Peclet = (v*(pi*(D^2)^2))/(2*thermdiffu);
weartemp=[];
kfact=1;
Wear = 0;
x = 1.e-03;
Accel = 9.8;
TotalDist = 0;
initvel(1) = 0;
Beta = 0.5;
soundvel = 343;
airdens = 1.225;
prompt = 'radeff';
radeff = input(prompt)
PR = 10e-12;
Q = 1;
P = zeros(1,1000000);
refPressure = 20e-06;
prompt = 'hardness';
hardness = input(prompt)
TBC = zeros(1,40000);
initvel = zeros(1,40000);
DistPinTravel = zeros(1,40000);
Vasp = zeros(1,40000);
MassAsp = zeros(1,40000);
CritDamping = zeros(1,40000);
DampingCoefficient = zeros(1,40000);
DampingRatio = zeros(1,40000);
F = zeros(1,40000);
M = zeros(1,40000);
Stress = zeros(1,40000);
TimeTot  =zeros(1,2999);
WearTot  =zeros(1,2999);
SoundTot = zeros(1,2999);
weartemp = zeros(1,40000);
Wearinst  =zeros(1,40000);
E = zeros(1,40000);
A1 = zeros(1,40000);
A2 = zeros(1,40000);
A3 =zeros(1,40000);
displacement = zeros(1,40000);
Ddisplacement = zeros(1,40000);
Fequiv = zeros(1,40000);
q = zeros(1,40000);
VibrVel = zeros(1,40000);
Lw = zeros(1,40000);
Lp1 = zeros(1,40000);
soundpressure =zeros(1,40000);

for i = 1:N2
    TBC(i) = tempArray(i)/v;
```

```
    initvel(i+1) = initvel(i) + 9.8*(TBC(i));
end
for i = 1:N2
    DistPinTravel(i) = (initvel(i)* TBC(i))+ 0.5*9.8*((TBC(i))^2);
end
for k = 1:length(R)
    Vasp(k) = CrossA * R(k);
    MassAsp(k) = Vasp(k)* density;
    CritDamping(k) = MassAsp(k)*2*Omega;
    DampingCoefficient(k) = 4*(0.04e-
03)*R(k)*sqrt(((2*MassAsp(k))/(pi*BM*temp))*Pressure);
    DampingRatio(k) = DampingCoefficient(k) / CritDamping(k);
    if k ~= length(R)
        if R(k) - R(k+1) < DistPinTravel(k)
            F(k) = (MassAsp(k)*v)/t;
            M(k) = F(k)*(R(k)-(DistPinTravel(k)));
            Stress(k)=M(k)/S;
            initvel(k) = 0;
            DistPinTravel(k) = (initvel(k)* TBC(k))+
0.5*9.8*((TBC(k))^2);
        end
    end
end
nrows = 1;
ncols = N2-1;
Test = ones(nrows, ncols);
mope = 1;

for b = 2*O:O:600
    TimeTot(mope) = b;
    WearTot(mope) = Wear;
    SoundTot(mope) = totalSoundPressure;
    mope = mope+1;
for c = 1:ncols-1
    if Stress(c) > yield && Stress(c) < UTS
        Test(c) = 3;
    elseif Stress(c) >= UTS
        Test(c) = 4;
    else
        Test(c) = 2;
    end
end

for L = 1:1:N2-1
    if Test(L) == 4
        Wear = (pmet);
        pmet = R(L) + pmet;
        weartemp(L) = R(L);
        R(L) = ((G*J*sqrt((((J^2)/4)*(b^2))-
(J*b*((R(L)+x)^0.5))+(R(L)+x))-initvel(L))/(J*((R(L)+x)^0.5))-
initvel(L))*exp(log10(G*exp((-G*(x+(((J^2)/4)*(b^2))-
(J*b*((R(L)+x)^0.5))+R(L)+x)))));
        E(c) = Hardness*pi*((d/2)^3)*Beta;
        P(c) = CrossA*soundvel*E(c);
    end
end
weartemp=[];
kfact = kfact+1;
```

```
for c = 1:1:N2-1
    if Test(c) == 2
        c = double(c);
        lambda = (((density * CrossA)/(Young * I))* (Omega^2))^0.25;
        A1(c) = (-
F(c)*W*R(c))/(Young*I*density*CrossA*(lambda^4)*(lambda*R(c))*exp(lamb
da*R(c))+exp(2*lambda*R(c))-1);
        A2(c) = 3*sin(lambda*R(c))*(exp(2*lambda*R(c))+1)-
2*((lambda*R(c))^3)*exp(lambda*R(c))-cos(lambda*R(c))*(3-
((lambda*R(c))^3)*(exp(2*lambda*R(c))+1)-3*exp(2*lambda*R(c)));
        A3(c) = A1(c)*A2(c);
        displacement(c) = A3(c)*cos(Omega*O);
        Ddisplacement(c) = displacement(c)*exp(-
1*DampingRatio(c)*O)*cos(Omega*O);
        if R(c) - R(c+1) < DistPinTravel(c)
            if c == length(R)
                break;
            end
        Fequiv(c) = (6*Ddisplacement(c)*Young*I)/(((R(c)-
DistPinTravel(c))^2)*(3*R(c)-DistPinTravel(c)));
        F(c) = (MassAsp(c)*v)/t;
        q(c) = 0.57*F(c)*v;
        F(c) = F(c)+Fequiv(c);
        if R(c) < R(c+1)
            M(c) = F(c)*(R(c+1)-R(c));
        else
            M(c) = F(c)*(R(c)-(DistPinTravel(c)));
        end
        Stress(c)=M(c)/S;
        initvel(c) = 0;
        DistPinTravel(c) = (initvel(c)* TBC(c))+ 0.5*9.8*((TBC(c))^2);
        VibrVel(c) = -DampingRatio(c)*Omega*O*displacement(c)*exp(-
DampingRatio(c)*Omega*O)*cos(Omega*O)-displacement(c)*exp(-
DampingRatio(c)*Omega*O)*sin(Omega*O);
        P(c) = airdens*soundvel*CrossA*radeff*(VibrVel(c)^2);
        end
        elseif Test(c) == 3
        Stress(c) = Stress(c) *2;
    end
    if P(c) ~= 0
        Lw(c) = 10*log10((P(c))/PR);
        Lp1(c) = Lw(c)+10*log10(Q/(4*pi*((d/2)^2)));
        soundpressure(c) = refPressure*10^((1/20)*Lp1(c));
    end
end
for i= 1:length(soundpressure)
    totalSoundPressure = totalSoundPressure + soundpressure(i);
end
end
TimeTot = transpose(TimeTot);
WearTot = transpose(WearTot);
SoundTot=transpose(SoundTot)
```